International Journal of Antennas and Propagation

MIMO Antenna Design and Channel Modeling 2014

Guest Editors: Wenhua Chen, Manos M. Tentzeris, Neil Trappe, Yuan Yao, Yan Zhang, and Xinyi Tang

MIMO Antenna Design and Channel Modeling 2014

International Journal of Antennas and Propagation

MIMO Antenna Design and Channel Modeling 2014

Guest Editors: Wenhua Chen, Manos M. Tentzeris, Neil Trappe, Yuan Yao, Yan Zhang, and Xinyi Tang

Editorial Board

Contents

Hindawi Publishing Corporation
International Journal of Antennas and Propagation
Volume 2015, Article ID 675650, 1 page
http://dx.doi.org/10.1155/2015/675650

Editorial

MIMO Antenna Design and Channel Modeling 2014

Wenhua Chen,[1] Manos M. Tentzeris,[2] Neil Trappe,[3] Yuan Yao,[4] Yan Zhang,[5] and Xinyi Tang[6]

[1] *Department of Electronic Engineering, Tsinghua University, Beijing 100084, China*
[2] *School of Electrical and Computer Engineering, Georgia Institute of Technology, Atlanta, GA 30332-0250, USA*
[3] *Experimental Physics Department, National University of Ireland Maynooth, Location Science Building, Room 2.13, Ireland*
[4] *School of Electronic Engineering, Beijing University of Posts and Telecommunications, Beijing 100876, China*
[5] *Beijing Institute of Technology, Beijing 100081, China*
[6] *Institute for Infocomm Research, 1 Fusionopolis Way, Singapore 138632*

Correspondence should be addressed to Wenhua Chen; chenwh@tsinghua.edu.cn

Received 18 May 2015; Accepted 18 May 2015

Every ten years or so, something big happens in mobile. Now, 5G is emerging ahead of the turn of a new decade and the next big change to hit mobile. Massive MIMO is believed to be a disruptive technology for the upcoming 5G standard, which makes a clean break with current practice through the use of a very large number of service antennas that are operated fully coherently and adaptively. Extra antennas help by focusing the transmission and reception of signal energy into ever-smaller regions of space. This brings huge improvements in throughput and energy efficiency, particularly when combined with simultaneous scheduling of a large number of user terminals.

In this special issue, we have received 18 paper submissions, the accepted papers include wideband MIMO antenna design, power allocation optimization, mutual Coupling suppression.

We sincerely hope that this special issue can further help the readers to understand MIMO design and MIMO channel modeling and explore the future 5G MIMO in the subsequent development and standardization of the system.

Wenhua Chen
Manos M. Tentzeris
Neil Trappe
Yuan Yao
Yan Zhang
Xinyi Tang

Hindawi Publishing Corporation
International Journal of Antennas and Propagation
Volume 2015, Article ID 801638, 9 pages
http://dx.doi.org/10.1155/2015/801638

Research Article

A Novel Miniaturized Dual Slant-Polarized UWB Antenna Array with Excellent Pattern Symmetry Property for MIMO Applications

Zhi Zeng,[1] Jianjun Huang,[2] Zhaohui Song,[3] and Qinyu Zhang[1]

[1] *Shenzhen Graduate School, Harbin Institute of Technology, Shenzhen 518055, China*
[2] *MOBI Antenna Technologies (Shenzhen) Co., Ltd., Shenzhen 518057, China*
[3] *Harbin Institute of Technology, Harbin 150001, China*

Correspondence should be addressed to Qinyu Zhang; zqy@hit.edu.cn

Received 30 June 2014; Accepted 4 September 2014

Academic Editor: Wenhua Chen

A novel miniaturized 1 × 10 uniform linear dual slant-polarized UWB antenna array for MIMO base station is presented. The antenna array operates in the frequency band from 1710 to 2690 MHz with a 17.3–18.7 dBi gain in a size of 105 × 1100 × 37 mm. The array element is composed of two single-polarized dipoles evolved from bow-tie antenna with slots on them, which miniaturize the size of the antenna. The 10 array elements are fed through an air dielectric strip-line power splitter. Two parameters, the beam tracking and the beam squint, are presented to quantitatively describe the pattern symmetry property of the antenna. The simulated and measured radiation performances are studied and compared. The results show that the pattern symmetry property of the single antenna element has been improved about 24% compared with the former study, and the antenna array also provides excellent pattern symmetry property.

1. Introduction

Multiple-input multiple-output (MIMO) is the use of multiple antennas at both the transmitter and the receiver to improve communication performance [1]. MIMO has attracted attention in wireless communications, because it offers significant increases in data throughput and link range without additional bandwidth or increased transmit power [2]. It achieves this goal by spreading the same total transmit power over the antennas to achieve an array gain that improves the spectral efficiency and/or to achieve a diversity gain that improves the link reliability (reduced fading) [3]. Because of these advantages, MIMO is an important part of modern wireless communication standards such as IEEE 802.11n (WI-Fi), 4G, 3GPP Long Term Evolution (LTE), WiMAX, and HSPA+ [4]. While coding and signal processing are key elements to successful implementation of a MIMO system, the propagation channel and the antenna design represent major parameters that ultimately impact the system performance. As a result, considerable research has been devoted recently to these two areas. For example, assessing the potential of MIMO systems requires a new level of understanding concerning multipath channel characteristics. Furthermore, while we have extensive information concerning the behavior of an antenna in multipath channels [5], recent activity surrounding MIMO communications has exposed new issues related to the impact of antenna properties and the array configuration on the system performance. In [6], a simulation study of the channel capacity of a MIMO antenna system exploiting multiple polarizations was carried out, while in [7] Perez and Ibanez analyzed the capacity of MIMO systems based on dual-polarized antenna array.

In modern mobile telecommunications industry, dual slant-polarized (+45°/−45°) base station antennas are widely used for their good anti-multi-path property. Usually, in a 2G network, a dual slant-polarized base station antenna works in 1T2R mode (1 of the 2 channels for transmitting, both 2 channels for receiving). In 3G or LTE network, both 2 channels of the dual slant-polarized base station antenna might be used to transmit and receive the signal. In this case, highly symmetric

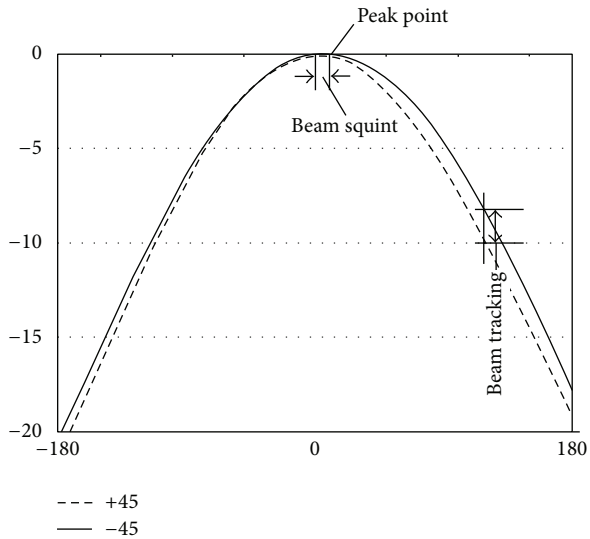

Figure 1: Antenna beam tracking and antenna beam squint.

radiation patterns are required to the dual slant-polarized base station antenna. However, only a few studies about the radiation pattern symmetry of the antenna were carried out in the past. In [8], Chair et al. studied 4 different types of dual-polarized dielectric resonator antennas and analyzed their radiation pattern symmetry qualitatively. In [9], Gao et al. presented a CPW-fed dual-polarized dielectric resonator antenna with "almost symmetrical" radiation patterns. In [10], Mak and Rowell presented a dual-polarized patch antenna with symmetrical patterns for base station in 1710–2690 MHz, but they did not analyze the pattern symmetry quantitatively either. In [11] Kim et al. proposed a modified dual-polarization horn antenna to improve radiation pattern symmetry and presented a method to evaluate the radiation pattern symmetry. They quantitatively analyzed the radiation pattern symmetry by comparing the normalized radiation pattern level of the E/H-plane at some specified angles including the −10 dB beam width point. The smaller the differences, the better the radiation pattern symmetry. Both the simulated and measured results have shown that the radiation pattern level differences increase as the angle increases within the −10 dB beam width range, so the difference at −10 dB beam width point can be considered as a characteristic to describe the radiation pattern symmetry. In this paper, it is called *the beam tracking*, which is defined as the maximum level difference between the two orthogonal polarizations normalized radiation patterns at the 10 dB beam width point, as shown in Figure 1. The beam tracking can be expressed as

$$\text{Beam tracking} = \max\left(\left|L_{-L} - L_{+L}\right|, \left|L_{-R} - L_{+R}\right|\right), \quad (1)$$

where L_{-L} is the level of −45° polarization at the 10 dB point on the left, L_{+L} is the level of +45° polarization at the 10 dB point on the left, L_{-R} is the level of −45° polarization at the 10 dB point on the right, and L_{+R} is the level of +45° polarization at the 10 dB point on the right. The smaller the beam tracking is, the better the symmetry of the radiation pattern is. Ideally, the value of beam tracking is expected to be 0, which means that the two patterns coincide completely at the 10 dB point. In [11], the authors supposed that the boresight was the axis of symmetry of the antenna. However, for most antennas, the boresight is not the symmetry axis of the antenna, because the beam is always tilted to one side, more or less. In this case only the amplitude is not enough to describe the radiation pattern symmetry, but also the angular dimension, *the beam squint*. The beam squint is defined as the ratio of the boresight angle to the 10 dB beam width;

$$\text{Beam squint} = \frac{\text{boresight angle}}{10\,\text{dB beam width}}. \quad (2)$$

Ideally, the value of beam squint is expected to be 0, which means that the boresight is just the symmetry axis of the antenna. The beam tracking and the beam squint describe the symmetric property of the dual-polarized antenna in the amplitude domain and the angular domain, respectively.

In this paper, a novel compact 1 × 10 dual slant-polarized antenna array with excellent pattern symmetry property is presented. The proposed antenna array operates in the frequency band from 1710 to 2690 MHz, with a size of 105 × 1300 × 37 mm. The fractional bandwidth of the antenna array is 44.5%, which could be classified as ultra wideband (UWB) antenna according to the definition of UWB antenna by the Federal Communications Commission (FCC) and the International Telecommunication Union Radio (ITU-R) [12]. The simulations of the proposed antenna are performed using the commercial electromagnetic simulation software HFSS. In the whole range of 10 dB beam width, the worst beam tracking of the array element is 0.40 dB, which has been improved about 24% compared with the result as 0.5398 dB in [11]. And the beam squint values are better than 1%. The antenna array also provides excellent pattern symmetry property. A prototype of the proposed antenna array was fabricated and measured in an anechoic chamber. The experimental measurements concerning the antenna parameters are found to be in good agreement with the numerical results.

2. Antenna Array Structure and Design

2.1. Antenna Array Element. The pattern symmetry property of the antenna array is mainly decided by the properties of the array element, so the design of the array element is quite important. The geometry of the proposed antenna array element is shown in Figure 2. The dual slant-polarized array element is composed of 2 evolved bow-tie antennas on a 105 mm wide reflector, and the total height is 37 mm. The evolutionary process from bow-tie antenna to the proposed array element is shown in Figure 3. The bow-tie antenna is a kind of antenna with two flaring, triangular shaped arms, which is a typical wide band antenna [13]. By adding slot on the arms, the equivalent electrical length of the arms is increased, so as to miniaturize the dimensions of the antenna. The array element has a strictly symmetrical structure, which is expected to obtain good radiation symmetry property. The feeding structure of the array element is shown in Figure 4.

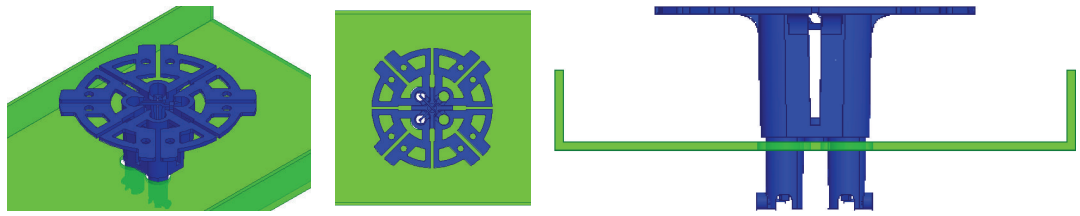

(a) (b) (c)

Figure 2: The geometry of the array element: (a) 3D view, (b) top view, (c) and side view.

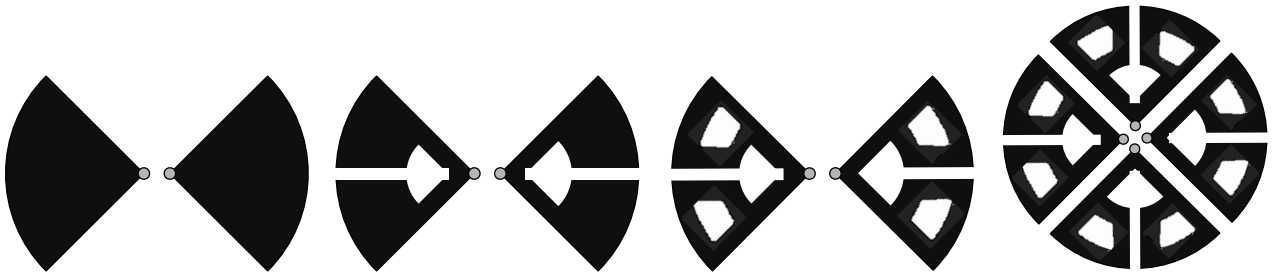

(a) (b) (c) (d)

Figure 3: The evolution from bow-tie antenna to the proposed array element: (a) bow-tie antenna, (b) bow-tie antenna with slots, (c) bow-tie antenna with slots and holes, and (d) the proposed array element.

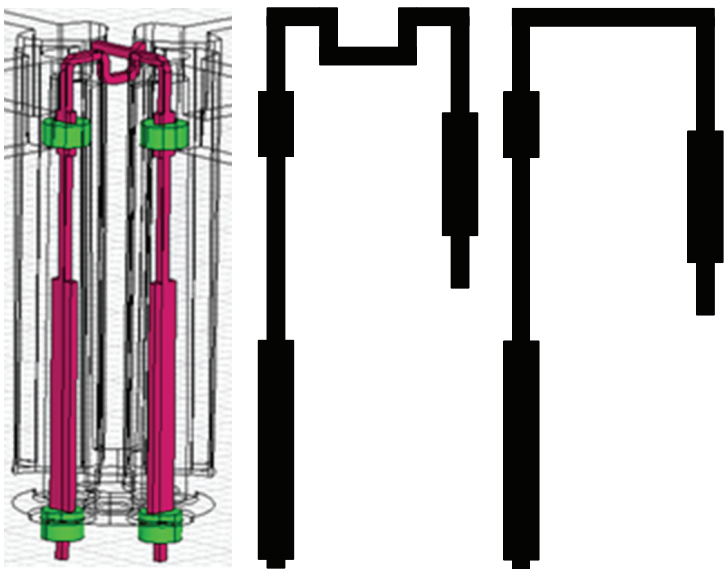

(a) (b) (c)

Figure 4: The feeding structure of the dipole: (a) 3D view, (b) the feeding structure for −45°, and (c) the feeding structure for +45°.

By adjusting the shape and the dimensions of the inner conductor, the antenna can be matched to 50 Ω transmission lines in a bandwidth of 1710 MHz–2690 MHz. Besides that, there are some holes in the arms and some raised blocks at the edge of the arms, which are brought in to tune the return loss over the whole frequency band.

2.2. Antenna Array. Based on the array element above, a uniform linear antenna array is designed. The proposed antenna array is composed of 10 elements, and the spacing between the elements was set to 110 mm based on the frequency characteristic. The structure of the antenna array is shown in Figure 5. The antenna array is fed by two 1 to 10 air dielectric strip-line power splitters, which are connected with the 10 elements through several coaxial cables as shown in Figure 6. The air dielectric strip-line has quite low transmission loss, which contributes to the gain of the antenna. The amplitude of each dipole could be conveniently adjusted by adjusting

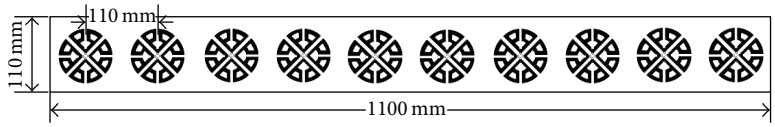

Figure 5: The structure of the antenna array.

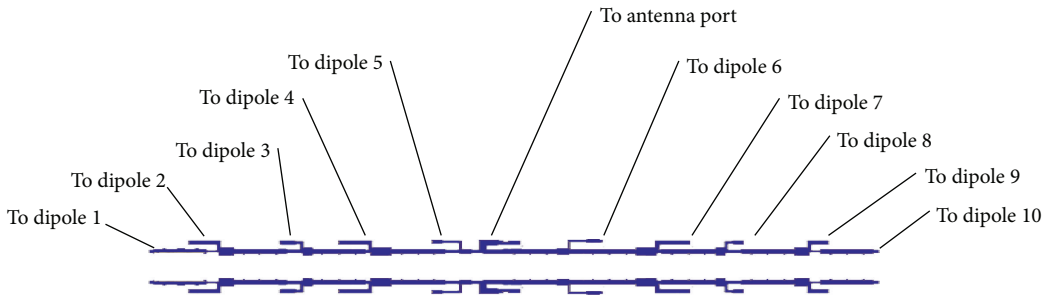

Figure 6: The feeding structure of the antenna array.

Table 1: The simulated beam tracking computed in H-plane and E-plane.

Freq. (MHz)	H-plane		E-plane	
	Element beam tracking (dB)	Array beam tracking (dB)	Element beam tracking (dB)	Array beam tracking (dB)
1710	0.04	0.05	0.05	0.06
2200	0.06	0.06	0.07	0.07
2690	0.08	0.09	0.09	0.10

the impedance of the corresponding matching section, and the phase of each dipole could be adjusted by adjusting the corresponding cable length. The dimensions of the antenna array are 105 × 1100 × 37 mm.

3. Antenna Array Simulation and Measurement

A commercial electromagnetic simulation software HFSS is used to analyze the performance of the proposed antenna element and the antenna array. The weight of the amplitude and the phase of each element were optimized to achieve a low upper side lobe level, which is quite critical for a wireless telecommunication system base station. The antenna array has around 65 degrees beam-width in H-plane, which is quite suitable for base station of mobile communication. The beam tracking and the beam squint of the array element and the antenna array are calculated in E-plane and H-plane. The simulated results of the beam tracking are shown in Table 1. The simulated beam squint results of the array element and the antenna array are shown in Tables 2 and 3, respectively. The simulated results show that both the proposed antenna element and the antenna array have quite good pattern symmetry property.

Table 2: The simulated beam squint of the array element.

Freq. (MHz)	H-plane		E-plane	
	−45°	+45°	−45°	+45°
1710	0.35%	0.30%	0.38%	0.34%
2200	0.48%	0.53%	0.49%	0.57%
2690	0.53%	0.58%	0.60%	0.58%

Table 3: The simulated beam squint of the antenna array.

Freq. (MHz)	H-plane		E-plane	
	−45°	+45°	−45°	+45°
1710	0.35%	0.32%	0.39%	0.34%
2200	0.50%	0.55%	0.49%	0.58%
2690	0.56%	0.59%	0.61%	0.60%

A prototype of the proposed antenna array was fabricated for measurement. The array elements were made of aluminum for its good processing property and coated with Tin to prevent the surface oxidation. The picture of the proposed antenna array prototype is shown in Figure 7, while the numerical and measurement results concerning the frequency behavior of the S parameters of the antenna are reported in Figure 8.

The measurement of radiation patterns was carried out in an enclosed anechoic chamber. The simulated and the measured radiation patterns in H-plane and E-plane are shown in Figures 9 and 10, respectively.

The simulated and the measured gain curves of the proposed antenna array are shown in Figure 11. However, the measured gain data of the antenna is approximately 0.1 dB below the predicted values in the operation frequency band. The reason for this behavior is probably coupling within the cable loss and/or the nonideal power distribution of the power dividers.

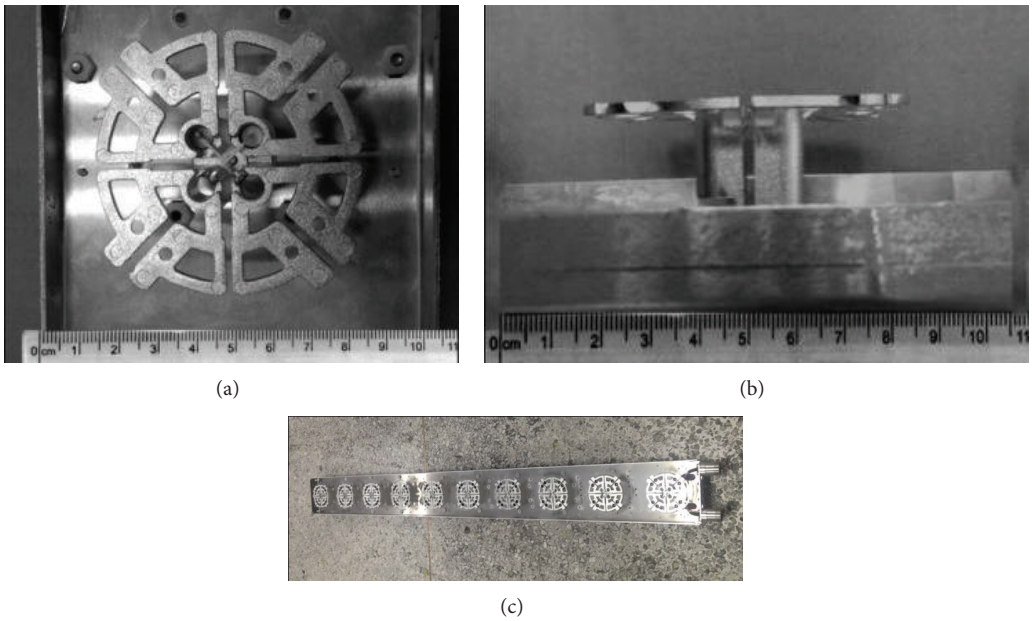

Figure 7: The photo of the proposed antenna array: (a) top view of the array element, (b) side view of the array element, and (c) the proposed antenna array.

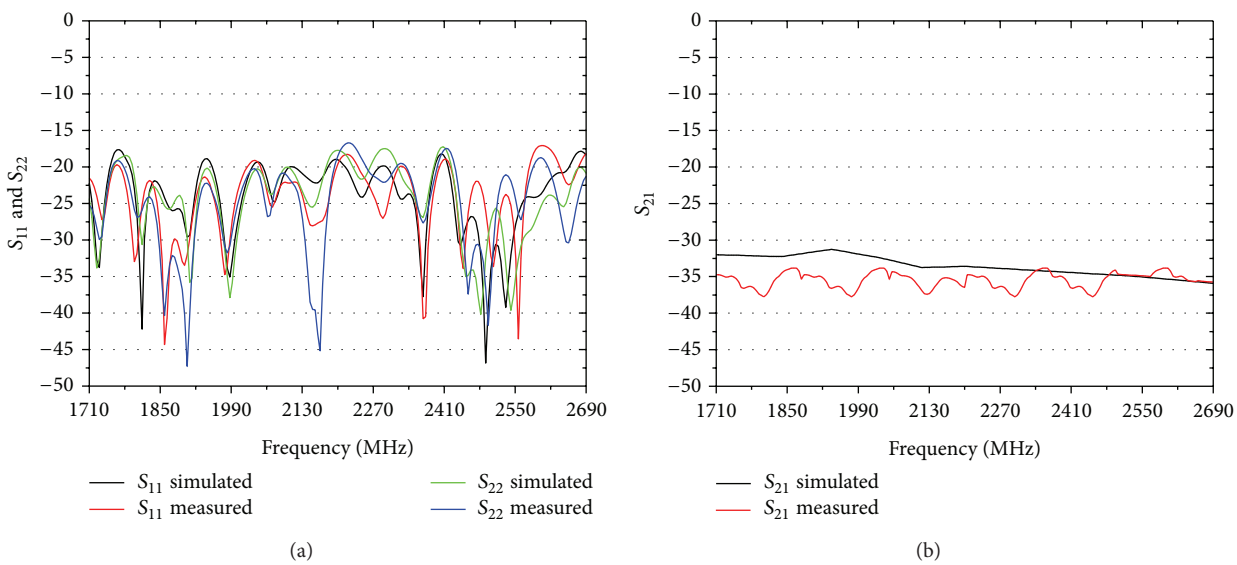

Figure 8: The simulated and measured S parameters of the proposed antenna array: (a) $|S_{11}|$ and $|S_{22}|$ and (b) $|S_{21}|$.

The beam tracking and the beam squint of the array element and antenna array are measured in E-plane and H-plane; the measured results of the beam tracking are shown in Table 4. The measured beam squint results of the array element and the antenna array are shown in Tables 5 and 6, respectively. The measured array element beam tracking results are better than 0.40 dB, which is about 24% better than the results as 0.5398 dB in [11]. And the measured antenna array beam tracking results are better than 0.41 dB. Besides that, all the measured results of the beam squint are better than 1%. The measured data agree very well with the numerical results and show attractive pattern symmetry characteristics for a MIMO base station.

4. Conclusion

In this paper, a novel compact 1 × 10 dual slant-polarized antenna array with excellent pattern symmetry property has been proposed. The antenna array is composed of 10 dual slant-polarized antenna array elements, which evolved from the bow-tie antennas. The antenna array operates in the frequency band 1710–2690 MHz, with a size

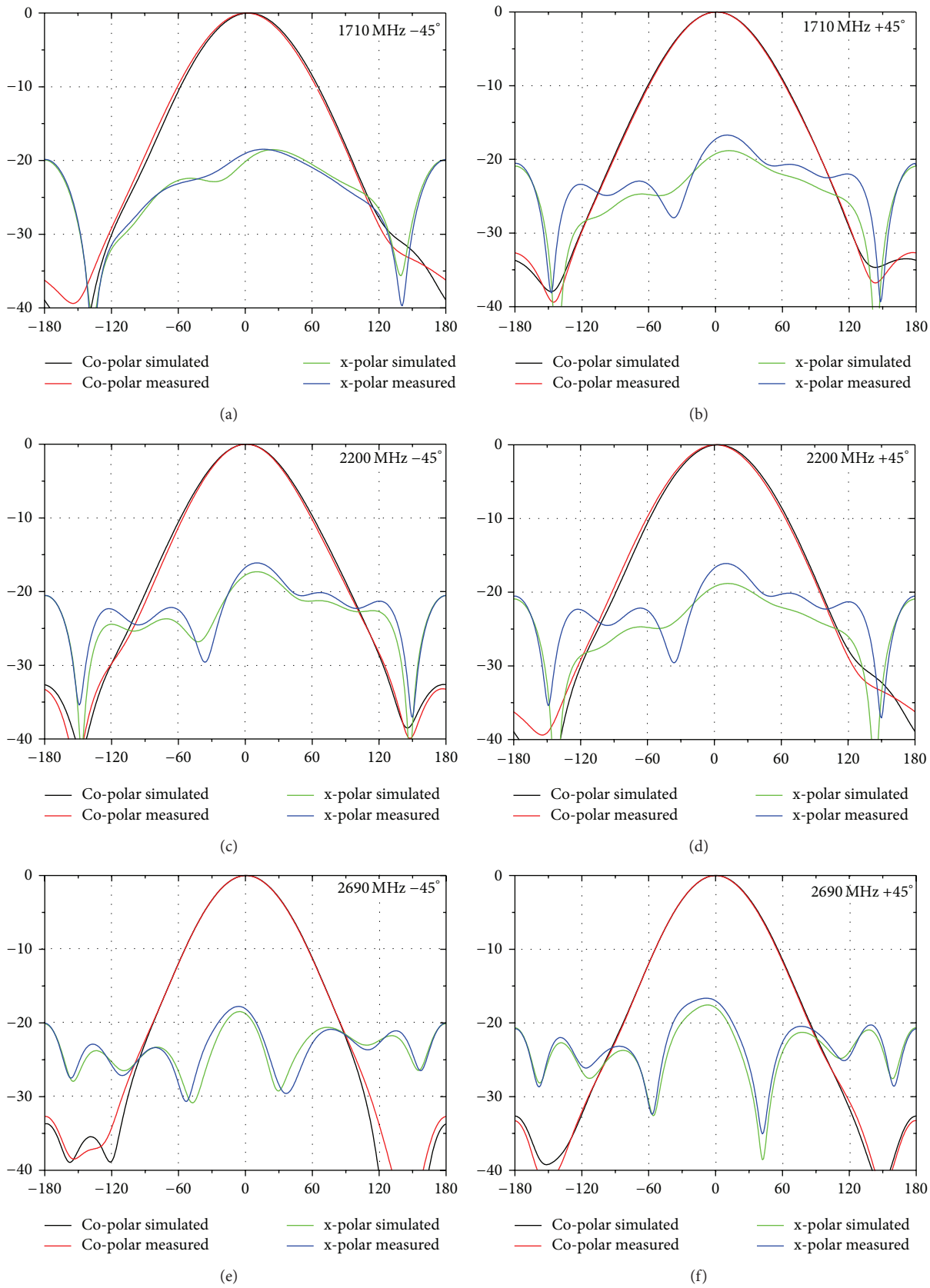

Figure 9: The simulated and measured radiation patterns in H-plane: (a) 1710 MHz −45°, (b) 1710 MHz +45°, (c) 2200 MHz −45°, (d) 22000 MHz +45°, (e) 2690 MHz −45°, and (f) 2690 MHz +45°.

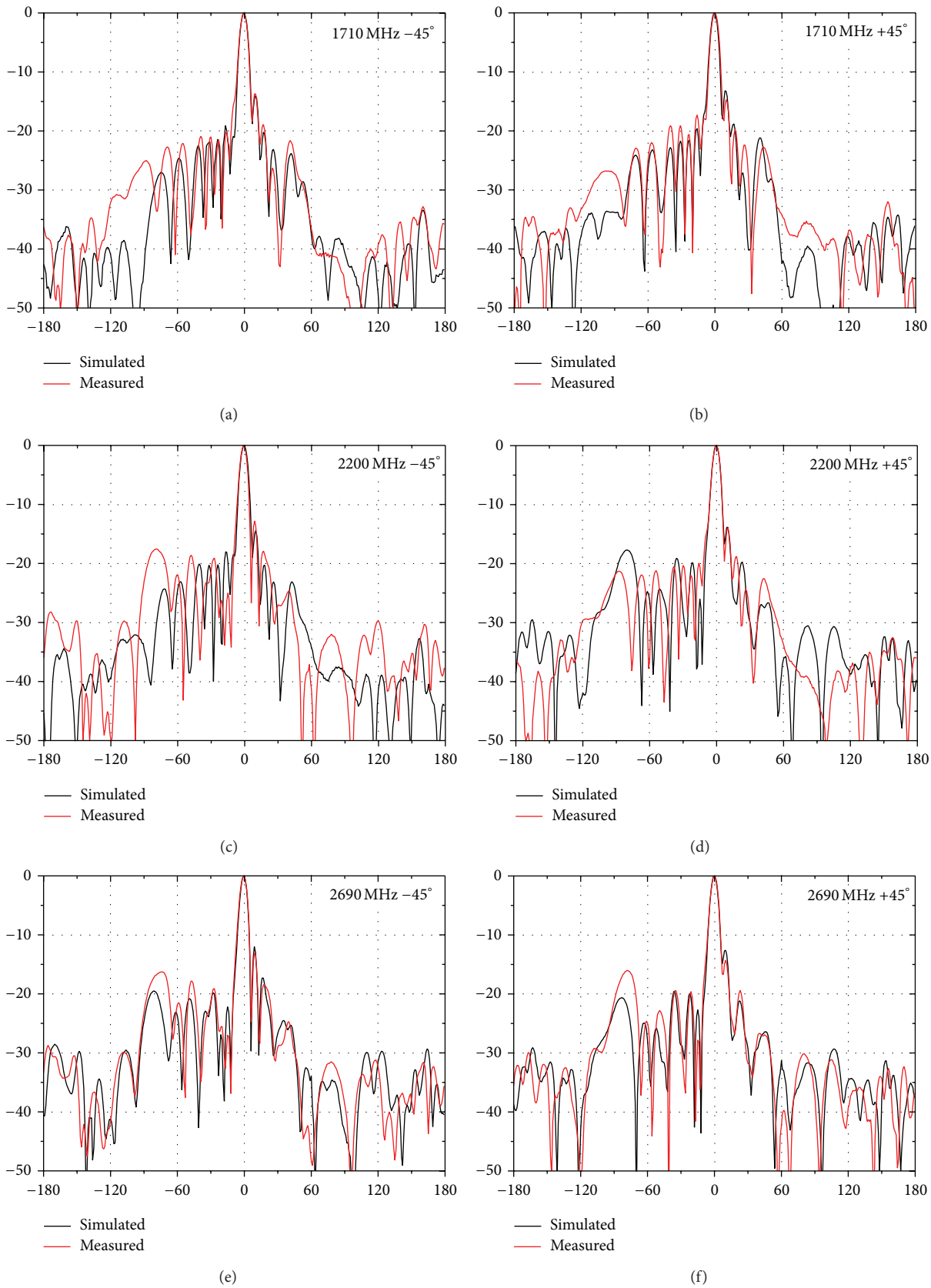

Figure 10: The simulated and measured radiation patterns in E-plane: (a) 1710 MHz −45°, (b) 1710 MHz +45°, (c) 2200 MHz −45°, (d) 22000 MHz +45°, (e) 2690 MHz −45°, and (f) 2690 MHz +45°.

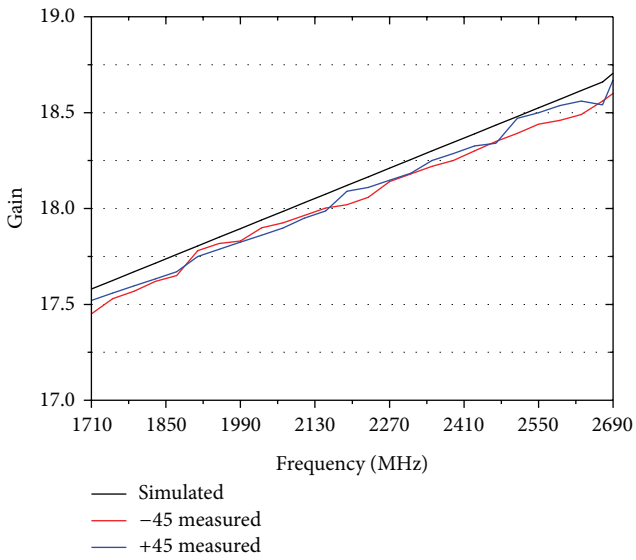

Figure 11: The gain of the proposed antenna array.

Table 4: The measured beam tracking computed in H-plane and E-plane.

Freq. (MHz)	H-plane		E-plane	
	Element beam tracking (dB)	Array beam tracking (dB)	Element beam tracking (dB)	Array beam tracking (dB)
1710	0.26	0.26	0.27	0.28
2200	0.36	0.36	0.37	0.37
2690	0.40	0.41	0.40	0.40

Table 5: The measured beam squint of the array element.

Freq. (MHz)	H-plane		E-plane	
	−45°	+45°	−45°	+45°
1710	0.80%	0.74%	0.58%	0.55%
2200	0.65%	0.63%	0.70%	0.67%
2690	0.52%	0.47%	0.56%	0.53%

Table 6: The measured beam squint of the antenna array.

Freq. (MHz)	H-plane		E-plane	
	−45°	+45°	−45°	+45°
1710	0.82%	0.75%	0.69%	0.54%
2200	0.71%	0.69%	0.72%	0.73%
2690	0.66%	0.51%	0.60%	0.61%

of 105 ∗ 1300 ∗ 37 mm only. Two parameters, the beam tracking and the beam squint, that quantitatively describe the pattern symmetry, were presented. The results show that the pattern symmetry property of the single antenna element has been improved about 24% compared with the former study, and the antenna array also provides excellent pattern symmetry property.

Conflict of Interests

The authors declare that there is no conflict of interests regarding the publication of this paper.

Acknowledgments

The authors would like to express their sincere gratitude to MOBI Antenna Technologies (Shenzhen) Company for providing the software package of HFSS and antenna test chamber. This work was supported in part by the Key Program of the National Natural Science Foundation of China under Grant 61032003 and the National Basic Research Program of China under Grant 2009CB320402.

References

[1] J. F. Valenzuela-Valdés, M. A. García-Fernández, A. M. Martínez-González, and D. A. Sánchez-Hernández, "Evaluation of true polarization diversity for MIMO systems," *IEEE Transactions on Antennas and Propagation*, vol. 57, no. 9, pp. 2746–2755, 2009.

[2] P.-S. Kildal and K. Rosengren, "Correlation and capacity of MIMO systems and mutual coupling, radiation efficiency, and diversity gain of their antennas: simulations and measurements in a reverberation chamber," *IEEE Communications Magazine*, vol. 42, no. 12, pp. 104–112, 2004.

[3] K. S. Min, D. J. Kim, and M. S. Kim, "Multi-channel MIMO antenna design for WiBro/PCS band," in *Proceedings of the IEEE International Symposium on Antennas and Propagation Society*, pp. 1225–1228, Honolulu, Hawaii, USA, July 2007.

[4] M. A. Jensen and J. W. Wallace, "A review of antennas and propagation for MIMO wireless communications," *IEEE Transactions on Antennas and Propagation*, vol. 52, no. 11, pp. 2810–2824, 2004.

[5] J. Lee and N. Jindal, "Symmetrie capacity of MIMO downlink channels," in *Proceedings of the IEEE International Symposium on Information Theory (ISIT '06)*, pp. 1031–1035, Seattle, Wash, USA, July 2006.

[6] L. Dong, H. Choo, R. W. Heath Jr., and H. Ling, "Simulation of MIMO channel capacity with antenna polarization diversity," *IEEE Transactions on Wireless Communications*, vol. 4, no. 4, pp. 1869–1873, 2005.

[7] J. Pérez, J. Ibáñez, L. Vielva, and I. Santamaría, "Capacity estimation of polarization-diversity MIMO systems in Urban microcellular environments," in *Proceedings of the 15th IEEE International Symposium on Personal, Indoor and Mobile Radio Communications (PIMRC '04)*, vol. 4, pp. 2730–2734, September 2004.

[8] R. Chair, A. A. Kishk, and K. F. Lee, "Comparative study on different feeding techniques for dual polarized dielectric resonator antennas," in *IEEE Antennas and Propagation Society International Symposium*, pp. 2495–2498, Albuquerque, NM, USA, 2006.

[9] Y. Gao, Z. Feng, and L. Zhang, "Compact CPW-fed dielectric resonator antenna with dual polarization," *IEEE Antennas and Wireless Propagation Letters*, vol. 10, pp. 544–547, 2011.

[10] A. C. K. Mak and C. Rowell, "A low-cost dual-polarized wideband antenna," in *Proceedings of the IEEE International Symposium on Antennas and Propagation Society*, pp. 1478–1479, Orlando, Fla, USA, July 2013.

[11] J. S. Kim, J. H. Yoon, Y. J. Yoon, W.-S. Lee, and C.-G. Kim, "Design of modified dual mode horn antenna to improve E/H-plane radiation pattern symmetry," in *Proceedings of the 17th International Symposium on Antennas and Propagation (ISAP '12)*, pp. 547–550, Nagoys, Japan, November 2012.

[12] F. Gross, *Frontiers in Antennas: Next Generation Design & Engineering*, McGraw-Hill, New York, NY, USA, 2011.

[13] E. A. Soliman, S. Brebels, P. Delmotte, G. A. E. Vandenbosch, and E. Beyne, "Bow-tie slot antenna fed by CPW," *Electronics Letters*, vol. 35, no. 7, pp. 514–515, 1999.

Hindawi Publishing Corporation
International Journal of Antennas and Propagation
Volume 2015, Article ID 370763, 7 pages
http://dx.doi.org/10.1155/2015/370763

Research Article

MIMO Antenna with High Isolation for WBAN Applications

Do-Gu Kang, Jinpil Tak, and Jaehoon Choi

Department of Electronics and Communications Engineering, Hanyang University, 222 Wangsimni-ro, Seongdong-gu, Seoul 133-791, Republic of Korea

Correspondence should be addressed to Jaehoon Choi; choijh@hanyang.ac.kr

Received 18 September 2014; Revised 23 December 2014; Accepted 4 February 2015

Academic Editor: Yuan Yao

A multi-input multi-output (MIMO) antenna with high isolation is proposed for 2.4 GHz ISM band (2.4–2.485 GHz) WBAN applications. The proposed MIMO antenna consists of two PIFA elements and utilizes an isolator composed of a shorted strip and two slits in the ground plane. Although the separation between the two PIFAs is minimized to 8 mm ($0.06\,\lambda_\circ$), isolation performance is improved by virtue of an isolator. To analyze the antenna's performance on a human body, the proposed antenna is placed on a human muscle-equivalent flat phantom and is investigated through simulations. The measured −10 dB reflection coefficient bandwidth of the antenna ranges from 2.11 GHz to 2.6 GHz, and the isolation is lower than −38 dB over the 2.4 GHz ISM band.

1. Introduction

Given the fast progress of wireless communication technologies, wireless body area network (WBAN) systems have received considerable attention for various applications [1, 2]. Because WBAN systems can be placed on or in the human body with high permittivity and conductivity at microwave frequencies, the gain and efficiency of an antenna for WBAN systems can be degraded [3–6]. Furthermore, to operate in WBAN communication environment, the antenna should have compact size, low height, insensitiveness to human body effects, and low specific absorption rate (SAR) [7].

Many researchers have conducted various studies on the performance analysis of on-body WBAN communication systems in the industrial, scientific, and medical (ISM) bands [8–11]. Because of reflections/scatterings that occur in a neighborhood environment and/or on the human body, severe multipath fading can arise in on-body communication links [9]. Multipath fading not only decreases the communication reliability of multisignals but also worsens the efficiency of a WBAN system [12]. To improve communication performance under the influence of multipath fading, a diversity technique such as multiple-input and multiple-output (MIMO) is necessary. Since the independence of the multisignals can be improved by the high isolation of a MIMO antenna, a MIMO technique is frequently used to overcome the deterioration of communication performance due to multipath fading [13].

To achieve high isolation between MIMO antenna elements, an isolator has been used by many researchers [14–17]. A MIMO antenna with a high isolation characteristic is proposed by using a shorted strip and two slits in the ground plane [17]. The antenna has isolation lower than −32 dB for on-body WBAN applications in the 2.4 GHz ISM band. The MIMO antenna utilizes two planar inverted-F antenna (PIFA) elements with lengths of $\lambda/4$ at a resonant frequency to achieve a compact size [18]. The performance of the proposed antenna on the human muscle-equivalent flat phantom is analyzed by examining data such as the S-parameter characteristic, current distribution, radiation pattern, SAR, and envelope correlation coefficient (ECC).

2. Antenna Design and Analysis

2.1. Basic Geometry. The proposed MIMO antenna consists of two PIFAs, a shorted strip, and two slits in a ground plane, as shown in Figure 1. The shorted strip, along with the two slits, acts as an isolator. The PIFAs, which have dimensions of $12 \times 10.5 \times 2\,\text{mm}^3$, are located on a FR4 substrate ($\varepsilon_r = 4.4$) with a 1 mm thickness and an area of $40 \times 40\,\text{mm}^2$. The two

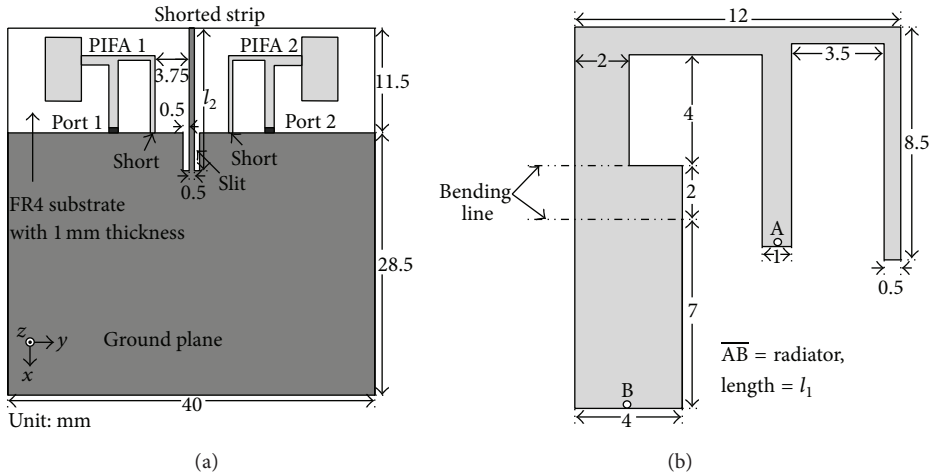

Figure 1: Geometry of the proposed antenna: (a) top view; (b) PIFA.

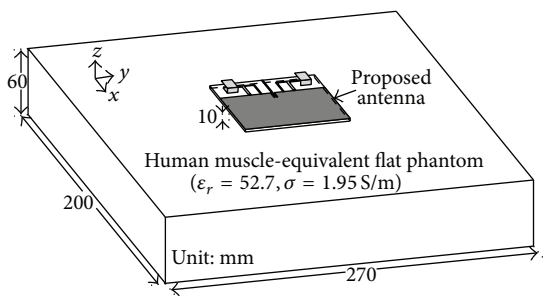

Figure 2: Proposed antenna on the phantom for simulation setup.

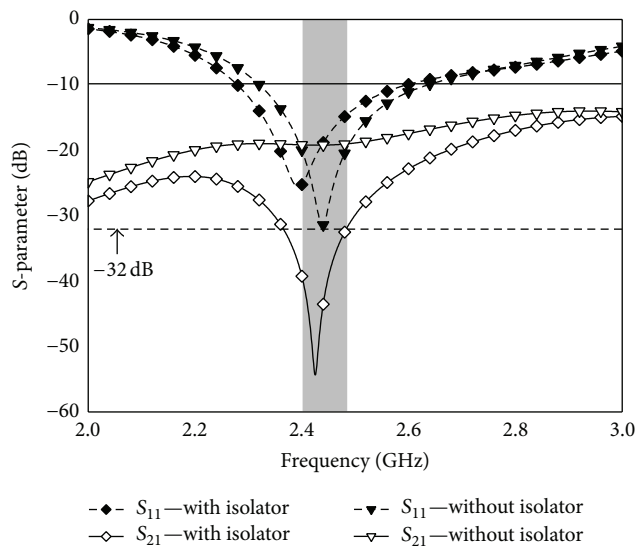

Figure 3: Simulated S-parameter characteristics for the proposed antenna with and without isolator.

PIFAs are symmetrically placed with a separation distance of 8 mm (0.06 $\lambda_\circ$) in the y-axis direction. The isolator and the ground plane are printed on the upper side of the substrate.

To consider the effects on the human body, the simulation setup of an antenna on a human muscle-equivalent flat phantom is illustrated in Figure 2. The phantom, with a volume of 200 × 270 × 60 mm^3, has the relative dielectric constant (ε_r = 52.7) and the conductivity (σ = 1.95 S/m) of human tissue [19]. Considering practical applications such as wearable Bluetooth services, the antenna is placed on the phantom with a separation distance of 10 mm to satisfy the required clearance to assemble the cover [3]. The antenna geometry was designed and analyzed by utilizing the high frequency structure simulator (HFSS 14) [20].

The simulated S-parameter characteristics of the proposed antenna with and without the isolator are compared in Figure 3. The optimized design parameters are l_1 = 27.5 mm and l_2 = 15.5 mm. The proposed antenna has a −10 dB reflection coefficient bandwidth ranging from 2.27 GHz to 2.6 GHz, which fully covers the desired 2.4 GHz ISM band. When the isolator is added between the two PIFAs, the isolation is improved significantly with a slight shift of the resonant frequency. The antenna has isolation below −32 dB in the 2.4 GHz ISM band.

To investigate the effect of the isolator, the simulated current distributions with and without the isolator at 2.4 GHz are shown in Figure 4. By exciting port 1, substantial current is induced at PIFA 2 in the absence of the isolator. After the isolator is added, the induced current on PIFA 2 becomes weak. This is because the impedance of the $\lambda/4$ isolator becomes large at 2.4 GHz so that the current flowing from port 1 to PIFA 2 is blocked by the isolator [21, 22].

2.2. Key Parameter Analysis. The S-parameters of the proposed antenna with respect to a variation in the length (l_1) of the PIFA radiator are shown in Figure 5. As l_1 decreases, the resonance frequency shifts toward a higher frequency, while the isolation is improved. However, as l_1 decreases beyond 27.5 mm, the isolation deteriorates. When l_1 = 27.5 mm, the antenna satisfies the 2.4 GHz ISM band with optimum isolation.

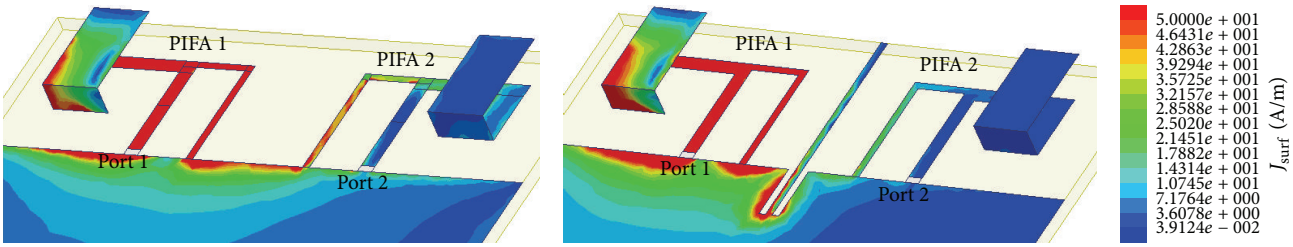

(a) (b)

Figure 4: Simulated current distributions for the proposed antenna at 2.4 GHz (port 1: on, port 2: off): (a) without isolator; (b) with isolator.

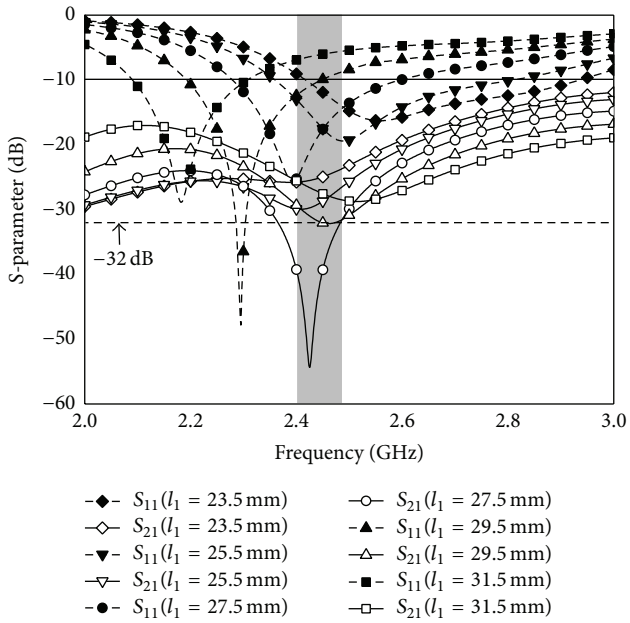

Figure 5: Simulated S-parameters for various values of length l_1 ($l_2 = 15.5$ mm).

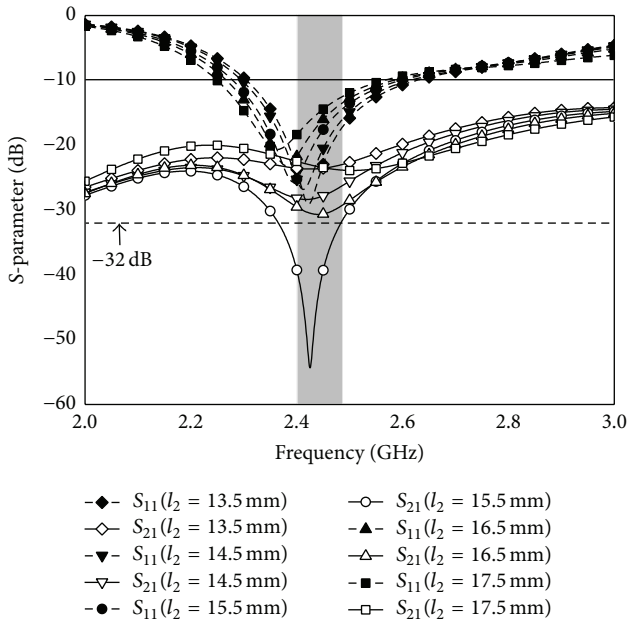

Figure 6: Simulated S-parameters for various values of length l_2 ($l_1 = 27.5$ mm).

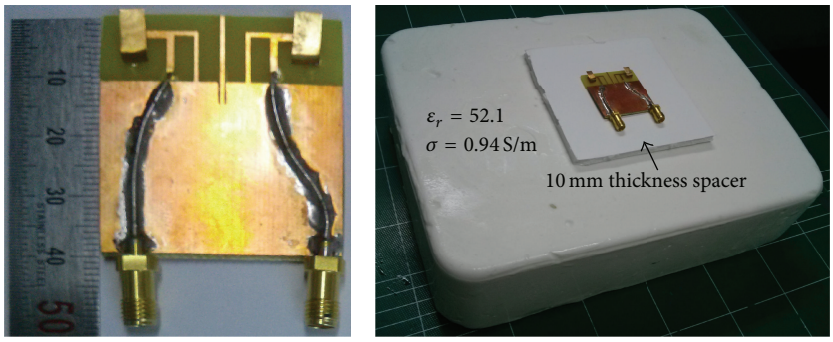

(a) (b)

Figure 7: Fabricated antenna and measurement setup. (a) Fabricated antenna; (b) the antenna on the phantom for measurement setup.

Table 1: Measured peak gain and radiation efficiency.

2.4 GHz	PIFA 1	PIFA 2
Peak gain (dBi)	0.54	0.59
Efficiency (%)	21.34	21.37

In Figure 6, the S-parameters of the proposed antenna with respect to the various lengths (l_2) of the shorted strip are illustrated. A variation in l_2 also changes the slit's length because the tip of the shorted strip is fixed. As l_2 increases, the isolation performance is improved and good impedance matching is obtained. However, after l_2 = 15.5 mm, the isolation degrades. To achieve optimum isolation performance, l_2 = 15.5 mm is chosen.

3. Antenna Performance

Photographs of the fabricated antenna and the human muscle-equivalent flat phantom for the measurement setup are shown in Figure 7 [23]. By utilizing the fabricated phantom (ε_r = 52.1 and σ = 0.94 S/m), the performance of the antenna on the human body can be investigated.

The simulated and measured S-parameter characteristics of the proposed antenna are compared in Figure 8. The measured and simulated results are in reasonably good agreement. The measured −10 dB reflection coefficient bandwidth of the fabricated antenna is 490 MHz from 2.11 GHz to 2.6 GHz, which satisfies the entire 2.4 GHz ISM band. The fabricated antenna has a measured isolation below −38 dB in the 2.4 GHz ISM band.

To analyze the effects on the human body when the proposed antenna operates, the SAR value of the antenna is calculated at 2.4 GHz, as shown in Figure 9. The Federal Communications Commission (FCC) of the United States requires that the SAR be lower than 1.6 W/kg over a volume of 1 g of tissue [24]. The antenna has a SAR of 1.52 W/kg when an input power of 100 mW is applied. Thus, the proposed antenna can be used for low power Bluetooth device applications [25].

The simulated and measured far-field radiation patterns of the proposed antenna on the phantom are compared at

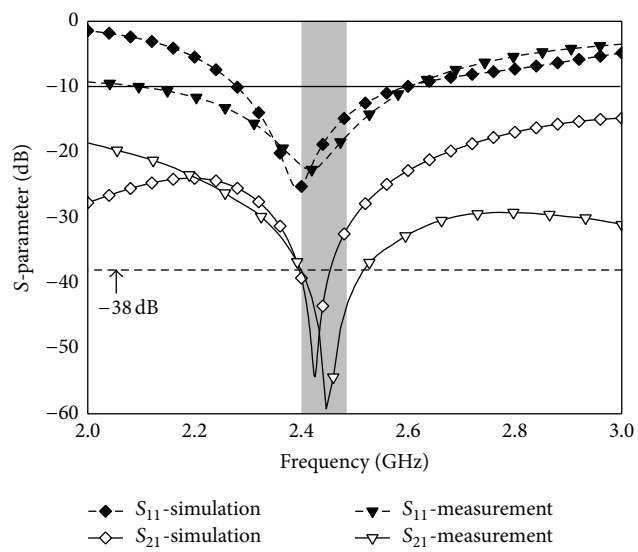

Figure 8: Simulated and measured S-parameter results for the proposed antenna on the human muscle-equivalent flat phantom.

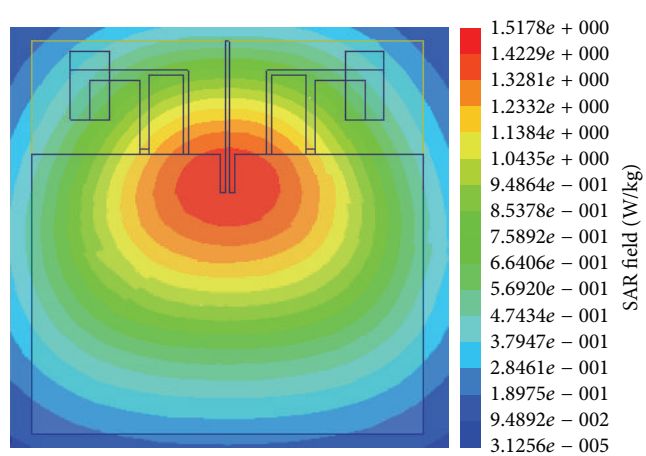

Figure 9: Simulated SAR distribution of the proposed antenna on the phantom at 2.4 GHz (input power: 100 mW).

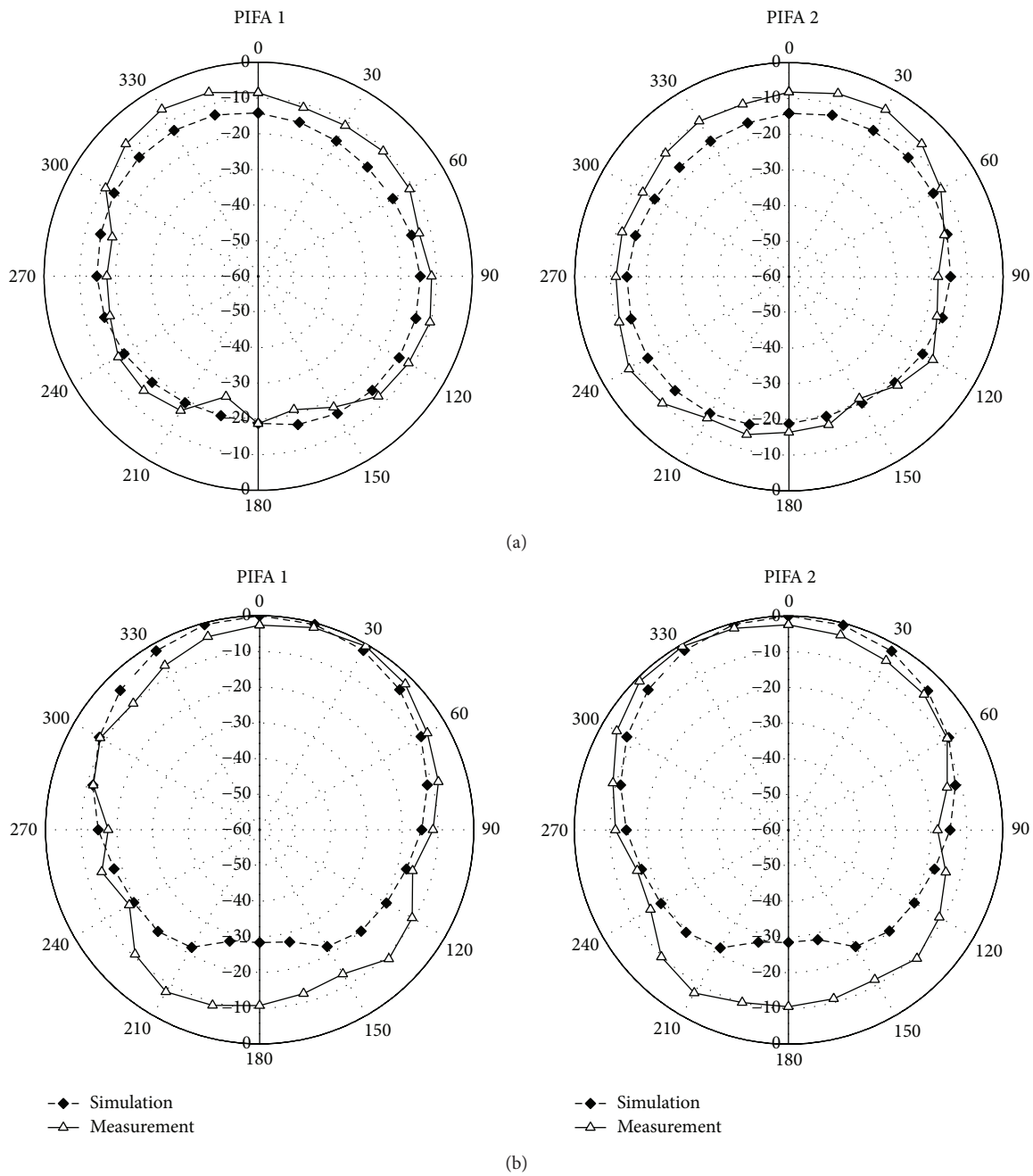

Figure 10: Simulated and measured radiation patterns of the proposed antenna at 2.4 GHz. (a) xy plane; (b) yz plane (σ for simulation: 1.95 S/m, σ for measurement: 0.94 S/m).

2.4 GHz, as shown in Figure 10. The simulated and measured radiation patterns agree very well, except for those in the back radiation direction ($150^\circ \leq \theta \leq 210^\circ$) of the yz plane. The difference between the simulated and measured radiation patterns of the yz plane occurs because the phantom has different conductivity values (conductivity for simulation: 1.95 S/m, conductivity for measurement: 0.94 S/m). Because the radiated field reflected by the phantom with high conductivity used in the simulation is stronger than that of the measurement, the backward radiation decreases. When the conductivity for the simulation becomes 0.94 S/m, the simulated radiation patterns are almost the same as the measured ones, as shown in Figure 11. The radiation patterns of PIFA 1 are somewhat analogous to those of PIFA 2. The antenna has quasi-omnidirectional radiation patterns in the xy plane and has its peak radiation in the outward normal to the phantom surface in the yz plane.

Measured radiation characteristics of the two PIFAs at 2.4 GHz are compared in Table 1. The efficiencies of PIFA 1 and PIFA 2 are 21.34% and 21.37%, respectively.

The envelope correlation coefficient (ECC) is commonly utilized to evaluate the diversity capability of a MIMO

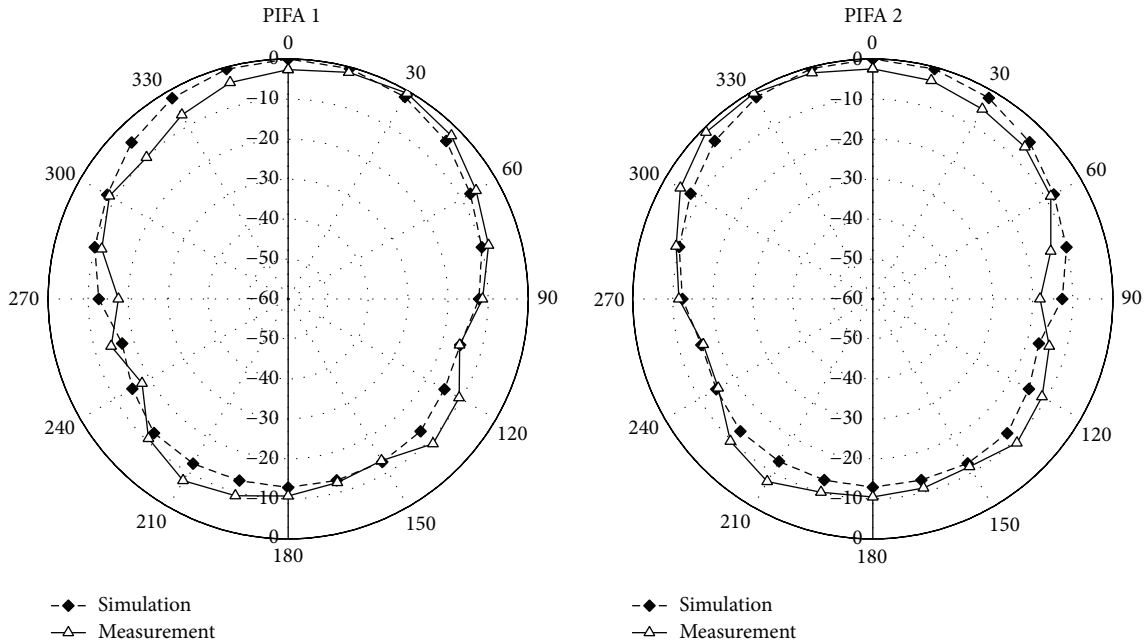

Figure 11: Simulated and measured radiation patterns (yz plane) of the proposed antenna at 2.4 GHz (σ for simulation and measurement: 0.94 S/m).

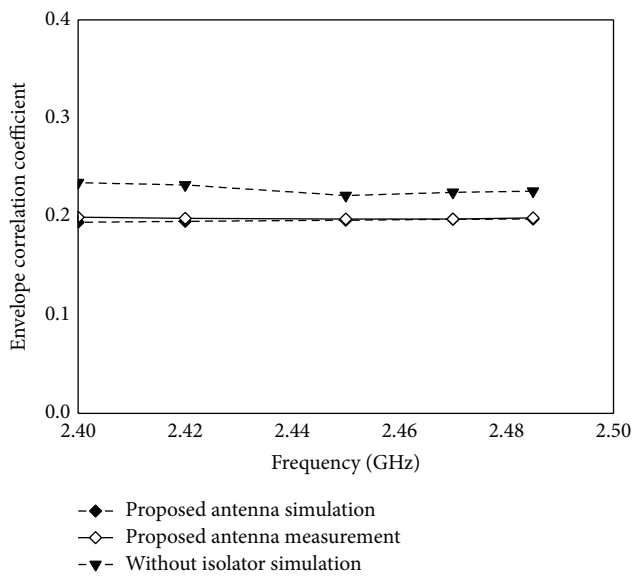

Figure 12: Simulated and measured envelope correlation coefficients of the proposed antenna with and without isolator.

antenna system. The ECC must be computed by using three-dimensional radiation patterns [26]. ECCs computed by simulated radiation patterns and measured radiation patterns are shown in Figure 12. The measured ECC agrees very well with the simulated one. The proposed antenna has an ECC value that is lower than 0.5 in the 2.4 GHz ISM band. When the computed ECCs with and without the isolator are compared, ECC performance improves owing to the improved isolation between PIFA 1 and PIFA 2.

4. Conclusion

A high isolation MIMO antenna is designed to operate in the 2.4 GHz ISM band for WBAN applications. When installed on a human muscle-equivalent flat phantom, the antenna satisfies the −10 dB reflection coefficient bandwidth of the 2.4 GHz ISM band. An isolator, consisting of a shorted strip and two slits, is added between the two PIFAs to improve the isolation. Although the two PIFAs are placed close to

each other with a separation distance of only 8 mm (0.06 λ_o), the antenna exhibits an isolation lower than −38 dB in the 2.4 GHz ISM band. Therefore, the above-mentioned properties prove that the proposed antenna is suitable for WBAN applications.

Conflict of Interests

The authors declare that there is no conflict of interests regarding the publication of this paper.

Acknowledgment

This research was partially supported by the MSIP (Ministry of Science, ICT and Future Planning), Korea, under the ITRC (Information Technology Research Center) support program (NIPA-2014-H0301-14-1017) supervised by the NIPA (National IT Industry Promotion Agency).

References

[1] T. Zasowski, F. Althaus, M. Stager, A. Wittneben, and G. Troster, "UWB for noninvasive wireless body area networks: channel measurements and results," in *Proceedings of the IEEE Conference on Ultra Wideband Systems and Technologies (UWBST '03)*, pp. 285–289, November 2003.

[2] P. S. Hall and Y. Hao, *Antennas and Propagation for Body-Centric Wireless Communications*, Artech House, Norwood, Mass, USA, 2006.

[3] M. U. Rehman, Y. Gao, Z. Wang et al., "Investigation of on-body bluetooth transmission," *IET Microwaves, Antennas and Propagation*, vol. 4, no. 7, Article ID IMAPCH0000040000007000871000001, pp. 871–880, 2010.

[4] C.-P. Deng, X.-Y. Liu, Z.-K. Zhang, and M. M. Tentzeris, "A miniascape-like triple-band monopole antenna for WBAN applications," *IEEE Antennas and Wireless Propagation Letters*, vol. 11, pp. 1330–1333, 2012.

[5] Z. N. Chen, A. Cai, T. S. P. See, X. Qing, and M. Y. W. Chia, "Small planar UWB antennas in proximity of the human head," *IEEE Transactions on Microwave Theory and Techniques*, vol. 54, no. 4, pp. 1846–1856, 2006.

[6] P. S. Hall, Y. Hao, Y. I. Nechayev et al., "Antennas and propagation for on-body communication systems," *IEEE Antennas and Propagation Magazine*, vol. 49, no. 3, pp. 41–58, 2007.

[7] N. Haga, K. Saito, M. Takahashi, and K. Ito, "Characteristics of cavity slot antenna for body-area networks," *IEEE Transactions on Antennas and Propagation*, vol. 57, no. 4, pp. 837–843, 2009.

[8] J. Tak, K. Kwon, S. Kim, and J. Choi, "Dual-band on-body repeater antenna for in-on-on WBAN applications," *International Journal of Antennas and Propagation*, vol. 2013, Article ID 107251, 12 pages, 2013.

[9] A. A. Serra, P. Nepa, G. Manara, and P. S. Hall, "Diversity for body area networks," in *Proceedings of the 29th URSI General Assembly*, pp. 1–4, Chicago, Ill, USA, August 2008.

[10] L. Akhoondzadeh-Asl, I. Khan, and P. S. Hall, "Polarisation diversity performance for on-body communication applications," *IET Microwaves, Antennas & Propagation*, vol. 5, no. 2, pp. 232–236, 2011.

[11] T. Aoyagi, M. Kim, J.-I. Takada, K. Hamaguchi, and R. Kohno, "Numerical simulations for wearable BAN propagation channel during various human movements," *IEICE Transactions on Communications*, vol. 94, no. 9, pp. 2496–2500, 2011.

[12] S. L. Cotton and W. G. Scanlon, "A statistical analysis of indoor multipath fading for a narrowband wireless body area network," in *Proceedings of the IEEE International Symposium on Personal, Indoor and Mobile Radio Communications*, pp. 1–5, IEEE, 2006.

[13] S. Zhang, B. K. Lau, A. Sunesson, and S. He, "Closely-packed UWB MIMO/diversity antenna with different patterns and polarizations for USB dongle applications," *IEEE Transactions on Antennas and Propagation*, vol. 60, no. 9, pp. 4372–4380, 2012.

[14] J. Lee, S. Hong, and J. Choi, "Design of an ultra-wideband mimo antenna for PDA applications," *Microwave and Optical Technology Letters*, vol. 52, no. 10, pp. 2165–2170, 2010.

[15] J.-F. Li, Q.-X. Chu, and T.-G. Huang, "A compact wideband MIMO antenna with two novel bent slits," *IEEE Transactions on Antennas and Propagation*, vol. 60, no. 2, pp. 482–489, 2012.

[16] M. S. Sharawi, A. B. Numan, M. U. Khan, and D. N. Aloi, "A dual-element dual-band MIMO antenna system with enhanced isolation for mobile terminals," *IEEE Antennas and Wireless Propagation Letters*, vol. 11, pp. 1006–1009, 2012.

[17] K. Wang, R. A. M. Mauermayer, and T. F. Eibert, "Compact two-element printed monopole array with partially extended ground plane," *IEEE Antennas and Wireless Propagation Letters*, vol. 13, pp. 138–140, 2014.

[18] Y.-X. Guo, M. Y. W. Chia, and Z. N. Chen, "Miniature built-in multiband antennas for mobile handsets," *IEEE Transactions on Antennas and Propagation*, vol. 52, no. 8, pp. 1936–1944, 2004.

[19] D. L. Means and W. Kwok, "Evaluating compliance with FCC guidelines for human exposure to radiofrequency electromagnetic fields," Supplement C (Edition 01-01) to OET Bulletin 65 (Edition 97-01), Federal Communications Commission Office of Engineering & Technology, 2001.

[20] Ansys High Frequency Structure Simulator (HFSS), ver.14, Ansys Corporation.

[21] M. Ayatollahi, Q. Rao, and D. Wang, "A compact, high isolation and wide bandwidth antenna array for long term evolution wireless devices," *IEEE Transactions on Antennas and Propagation*, vol. 60, no. 10, pp. 4960–4963, 2012.

[22] J.-H. Lim, Z.-J. Jin, C.-W. Song, and T.-Y. Yun, "Simultaneous frequency and isolation reconfigurable MIMO PIFA using pin diodes," *IEEE Transactions on Antennas and Propagation*, vol. 60, no. 12, pp. 5939–5946, 2012.

[23] S.-Y. Lee, W.-B. Seo, K. Kwon, and J.-H. Choi, "The study on implementation of a semi-solid flat phantom with equivalent electrical properties to whole human body at MICS and ISM band," *The Journal of Korean Institute of Electromagnetic Engineering and Science*, vol. 23, no. 1, pp. 101–107, 2012.

[24] IEEE, "IEEE standard for safety levels with respect to human exposure to radio frequency electromagnetic fields, 3 KHz to 300 GHz," IEEE Standard C95, IEEE, 1999.

[25] M. Patel and J. Wang, "Applications, challenges, and prospective in emerging body area networking technologies," *IEEE Wireless Communications*, vol. 17, no. 1, pp. 80–88, 2010.

[26] J.-F. Li, Q.-X. Chu, and T.-G. Huang, "A compact wideband MIMO antenna with two novel bent slits," *IEEE Transactions on Antennas and Propagation*, vol. 60, no. 2, pp. 482–489, 2012.

Hindawi Publishing Corporation
International Journal of Antennas and Propagation
Volume 2015, Article ID 912934, 6 pages
http://dx.doi.org/10.1155/2015/912934

Research Article

Dual-Frequency Two-Element Antenna Array with Suppressed Mutual Coupling

Yantao Yu, Lijun Yi, Xiaoya Liu, Zhaokai Gu, and Nadia Media Rizka

College of Communication Engineering, Chongqing University, Chongqing 400044, China

Correspondence should be addressed to Yantao Yu; yantaoyu@cqu.edu.cn

Received 21 September 2014; Accepted 12 December 2014

Academic Editor: Xinyi Tang

An efficient technique utilizing the defected ground structure (DGS) to suppress the mutual coupling effect of a dual-frequency microstrip antenna array is studied. The proposed dual-frequency DGS beneath two patches includes two circular split ring slots, each of which corresponds to one resonant frequency of the patches. The characteristic of the compact DGS is theoretically and experimentally investigated. The prototypes of the patches arrays with and without the proposed DGS are fabricated. Both the simulated and measured results show that the mutual coupling between array elements has been obviously reduced at the two operating frequency bands with the implementation of the proposed DGS structure.

1. Introduction

The multiple-input multiple-output (MIMO) antenna systems are widely used in new generation of wireless communication systems to accommodate higher data rates and provide increased capacity [1]. However, it is not an easy work to integrate multiple antennas in a small size wireless device while keeping a high level of isolation between antenna elements [2], especially for dual-frequency arrays. This is because the effects of mutual coupling between array elements become more severe when the separation between elements becomes smaller. The mutual coupling effect can cause significant system performance degradation, such as reduction in signal-to-noise ratio and degradation of the synthesized far-field pattern. In addition, the high capacity offered by the MIMO system is reduced if the various signals at the receiver are correlated, where the correlation may arise from the mutual coupling between the transmitting and/or receiving antenna elements [3, 4]. In order to remove or reduce the adverse effects of mutual coupling in compact antenna arrays, different techniques [5, 6] have been proposed in literature.

In signal processing, the coupling matrices [7] can be applied to the received signal vectors from the adaptive arrays to counter the effects of mutual coupling. The relation of the isolation and the array configuration of two nearby antennas in a cellular handset was studied in [8]. Parasitic scatters may also be exploited to reduce the mutual coupling effect in a MIMO array [9]. Various decoupling networks using reactive components [10] or 90° or 180° hybrid couplers [11, 12] have been proposed to increase the isolation between antenna ports. Recently, another effective approach to reduce mutual coupling is to use electromagnetic bandgap (EBG) structures [13] or defected ground structures (DGS) [14] to suppress the surface wave in microstrip substrates. The term "DGS" was first used by Kim and Park in describing a single unit of dumbbell-shaped defect in [15]. The application of DGS to reduce the mutual coupling between two adjacent microstrip patches was first shown in [16]. Most of the designs in literature including the aforementioned ones are for arrays with single operating frequency band. However, dual-frequency operation is preferred for many popular communication standards. Mutual coupling reduction for dual-frequency arrays has attracted many studies. Improvement on dual-band isolation is achieved by using an array of printed capacitively loaded loops (CLLs) on the top side of the board and a complementary CLL structure on the ground plane [17]. However, this design is a bit complicated. A reconfigurable dual-band monopole array with high isolation is given in [18], which exploits the neutralization techniques and uses a switch to control the operating frequency band. The paper

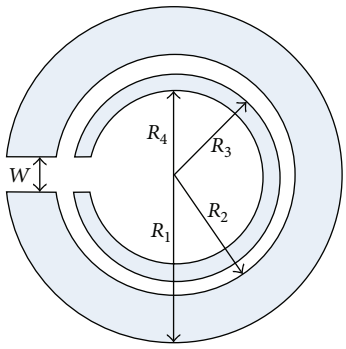

Figure 1: The geometry of the proposed defected ground structure.

[19] describes a procedure to achieve simultaneous decoupling and matching at two frequencies using decoupling network with series and parallel combination of inductors and capacitors.

In this paper, a compact design utilizing the defected ground structure to reduce the mutual coupling between array ports of a dual-frequency patch antenna array is proposed. The proposed dual-frequency DGS beneath two patches includes two circular split ring slots, each of which corresponds to one resonant frequency of the patches. The characteristic of the compact DGS is studied. The prototypes of the patch arrays with and without the proposed DGS are fabricated. Both the simulated and measured results are presented to show the effectiveness of the proposed structure in mutual coupling reduction at two frequency bands.

2. The Dual-Frequency Defected Ground Structure

The proposed defected ground structure is shown in Figure 1. Two cocentered circular split ring slots are etched on the ground plane of a dielectric substrate, which are the parts indicated in grey. The larger split ring slot has an outer radius of R_1 and an inner radius of R_2, while the smaller one has an outer radius of R_3 and an inner radius of R_4. The two split ring slots are resonant and create two stop bands. To study the characteristics of the DSG structure, a microstrip filter model is built in the EM simulator HFSS and the fabricated one is shown in Figure 2. The substrate is FR4 material with dielectric constant of $\varepsilon_r = 4.4$ and thickness of 1.6 mm, while the 50 Ω microstrip line has a width of 3 mm. The performance of the filter is studied by changing the dimensions of the split ring slots. Figure 3 shows the transmission coefficients of the filter with various values of R_1. It can be seen that the lower stop-band frequency decreases with the increase of R_1, while the upper stop-band frequency remains stable. The parameter R_2 has similar effect on the performance of the filter as R_1 as they determine the width of the larger split ring. Similarly, the transmission coefficients of the filter with different R_3 are plotted in Figure 4. It is obvious that as R_3 increases, the upper stop-band frequency will decrease and the lower stop-band frequency keeps unchanged. According to our study, the variation of R_4 also influences the upper stop-band much.

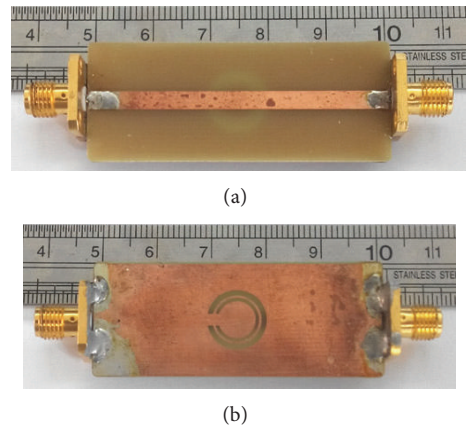

(a)

(b)

Figure 2: The fabricated microstrip filter with DGS. (a) Top view; (b) bottom view.

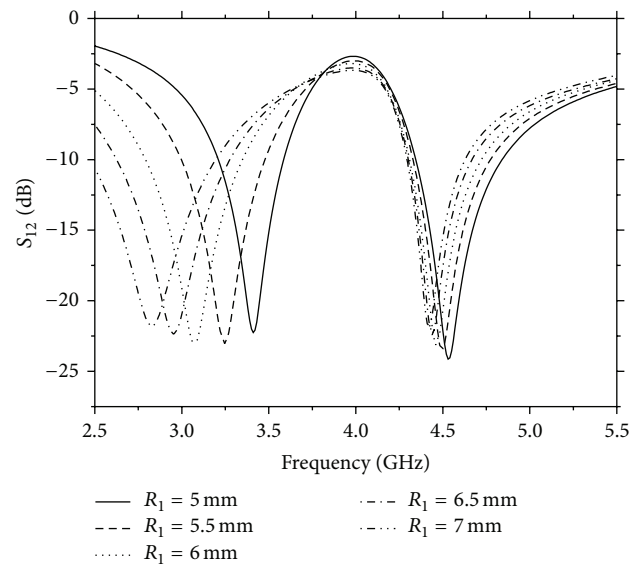

Figure 3: The transmission coefficient of the filter with variation of R_1.

By properly choosing the dimensions of the DGS structure, the desired band rejection characteristic can be obtained. Figure 5 shows the simulated and measured S-parameters of the band-stop filter with $R_1 = 5.2$ mm, $R_2 = 4.2$ mm, $R_3 = 3.9$ mm, $R_4 = 3.1$ mm, and $W = 2$ mm. It is obvious that the band-stop filter has two stop bands at 3.35 GHz and 4.5 GHz.

3. Patch Array with the Proposed DGS

The proposed DGS structure can be implemented in a MIMO antenna array to reduce the mutual coupling. Two coaxial feed rectangular patch antennas with dual operating frequencies at 3.35 GHz and 4.5 GHz are designed, as shown in Figure 6 (without the ring slots). The substrate used for the patches is the same as the one used in filter design. The dimensions of the patch are $W_1 = 102$ mm, $L_1 = 80$ mm, $W_2 = 20$ mm, $L_2 = 25.2$ mm, and $W_3 = 6$ mm, $L_3 = 6$ mm.

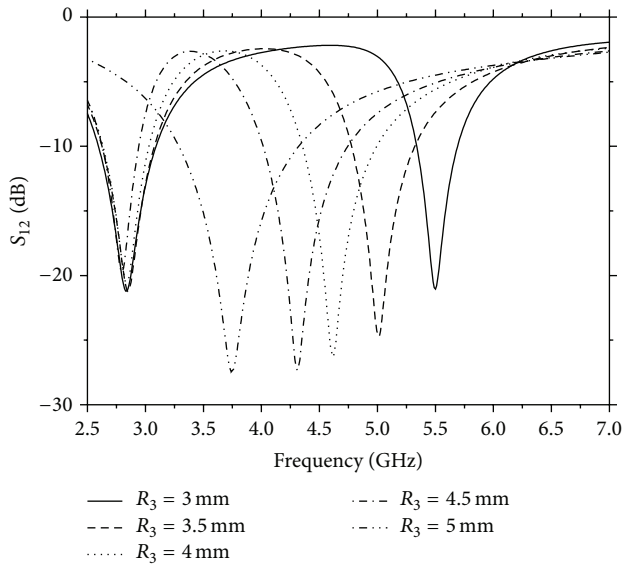

Figure 4: The transmission coefficient of the filter with variation of R_3.

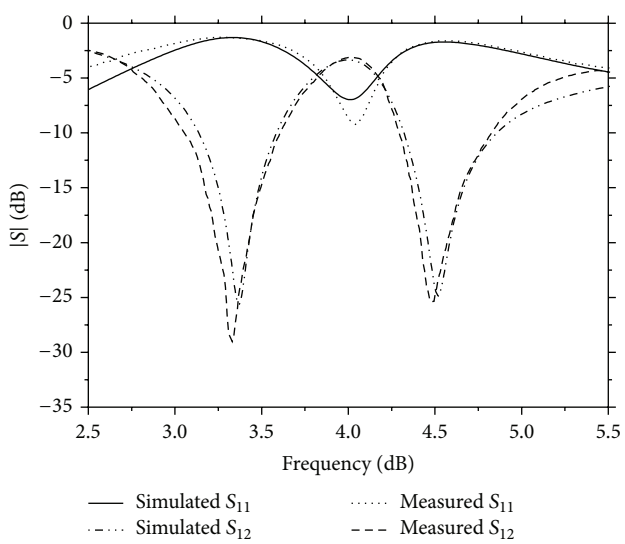

Figure 5: The S-parameters of the filter with optimized dimensions.

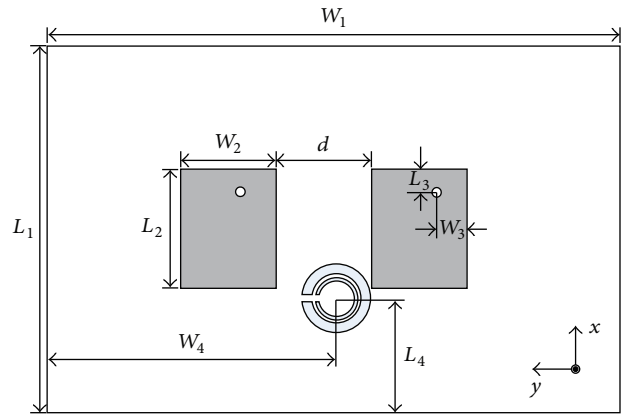

Figure 6: The geometry of the patch array.

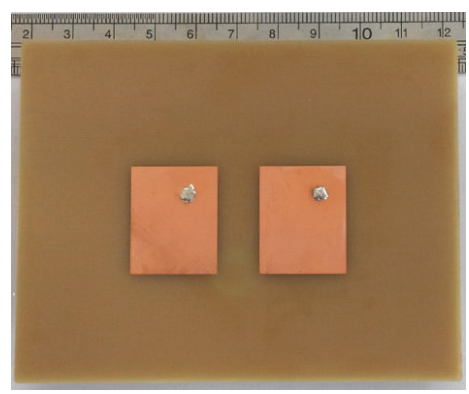

(a)

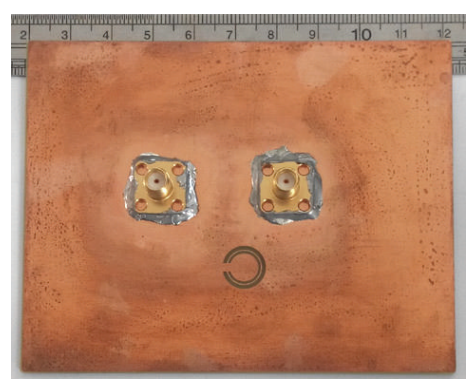

(b)

Figure 7: The prototype of the patch array. (a) Top view without DGS; (b) bottom view with DGS.

The edge to edge distance between the two patches is $d = 10$ mm. The prototype of the patch array is shown in Figure 7(a). Figure 8 shows the simulated and measured S-parameters of the dual-frequency patch array. Although the two patches are not strictly symmetric about the center of the substrate, they have almost the same reflection coefficients in the design according to our simulation and measurement. Therefore, only S_{11} and S_{12} are plotted in Figure 8. It can be seen from the plot that the array has two resonant frequencies at 3.35 GHz and 4.5 GHz, respectively. The measurement agrees well with the simulation. It is also noted that the coupling coefficient is about 19 dB at 3.35 GHz and 15 dB at 4.5 GHz.

To reduce the mutual coupling, the proposed DGS structure is etched in the ground plane of the patches, as shown in Figure 7(b). The center position of the DGS is at $W_4 = 47.9$ mm and $L_4 = 25.1$ mm. The S-parameters of the patch array with DGS are plotted in Figure 9. Since the two antennas are asymmetric after implementing the DGS in the ground plane, the S_{11} and S_{22} are not completely coinciding with each other, but the two patches are still operating in the two bands of the array. It can be seen from Figure 9 that the measured coupling coefficient remains below −20 dB across

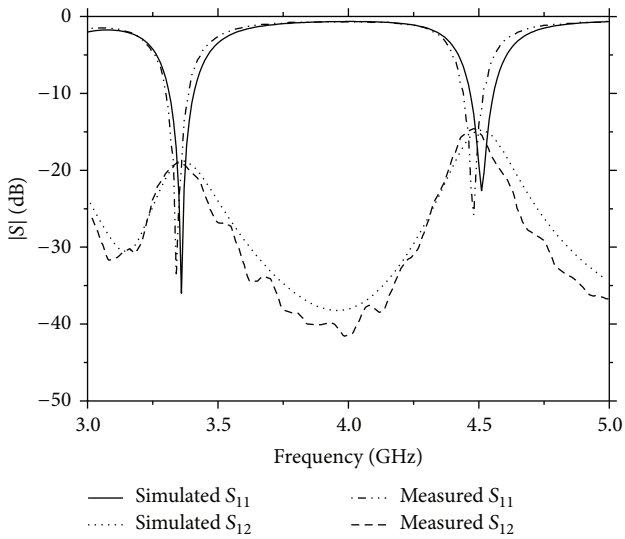

Figure 8: The S-parameters of the patch array without DGS.

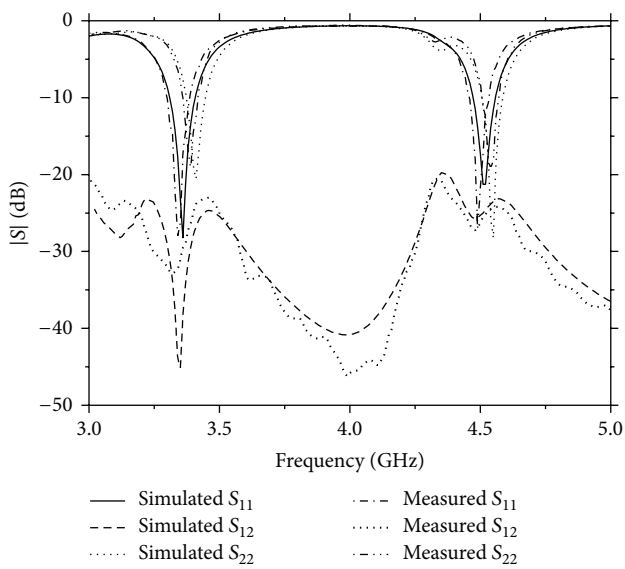

Figure 9: The S-parameters of the patch array with DGS.

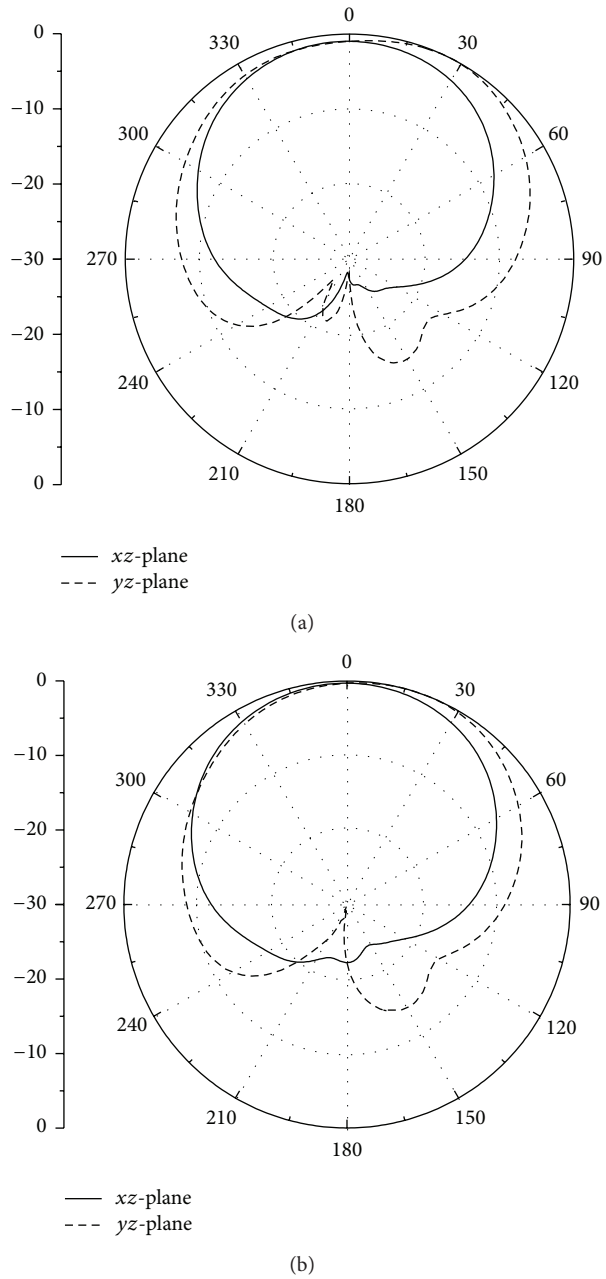

Figure 10: The simulated radiation pattern of the patch array at 3.35 GHz. (a) Without DGS; (b) with DGS.

the two frequency bands and has been reduced to −33 dB at 3.35 GHz and −27 dB at 4.5 GHz. The simulated normalized radiation patterns of the patch array at 3.35 GHz and 4.5 GHz are plotted in Figures 10 and 11, respectively. The coordinate system is shown in Figure 6. It is obvious that the radiation patterns of the patch array remain in their general shapes before and after implementing the defected ground structure.

Correlation coefficient is an important parameter in MIMO performance evaluation. By assuming uniform external signal source distribution, the envelope correlation coefficient (ECC) based on the S-parameters of an array can be calculated using [20]

$$\rho_e(1,2) = \frac{\left|S_{11}^* S_{21} + S_{12}^* S_{22}\right|^2}{\left(1 - \left|S_{11}\right|^2 - \left|S_{21}\right|^2\right)\left(1 - \left|S_{22}\right|^2 - \left|S_{12}\right|^2\right)}. \quad (1)$$

If the antenna efficiencies are known in addition to the S-parameters, the correlation coefficients can be calculated using the method given in [21]. Figure 12 shows the envelope correlation of the patch array with and without DGS using (1). It can be seen that the envelope correlation in the frequency band of interest is very low, which means that the antenna array has good spatial diversity and is suitable for MIMO systems.

4. Conclusion

A compact defected ground structure using double circular split ring slots has been presented to reduce the mutual

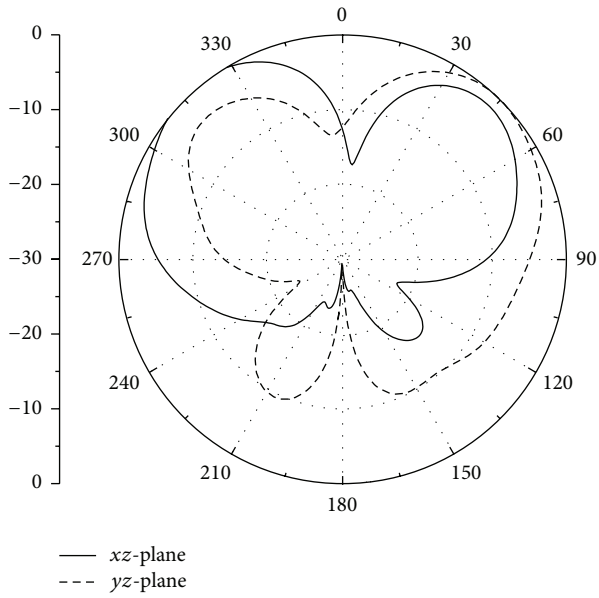

(a)

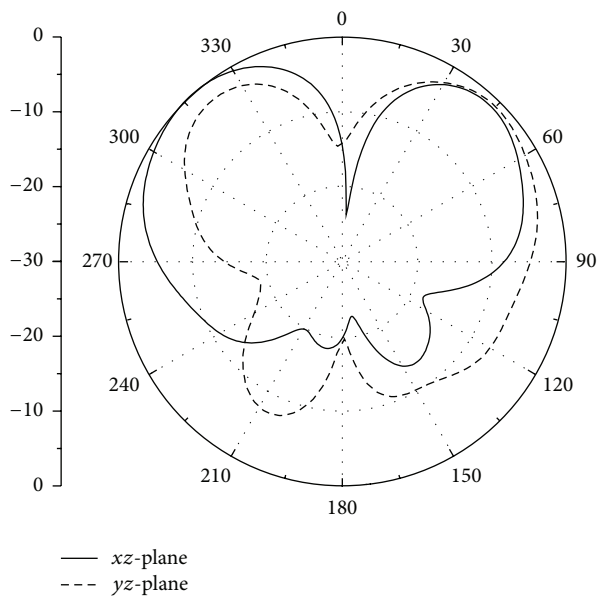

(b)

Figure 11: The simulated radiation pattern of the patch array at 4.5 GHz. (a) Without DGS; (b) with DGS.

coupling between array ports of a dual-frequency patch antenna array. The radii of the slots control the stop-band frequencies. The simulated and measured results of a two-patch array show that the mutual coupling effect between array elements has been obviously reduced. The resulted array has high port isolation and is suitable for MIMO applications.

Conflict of Interests

The authors declare that there is no conflict of interests regarding the publication of this paper.

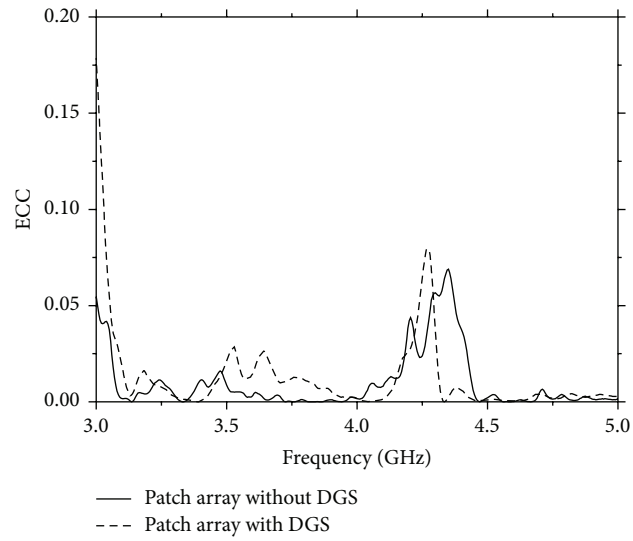

Figure 12: The measured envelope correlation of the patch array with and without DGS.

Acknowledgments

This work was supported in part by the National Natural Science Foundation of China (Grant 61101024), the Natural Science Foundation Project of CQ CSTC (Grant CSTC, 2011BB2070), the Fundamental Research Funds for the Central Universities (Grant nos. CDJZR12160013 and 106112014CDJZR165504), and the sharing fund of Chongqing University's large-scale equipment (Grant 2013121556).

References

[1] M. A. Jensen and J. W. Wallace, "A review of antennas and propagation for MIMO wireless communications," *IEEE Transactions on Antennas and Propagation*, vol. 52, no. 11, pp. 2810–2824, 2004.

[2] A. C. K. Mak, C. R. Rowell, and R. D. Murch, "Isolation enhancement between two closely packed antennas," *IEEE Transactions on Antennas and Propagation*, vol. 56, no. 11, pp. 3411–3419, 2008.

[3] R. Janaswamy, "Effect of element mutual coupling on the capacity of fixed length linear arrays," *IEEE Antennas and Wireless Propagation Letters*, vol. 1, pp. 157–160, 2002.

[4] P. N. Fletcher, M. Dean, and A. R. Nix, "Mutual coupling in multi-element array antennas and its influence on MIMO channel capacity," *Electronics Letters*, vol. 39, no. 4, pp. 342–344, 2003.

[5] J. W. Wallace and M. A. Jensen, "Mutual coupling in MIMO wireless systems: a rigorous network theory analysis," *IEEE Transactions on Wireless Communications*, vol. 3, no. 4, pp. 1317–1325, 2004.

[6] H. T. Hui, "A practical approach to compensate for the mutual coupling effect in an adaptive dipole array," *IEEE Transactions on Antennas and Propagation*, vol. 52, no. 5, pp. 1262–1269, 2004.

[7] H. Steyskal and J. S. Herd, "Mutual coupling compensation in small array antennas," *IEEE Transactions on Antennas and Propagation*, vol. 38, no. 12, pp. 1971–1975, 1990.

[8] Z. Li and Y. Rahmat-Samii, "Optimization of PIFA-IFA combination in handset antenna designs," *IEEE Transactions on Antennas and Propagation*, vol. 53, no. 5, pp. 1770–1778, 2005.

[9] Z. Li, Z. Du, M. Takahashi, K. Saito, and K. Ito, "Reducing mutual coupling of MIMO antennas with parasitic elements for mobile terminals," *IEEE Transactions on Antennas and Propagation*, vol. 60, no. 2, pp. 473–481, 2012.

[10] S. Dossche, S. Blanch, and J. Romeu, "Optimum antenna matching to minimise signal correlation on a two-port antenna diversity system," *Electronics Letters*, vol. 40, no. 19, pp. 1164–1165, 2004.

[11] J. C. Coetzee and Y. Yu, "Port decoupling for small arrays by means of an eigenmode feed network," *IEEE Transactions on Antennas and Propagation*, vol. 56, no. 6, pp. 1587–1593, 2008.

[12] T.-I. Lee and Y. E. Wang, "Mode-based information channels in closely coupled dipole pairs," *IEEE Transactions on Antennas and Propagation*, vol. 56, no. 12, pp. 3804–3811, 2008.

[13] F. Yang and Y. Rahmat-Samii, "Microstrip antennas integrated with electromagnetic band-gap (EBG) structures: a low mutual coupling design for array applications," *IEEE Transactions on Antennas and Propagation*, vol. 51, no. 10, pp. 2936–2946, 2003.

[14] C.-S. Kim, J.-S. Lim, S. Nam, K.-Y. Kang, and D. Ahn, "Equivalent circuit modelling of spiral defected ground structure for microstrip line," *Electronics Letters*, vol. 38, no. 19, pp. 1109–1110, 2002.

[15] C.-S. Kim, J.-S. Park, D. Ahn, and J.-B. Lim, "A novel 1-D periodic defected ground structure for planar circuits," *IEEE Microwave and Wireless Components Letters*, vol. 10, no. 4, pp. 131–133, 2000.

[16] D. Guha, S. Biswas, M. Biswas, J. Y. Siddiqui, and Y. M. M. Antar, "Concentric ring-shaped defected ground structures for microstrip applications," *IEEE Antennas and Wireless Propagation Letters*, vol. 5, no. 1, pp. 402–405, 2006.

[17] M. S. Sharawi, A. B. Numan, and D. N. Aloi, "Isolation improvement in a dual-band dual-element MIMO antenna system using capacitively loaded loops," *Progress in Electromagnetics Research*, vol. 134, pp. 247–266, 2013.

[18] Q. Luo, J. R. Pereira, and H. M. Salgado, "Reconfigurable dual-band C-shaped monopole antenna array with high isolation," *Electronics Letters*, vol. 46, no. 13, pp. 888–889, 2010.

[19] J. C. Coetzee, "Dual-frequency decoupling networks for compact antenna arrays," *International Journal of Microwave Science and Technology*, vol. 2011, Article ID 249647, 3 pages, 2011.

[20] J. Thaysen and K. B. Jakobsen, "Envelope correlation in (N, N) MIMO antenna array from scattering parameters," *Microwave and Optical Technology Letters*, vol. 48, no. 5, pp. 832–834, 2006.

[21] H. Li, X. Lin, B. K. Lau, and S. He, "Equivalent circuit based calculation of signal correlation in lossy MIMO antennas," *IEEE Transactions on Antennas and Propagation*, vol. 61, no. 10, pp. 5214–5222, 2013.

Hindawi Publishing Corporation
International Journal of Antennas and Propagation
Volume 2015, Article ID 851904, 9 pages
http://dx.doi.org/10.1155/2015/851904

Research Article

A Novel Metamaterial MIMO Antenna with High Isolation for WLAN Applications

Nguyen Khac Kiem,[1] Huynh Nguyen Bao Phuong,[2] Quang Ngoc Hieu,[3] and Dao Ngoc Chien[4]

[1] *Hanoi University of Science and Technology, Hanoi 100000, Vietnam*
[2] *Quy Nhon University, Binh Dinh 820000, Vietnam*
[3] *Chuo University, Tokyo 1920393, Japan*
[4] *Ministry of Science and Technology, Hanoi 100000, Vietnam*

Correspondence should be addressed to Nguyen Khac Kiem; kiem.nguyenkhac@hust.edu.vn

Received 11 September 2014; Revised 24 December 2014; Accepted 8 January 2015

Academic Editor: Xinyi Tang

A compact 2 × 2 metamaterial-MIMO antenna for WLAN applications is presented in this paper. The MIMO antenna is designed by placing side by side two single metamaterial antennas which are constructed based on the modified composite right/left-handed (CRLH) model. By adding another left-handed inductor, the total left-handed inductor of the modified CRLH model is increased remarkably in comparison with that of conventional CRLH model. As a result, the proposed metamaterial antenna achieves 60% size reduction in comparison with the unloaded antenna. The MIMO antenna is electrically small (30 mm × 44 mm) with an edge-to-edge separation between two antennas of $0.06\lambda_0$ at 2.4 GHz. In order to reduce the mutual coupling of the antenna, a defected ground structure (DGS) is inserted to suppress the effect of surface current between elements of the proposed antenna. The final design of the MIMO antenna satisfies the return loss requirement of less than −10 dB in a bandwidth ranging from 2.38 GHz to 2.5 GHz, which entirely covers WLAN frequency band allocated from 2.4 GHz to 2.48 GHz. The antenna also shows a high isolation coefficient which is less than −35 dB over the operating frequency band. A good agreement between simulation and measurement is shown in this context.

1. Introduction

Recently, social demand on multimedia communication has been rapidly increasing resulting in development of modern wireless communication systems such as Wi-Fi, WiMAX, and 3G/4G. Along with these applications, modern antennas are required to have small size and light weight. However, the typical antennas are usually large in size due to the operating wavelength, so they are difficult to meet the requirements of modern antennas. There are several techniques used to decrease the size of antenna, such as incorporating a shorting pin in a microstrip patch [1], using short circuit [2], and cutting slots in radiating patch [3, 4], by partially filled high permittivity substrate [5] or by Fractal microstrip patch configuration [6]. Besides, transmission line metamaterial (TL-MM) [7] is one of the methods that provides a conceptual way for implementing small resonant antenna [8–15]. The first proposals of using TL-MM structures at resonance to implement small sprinted antennas have been documented in [9, 10].

Wireless LANs have experienced phenomenal growth during the past several years. The new WLANs standard (IEEE 802.11n) promises both higher data rates and increases reliability. This standard is based on MIMO communication technology which has received much attention as a practical method to substantially increase wireless channel capacity without additional power and spectrum. A multiple antenna system is needed for MIMO system. However, it is difficult to integrate two or more antennas in a mobile device. There are two critical factors for MIMO antenna system. One is total size of antenna system with a limited space of mobile device. In such a way the antenna elements must be compact and

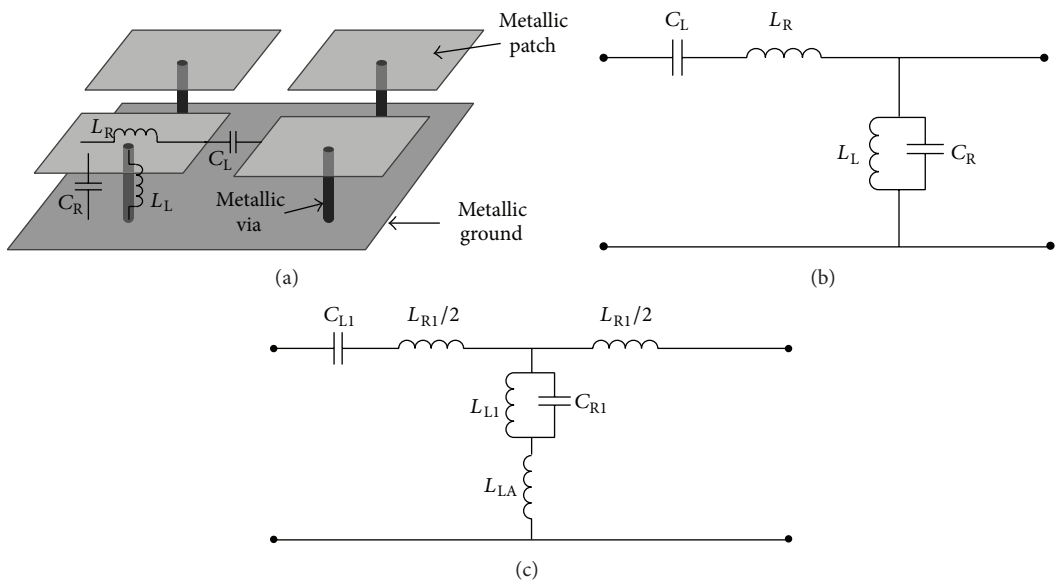

Figure 1: CRLH transmission line: (a) mushroom-like EBG model, (b) equivalent circuit of unit cell, and (c) equivalent circuit of proposed metamaterial antenna.

be put very close. The other factor is the isolation between antenna elements. Due to the close space between antenna elements, the coupling coefficient among radiating elements is very high. This will degrade the performance of MIMO system. Therefore, it will be a real challenging task to design a MIMO antenna with small size while obtaining a very high isolation coefficient.

In this paper, a very compact metamaterial MIMO antenna is proposed. The MIMO antenna consists of two antennas which are based on composite left/right handed (CLRH) transmission lines for reducing the antenna dimension. In the proposed configuration, a defected ground structure (DGS) is employed to increase the isolation between two antenna elements. Thus, a novel metamaterial MIMO antenna is proposed which has a high isolation with only 7.5 mm ($0.06\lambda_0$) distance between antenna elements. This antenna is built on a FR4 substrate with total volume of $30 \times 44 \times 1.6\,\text{mm}^3$ and has very compact radiating elements with total size of $8.92 \times 32.6\,\text{mm}^2$ and operates at the frequency band of 2.38–2.5 GHz while the values of isolation coefficients are below −35 dB over operating frequency band.

The rest of this paper is organized as follow. In Section 2, detailed designs of the single metamaterial antenna are presented. The proposed MIMO antenna is then introduced in both cases of initial and final design. The simulated and measured results are shown in Section 3, while some conclusions are provided in Section 4.

2. Design of Metamaterial MIMO Antenna

In this work, the design of the antenna is divided into two parts. In the first one, a metamaterial antenna is designed for WLAN frequency ranging from 2.4 GHz to 2.48 GHz. In the second part, the two identical single metamaterial antennas are utilized as elements to form a 2 × 2 MIMO antenna. Finally, the defected ground structure is implemented to diminish the mutual coupling of the antennas.

2.1. Design of Single Metamaterial Antenna. The configuration of metamaterial antenna is shown in Figure 2(a). The antenna is printed on a low-cost FR4 substrate with the thickness of 1.6 mm, dielectric constant ε of 4.4, and loss tangent $\tan\delta$ of 0.02. As a reference comparison, an unloaded microstrip fed rectangular strip with the length of l_1 is chosen as the monopole radiating element. In order to maintain compact electrical length while decreasing the operating frequencies, the monopole antenna is constructed by a modified CRLH single-cell.

The model of conventional CRLH transmission line is shown in Figure 1(a). This is a mushroom-like EBG which can be interpreted by equivalent circuit depicted in Figure 1(b). From this figure, the serial left-handed (LH) capacitor (C_L) is created by two adjacent metallic patches placed on the top surface of the structure while the shunt LH inductor (L_L) created by the current flows from the metallic patch to ground plane through metallic via. Moreover, the serial right-handed (RH) inductor (L_R) is formed by the metallic patch and the shunt RH capacitor (C_R) is created due to the parallel arrangement of metallic patch and ground plane.

The equivalent circuit of proposed metamaterial antenna is shown in Figure 1(c). In this design, the metamaterial-loading is carried out in an asymmetric fashion, where serial LH capacitor (C_{L1}) is formed between two strips separated by a distance s_1 (as shown in Figure 2(a)) while the shunt LH inductor (L_{L1}) is formed similarly to the shunt LH one shown in Figure 1(b). Moreover, the additional LH inductor (L_{LA}) is built up by meandered strips which connect the structure and the ground plane. Regarding RH components, the serial RH inductor (L_{R1}) is formed by the main patch with length of l_1 and shunt RH capacitor (C_{R1}) is formed similarly

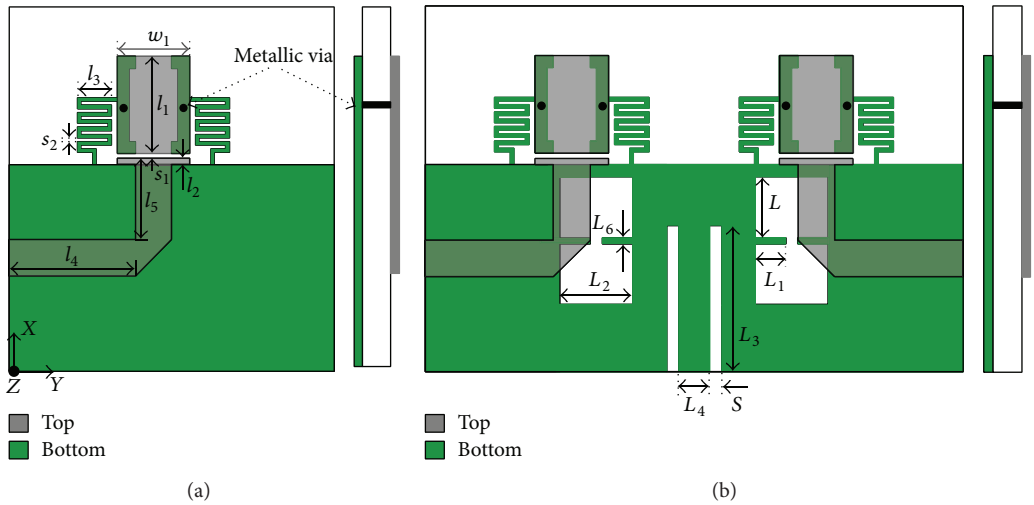

Figure 2: Configuration of the proposed antennas: (a) single metamaterial antenna and (b) metamaterial MIMO antenna.

Table 1: Dimensions of single metamaterial antenna.

l_1	8 mm	l_4	10.5 mm	s_1	0.42 mm
l_2	0.5 mm	l_5	6.7 mm	s_2	0.3 mm
l_3	2.8 mm	w_1	6 mm		

Table 2: Dimensions of metamaterial MIMO antenna.

L	5 mm	L_3	12 mm	S	2.5 mm
L_1	2.5 mm	L_4	1 mm		
L_2	6 mm	L_6	0.5 mm		

to the RH components of conventional CRLH model. As a result, a single metamaterial antenna is proposed with the size of radiating element of $8.92 \times 12.6\,\text{mm}^2$ ($0.07\lambda_0 \times 0.1\lambda_0$ at 2.4 GHz) and printed in a substrate with two dimensions of $27 \times 30\,\text{mm}^2$. Finally, the center resonant frequency of proposed metamaterial antenna is defined as follows:

$$f_C = \frac{1}{2\pi\sqrt{(L_{\text{L1}} + L_{\text{LA}})\,C_{\text{R1}}}}. \quad (1)$$

2.2. Design of Metamaterial MIMO Antenna. In this design, a MIMO model is constructed by placing two single antennas side by side at the distance of 20 mm ($0.16\lambda_0$ at 2.4 GHz) from center-to-center or 7.5 mm ($0.06\lambda_0$ at 2.4 GHz) from edge-to-edge, making the overall the dimension of this design very compact. The layout of the MIMO antenna is shown in Figure 2(b). In order to increase the isolation between elements of MIMO antenna, a defected ground structure is etched in a part of ground between two elements. Firstly, two parallel slots are etched on the ground plane. As a result, the MIMO antenna satisfies the isolation requirement while the operating frequencies were shifted compared to the WLAN frequency band. Therefore, two I-shaped slots which are used as an impedance matching circuit are etched on the metallic ground (as shown in Figure 2(b)). The final MIMO antenna system is proposed with total size of radiating elements of $8.92 \times 32.6\,\text{mm}^2$ and satisfies all requirements of MIMO system with very high isolation between antenna elements. All the dimensions of the proposed single metamaterial antenna and MIMO antenna are given in Tables 1 and 2, respectively.

3. Results and Discussions

The performance of the proposed antennas is discussed in detail in terms of simulation and measurement results.

3.1. Single Metamaterial Antenna. As mentioned in Section 2, the resonant frequency of proposed metamaterial antenna depends on the meandered strip length which is controlled by tuning the length l_3 as well as the gap between strip steps s_2. The simulated S_{11} results of the single metamaterial antenna with different values of l_3 and s_2 are shown in Figure 3. In Figure 3, the resonant frequency reduces with the increasing the value of l_3 and s_2. Actually, the increase of l_3 and s_2 will lead to the increase of the additional LH inductor L_{LA} and therefore making the decrease of the resonant frequency. This is entirely consistent with formula (1). The optimized bandwidth is obtained when the l_3 and s_2 are set at 2.8 mm and 0.3 mm, respectively. It can be seen from Figure 7 that the bandwidth of the antenna defined by the S_{11} less than −10 dB entirely covers the WLAN frequency range, which is allocated from 2.4 to 2.48 GHz.

The size reduction of the proposed antenna is carried out by taking the simulated S_{11} of antennas in case of loaded (proposed antenna) and unloaded (conventional antenna). The two antennas are given the same dimensions of substrate layer and radiation elements. As can be seen from Figure 4, the resonant frequency of the unloaded antenna centers at 6 GHz while the resonant one of the proposed antenna is maintained at 2.44 GHz. It is clear that the proposed antenna exhibits smaller resonant frequency than the conventional one. In this case, the proposed antenna achieves 60% size reduction in comparison with the conventional one.

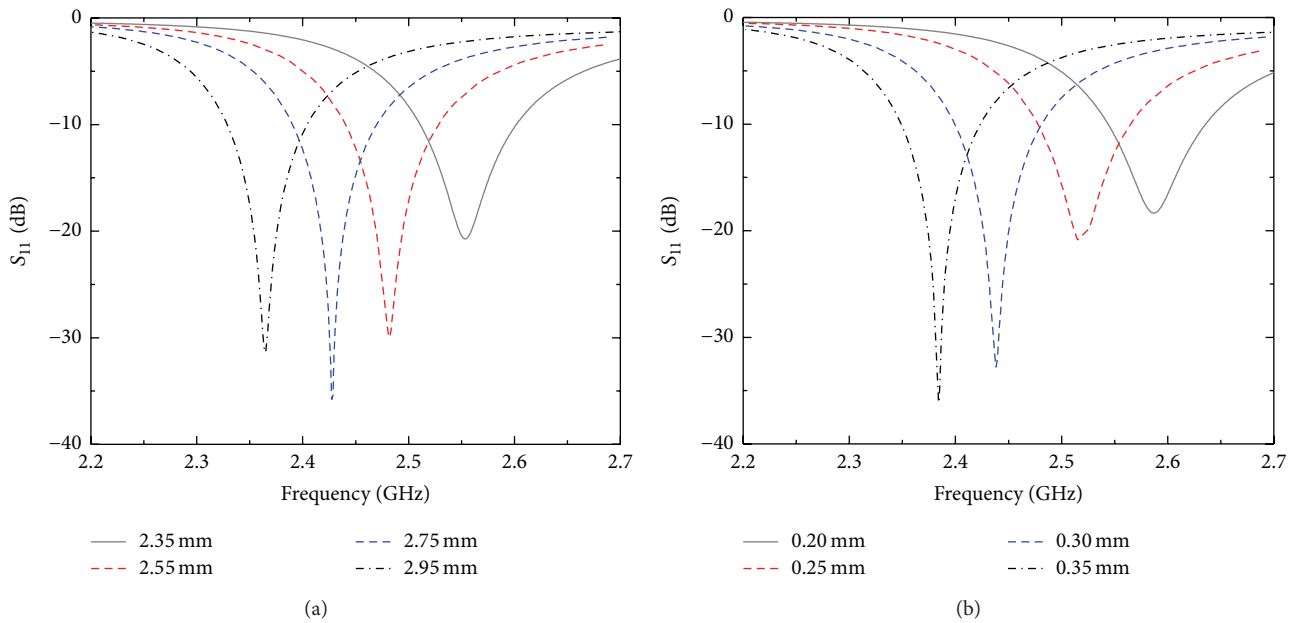

Figure 3: Simulated S_{11} of single metamaterial antenna for different values of (a) l_3 and (b) s_2.

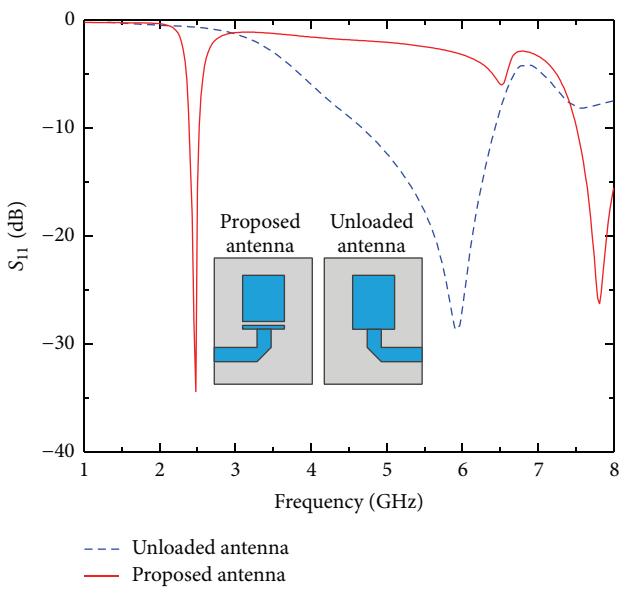

Figure 4: Simulated S_{11} of unloaded and proposed antennas.

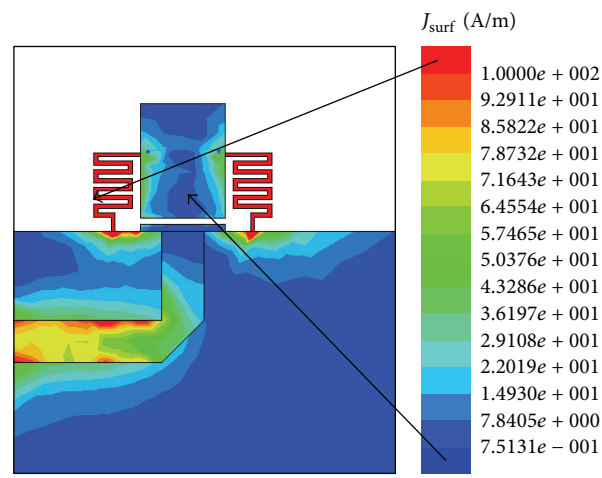

Figure 5: Surface current distribution on single antenna at 2.44 GHz.

Current distributions of the metamaterial antenna at the center frequency of WLAN are exhibited in Figure 5. As observed in Figure 5, the current distribution on antenna at 2.44 GHz mainly focuses on the meandered strips instead of on the radiating patch as the principle of microstrip antenna.

The radiation pattern of single antenna at the center frequency of 2.44 GHz is plotted in Figure 6. The solid lines display the E-plane and the dotted lines represent H-plane. It can be observed that the single antenna possesses an isotropic radiation pattern confirming its operation in the fundamental resonant mode. Therefore, its gain is small with the maximum total gain of 1.4 dB.

Finally, the fabricated single metamaterial antenna is presented in Figure 13. The simulated and measured results of S_{11} of single metamaterial antenna is shown in Figure 7. From this figure, it can be observed that the antenna can operate over the range spreading from 2.4 GHz to 2.48 GHz and from 2.405 GHz to 2.495 GHz in simulation and measurement, respectively.

3.2. Metamaterial MIMO Antenna. The simulated results of reflection coefficients of the initial MIMO antenna (without DGS) are shown in Figure 8. From this figure, it is observed that the initial antenna does not satisfy the impedance

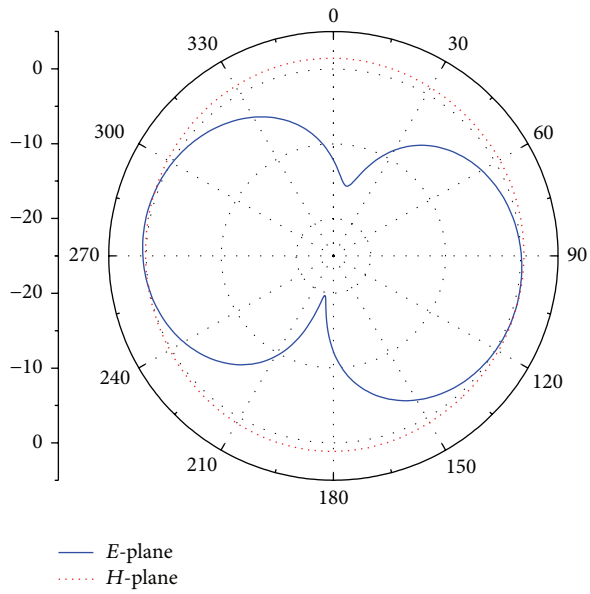

Figure 6: Simulated radiation pattern of single metamaterial antenna at center frequency of 2.44 GHz.

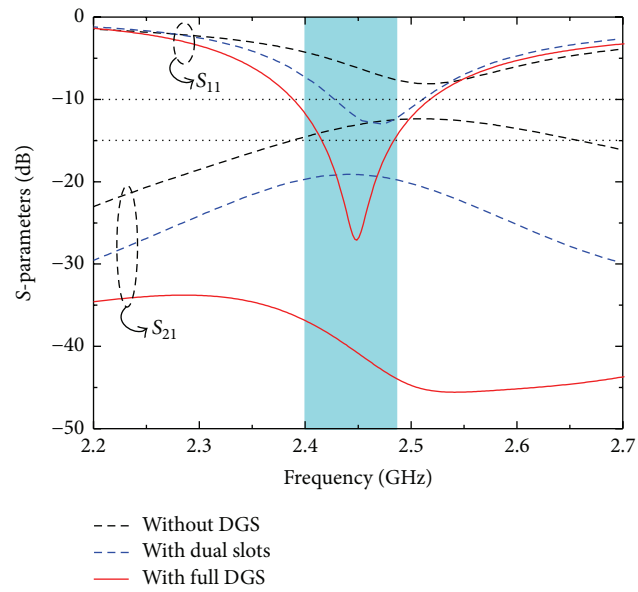

Figure 8: Simulated S-parameters in three cases: without DGS, with dual slots, and with full DGS.

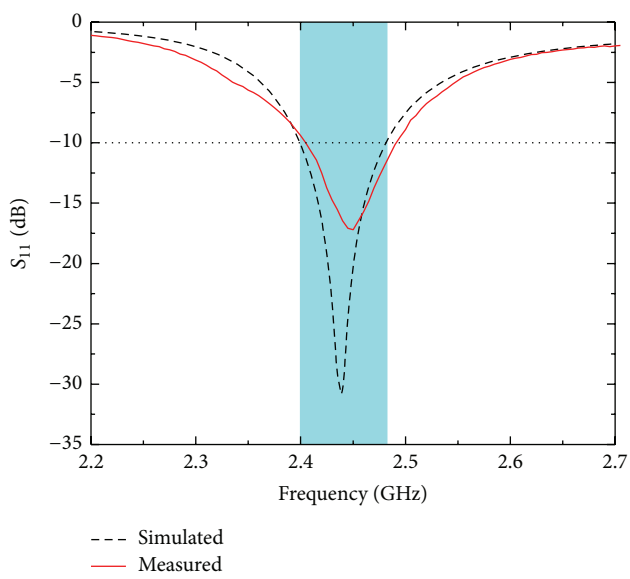

Figure 7: Simulated and measured results of single metamaterial antenna.

matching condition due to the effect of mutual coupling. The S-parameters of antenna are changed and could not meet the requirements of MIMO antenna from which S_{11} and S_{22} are not below −10 dB and S_{21} and S_{12} are not below −15 dB in WLAN band. This fact is clearly demonstrated by the surface current distribution on the initial MIMO antenna in Figure 10(a). As can be observed from Figure 10(a), when the first element (Port 1) is excited, the surface current is strongly induced on the second element (Port 2) resulting in a rise of the mutual coupling (S_{21} and S_{12}). Actually, the mutual coupling can be reduced by increasing the distance between the elements. However, this will lead to the larger size of the proposed MIMO antenna. These drawbacks of the initial MIMO antenna can be solved thanks to the use of defected ground structure etched on the common ground of MIMO antenna by the following two steps.

At first, two parallel slots are added to central ground plane between two ports (as shown in Figure 2(b)). The length slot L_3 is varied to find out the value from which the impedance matching and mutual coupling have the best solution. The optimized length of L_3 is chosen as 12 mm. Simulated S-parameters of MIMO antenna with dual slots are shown in Figure 8. From this figure, it can be seen that the isolation coefficient S_{21} is lower than −18 dB for all frequency in WLAN band. However, the impedance is not matched enough in this band so that the S_{11} is below −10 dB over the frequency ranging from 2.42 GHz to 2.5 GHz, and therefore the antenna could not cover the WLAN frequencies.

The current distribution of MIMO antenna with the implementation of dual slots at 2.44 GHz is shown in Figure 10(b). It can be seen from Figure 10(b) that the surface current partly focuses on the slots and somewhat coupling to the radiation strips of the adjacent antenna element.

In order to solve this problem, in the second step, two I-shaped slots are etched on the ground plane and used as an impedance matching circuit. The effect of I-shaped slots to impedance matching of the MIMO antenna is investigated via the length L. Figure 9 shows the simulated S-parameters of the MIMO antenna for the different values of L. It can be observed that the isolation coefficient is below −15 dB for all cases and the return loss is changed with the various sizes of slots. When the length L of I-slots increases, the input impedance decreases make the impedance highly matched. The final MIMO antenna with full DGS is formed as the value of L fixed at 5 mm. As a result, the full DGS MIMO

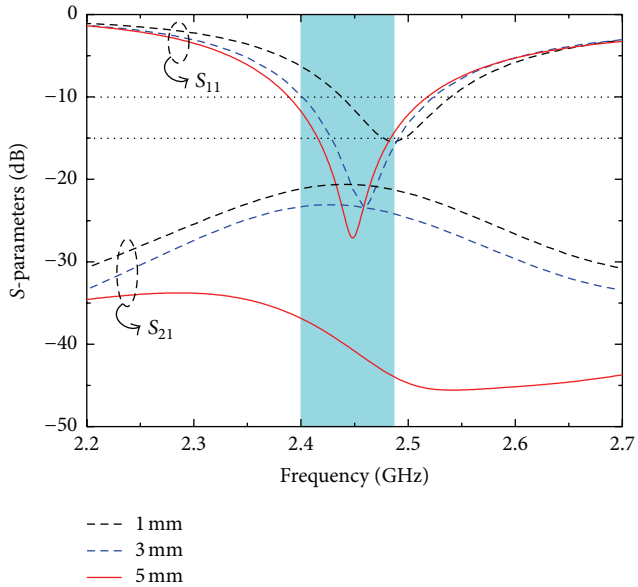

Figure 9: Simulated S-parameters of full DGS MIMO antenna for different values of L.

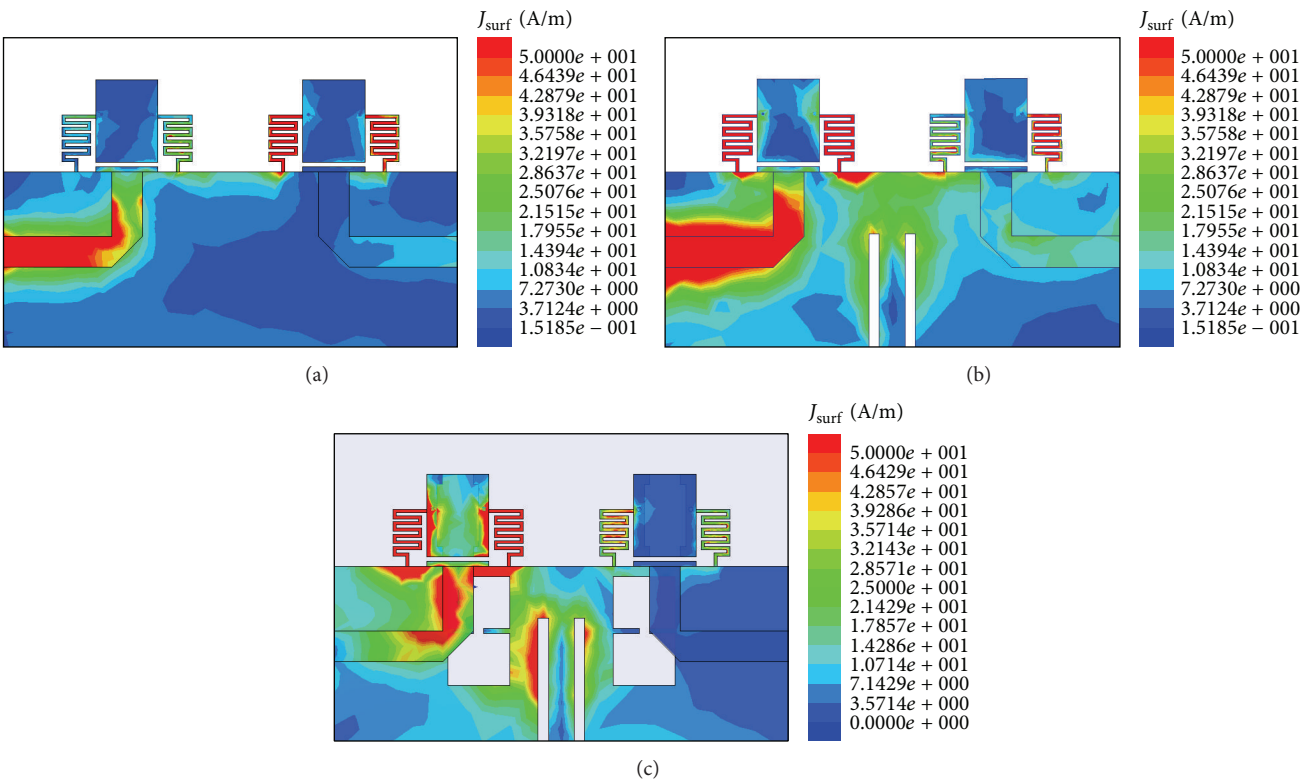

Figure 10: Surface current distribution at 2.44 GHz on metamaterial MIMO antenna (a) without DGS and (b) with the implementation of dual slots and (c) with full DGS.

antenna achieves high isolation coefficient which is less than −35 dB over all frequency of WLAN band while the operating bandwidth covers from 2.38 GHz to 2.52 GHz. The current distribution of the final MIMO antenna at 2.44 GHz is focused on the defected ground structure shown in Figure 10(c). Therefore, the effect of the surface current to the second element is significant reduced.

Simulated radiation patterns of final MIMO antenna in the xy, yz, and xz planes at 2.44 GHz when the antenna is fed; each port in turn is shown in Figure 11. The antenna displays

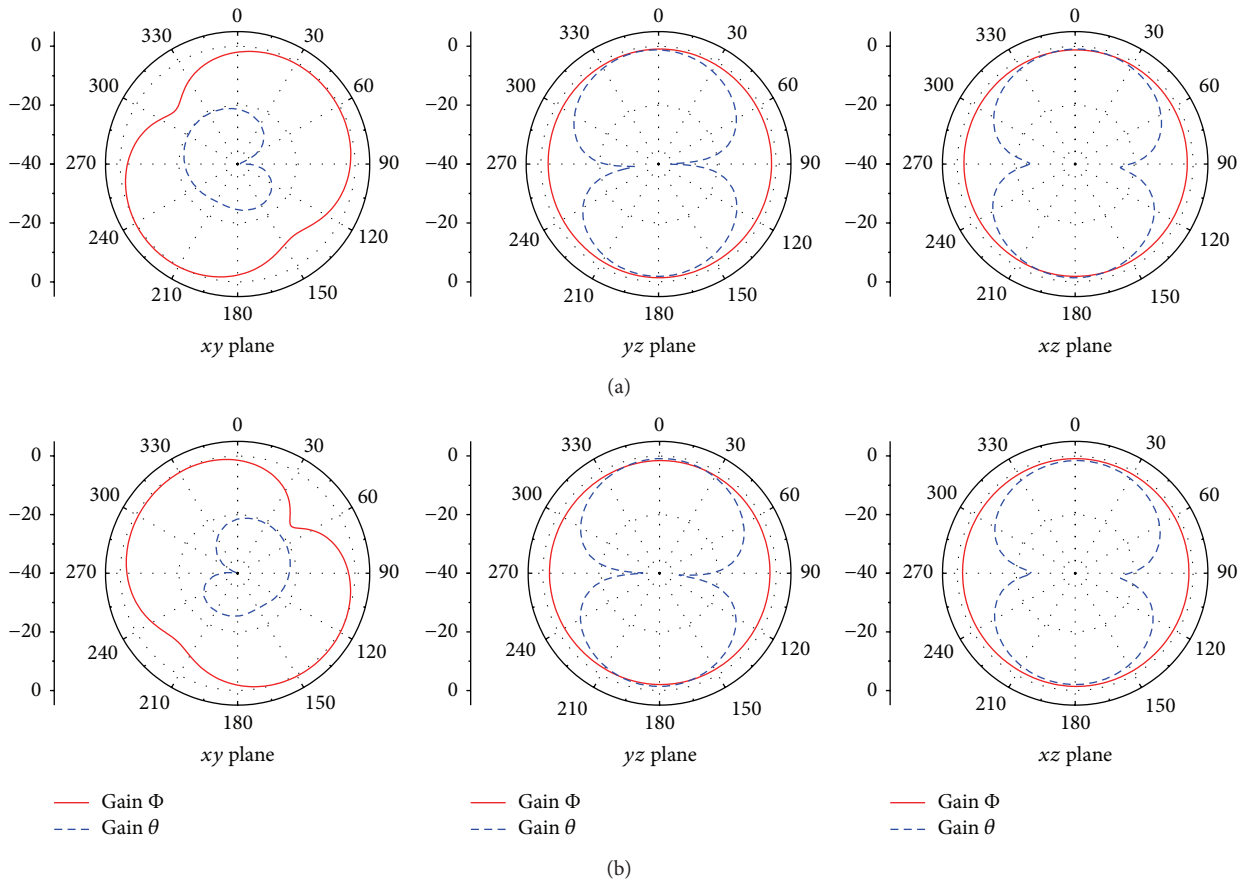

Figure 11: Radiation patterns of proposed metamaterial MIMO antenna at central frequency of 2.44 GHz when (a) excited Port 1 and (b) excited Port 2.

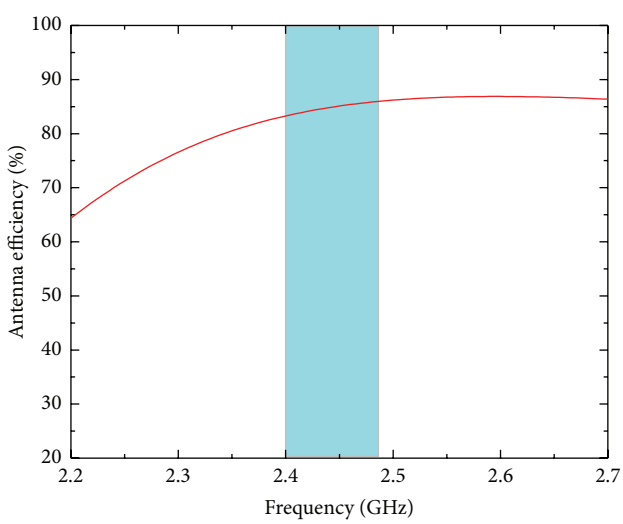

Figure 12: Simulated radiation efficiency of proposed antenna.

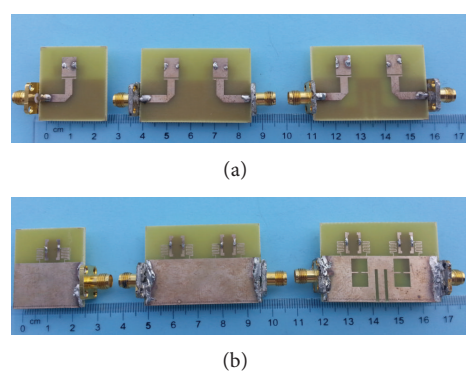

Figure 13: Fabrication of the single metamaterial antenna; initial and final MIMO antenna (a) front view and (b) back view.

good omnidirectional radiation patterns in the yz and xz planes (H-plane) while the separate far field patterns are produced in the xy plane (E-plane). Therefore, the diversity for the antenna is achieved. Thanks to this characteristic, the antenna is a promising candidate for MIMO system.

Figure 12 gives the simulated radiation efficiency of the proposed antenna. This figure indicates that the proposed antenna shows good radiation efficiency, which has the average value of 85% in over the operating bandwidth of WLAN system.

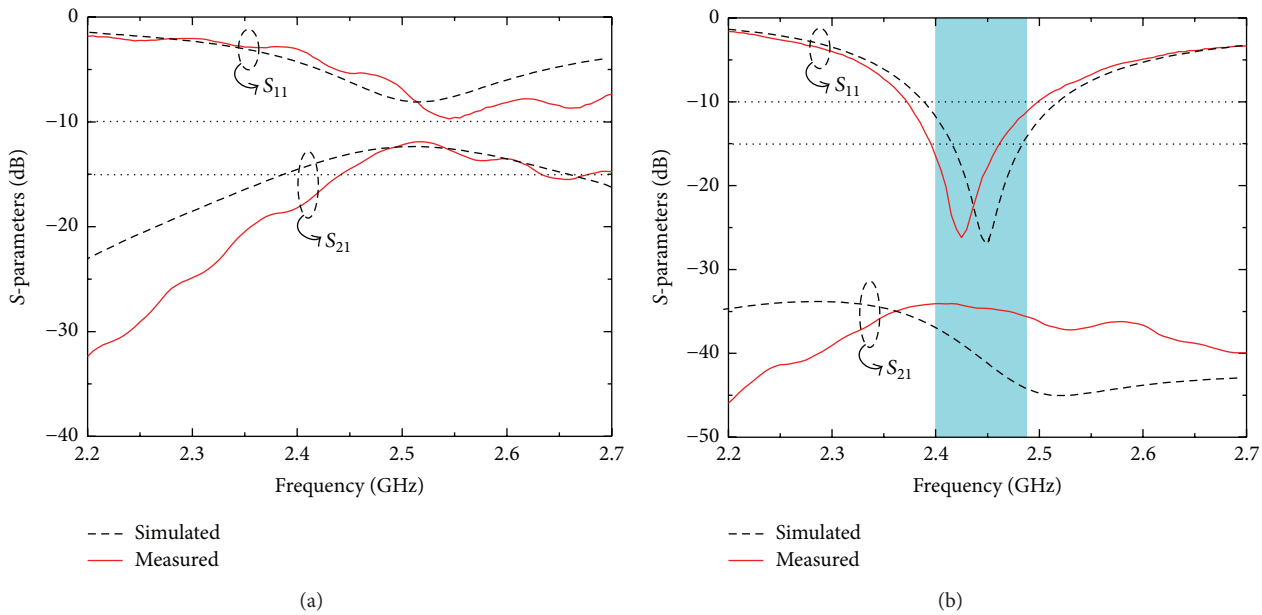

Figure 14: Simulated and measured S-parameters of (a) initial MIMO antenna and (b) final MIMO antenna.

Figure 14 presents the measured S_{11} and S_{21} of the fabricated initial and final MIMO antenna shown in Figure 13. From this figure, it is observed that the final MIMO antenna can operate over the range spreading from 2.38 to 2.5 GHz which is covering the WLAN band. Meanwhile, the mutual coupling between two elements (S_{21}) is less than −35 dB over WLAN range. It should be noted that the measured results are in good agreement with the simulated results.

3.3. MIMO Characteristics. MIMO antennas are required to be characterized for their diversity performance. In each system, the signals can be usually correlated by the distance between the antenna elements [16]. The parameter used to assess the correlation between radiation patterns is so-called enveloped correlation coefficient (ECC). Normally, the value of ECC at a certain frequency is small in case of the radiation pattern of each single antenna differently from each other. Otherwise, the same patterns of these antennas will exhibit the larger value of enveloped correlation coefficient. The factor can be calculated from radiation patterns or scattering parameters. For a simple two-port network, assuming uniform multipath environment, the enveloped correlation (ρ_e), simply square of the correlation coefficient (ρ), can be calculated conveniently and quickly from S-parameters [17], as follows:

$$\rho_e = \frac{\left|S_{11}^* S_{12} + S_{21}^* S_{22}\right|^2}{\left(1 - \left|S_{11}\right|^2 - \left|S_{21}\right|^2\right)\left(1 - \left|S_{22}\right|^2 - \left|S_{12}\right|^2\right)}. \quad (2)$$

The calculated ECC of proposed antenna by using the simulated and measured S-parameters is shown in Figure 15. From this figure, the proposed MIMO antenna has the simulated ECC lower than 0.01, while the measured one has lower than 0.02 over the operating frequencies. Therefore, the proposed antenna is suitable for mobile communication with a minimum acceptable correlation coefficient of 0.5 [18].

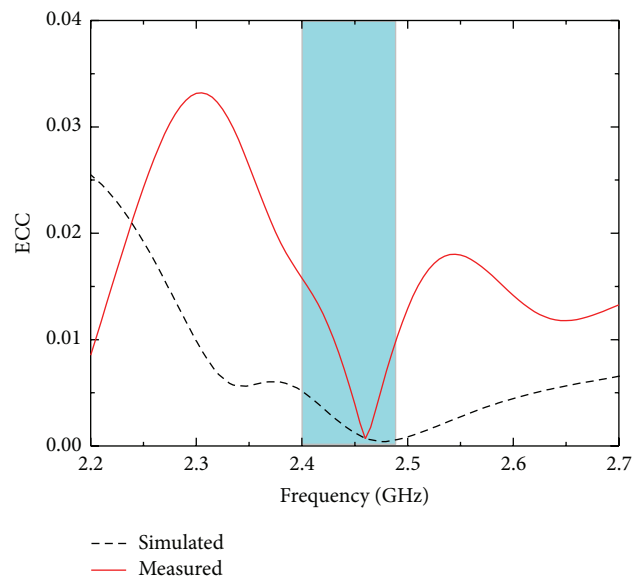

Figure 15: Simulated and measured proposed MIMO antenna's envelope correlation coefficient.

4. Conclusions

The compact 2 × 2 metamaterial MIMO antenna is designed to operate in WLAN frequency band. By using the modified CRLH model, the proposed metamaterial antenna achieves 60% size reduction in comparison with the unloaded antenna. The defected ground structures are inserted to

suppress the effect of surface current on the elements of the proposed antenna for reducing the mutual coupling. The antenna offers the compact size with the diversity radiation patterns. The fabricated MIMO antenna shows isolation less than −35 dB over its operating frequency band spreading from 2.38 to 2.5 GHz. The proposed MIMO antenna has also a minimum correlation coefficient which is less than 0.02 over the WLAN frequency range. Summing up the result, it can be concluded that the proposed antenna is a good candidate for WLAN applications.

Conflict of Interests

The authors declare that there is no conflict of interests regarding the publication of this paper.

References

[1] J. P. Gianvittorio and Y. Rahmat-Samii, "Fractal antennas: a novel antenna miniaturization technique, and applications," *IEEE Antennas and Propagation Magazine*, vol. 44, no. 1, pp. 20–36, 2002.

[2] G. Monti, L. Catarinucci, and L. Tarricone, "Compact microstrip antenna for RFID applications," *Progress in Electromagnetics Research Letters*, vol. 8, pp. 191–199, 2009.

[3] W. J. Krzysztofik, "Modified Sierpinski fractal monopole for ISM-bands handset applications," *IEEE Transactions on Antennas and Propagation*, vol. 57, no. 3, pp. 606–615, 2009.

[4] A. Mehdipour, I. D. Rosca, A.-R. Sebak, C. W. Trueman, and S. V. Hoa, "Full-composite fractal antenna using carbon nanotubes for multiband wireless applications," *IEEE Antennas and Wireless Propagation Letters*, vol. 9, pp. 891–894, 2010.

[5] M. N. Jahromi, A. Falahati, and R. M. Edwards, "Bandwidth and impedance-matching enhancement of fractal monopole antennas using compact grounded coplanar waveguide," *IEEE Transactions on Antennas and Propagation*, vol. 59, no. 7, pp. 2480–2487, 2011.

[6] A. Arazi, "Ultra wideband fractal microstrip antenna design," *Progress in Electromagnetic Research C*, vol. 2, pp. 7–12, 2008.

[7] G. V. Eleftheriades, A. K. Iyer, and P. C. Kremer, "Planar negative refractive index media using periodically L-C loaded transmission lines," *IEEE Transactions on Microwave Theory and Techniques*, vol. 50, no. 12, pp. 2702–2712, 2002.

[8] G. V. Eleftheriades, "Enabling RF/microwave devices using negative-refractive-index transmission-line (NRI-TL) metamaterials," *IEEE Antennas and Propagation Magazine*, vol. 49, no. 2, pp. 34–51, 2007.

[9] G. V. Eleftheriades, A. Grbic, and M. Antoniades, "Negative-refractive-index transmission-line metamaterials and enabling electromagnetic applications," in *Proceedings of the IEEE Antennas and Propagation Society Symposium*, vol. 2, pp. 1399–1402, IEEE, June 2004.

[10] A. Sanada, M. Kimura, I. Awai, C. Caloz, and T. Itoh, "A planar zeroth-order resonator antenna using a left-handed transmission line," in *Proceedings of the 34th European Microwave Conference*, pp. 1341–1344, October 2004.

[11] M. A. Antoniades and G. V. Eleftheriades, "A folded-monopole model for electrically small NRI-TL metamaterial antennas," *IEEE Antennas and Wireless Propagation Letters*, vol. 7, pp. 425–428, 2008.

[12] A. Lai, K. M. K. H. Leong, and T. Itoh, "Infinite wavelength resonant antennas with monopolar radiation pattern based on periodic structures," *IEEE Transactions on Antennas and Propagation*, vol. 55, no. 3, pp. 868–876, 2007.

[13] J.-G. Lee and J.-H. Lee, "Zeroth order resonance loop antenna," *IEEE Transactions on Antennas and Propagation*, vol. 55, no. 3, pp. 994–997, 2007.

[14] J. Zhu and G. V. Eleftheriades, "Dual-band metamaterial-inspired small monopole antenna for WiFi applications," *Electronics Letters*, vol. 45, no. 22, pp. 1104–1106, 2009.

[15] J. Zhu and G. V. Eleftheriades, "A compact transmission-line metamaterial antenna with extended bandwidth," *IEEE Antennas and Wireless Propagation Letters*, vol. 8, pp. 295–298, 2009.

[16] A. Najam, Y. Duroc, and S. Tedjni, "UWB-MIMO antenna with novel stub structure," *Progress in Electromagnetics Research C*, vol. 19, pp. 245–257, 2011.

[17] J. Thaysen and K. B. Jakobsen, "Envelope correlation in (N, N) mimo antenna array from scattering parameters," *Microwave and Optical Technology Letters*, vol. 48, no. 5, pp. 832–834, 2006.

[18] M. P. Karaboikis, V. C. Papamichael, G. F. Tsachtsiris, C. F. Soras, and V. T. Makios, "Integrating compact printed antennas onto small diversity/MIMO terminals," *IEEE Transactions on Antennas and Propagation*, vol. 56, no. 7, pp. 2067–2078, 2008.

Hindawi Publishing Corporation
International Journal of Antennas and Propagation
Volume 2015, Article ID 278160, 9 pages
http://dx.doi.org/10.1155/2015/278160

Research Article

Linear Array Design with Switched Beams for Wireless Communications Systems

Vinícius Ludwig-Barbosa,[1] Edson Schlosser,[2] Renato Machado,[1,3] Filipe Guterres Ferreira,[2] Sabrina Müller Tolfo,[2] and Marcos Vinício Thomas Heckler[2]

[1] *Universidade Federal de Santa Maria, 97105-900 Santa Maria, RS, Brazil*
[2] *Universidade Federal do Pampa, 97546-550 Alegrete, RS, Brazil*
[3] *Blekinge Institute of Technology, 371 79 Karlskrona, Sweden*

Correspondence should be addressed to Vinícius Ludwig-Barbosa; viniciuslbar@mail.ufsm.br

Received 19 September 2014; Revised 30 March 2015; Accepted 3 April 2015

Academic Editor: Wenhua Chen

This paper presents an analysis for optimal design of switched beamforming applied to a linear array for wireless communication systems. The beam switching scheme provides coverage of a given sector in azimuth and controls the sidelobe level simultaneously. The analysis was developed considering arrays composed of Quasi-Yagi elements. The model assumes a user moving in the azimuthal direction under a constant velocity and with an estimation of the signal-to-noise ratio (SNR) at the mobile user (MU). The radio base station applies the beam that yields the best performance during transmission. The decision is based on the feedback information received from the MU. The goal of the analysis is to determine the best trade-off between the array size and number of feedback bits necessary to maximize the SNR at the receiver. The results show that a compromise between the number of beam-pointing directions and the array size should be taken into consideration for a wireless communication system design.

1. Introduction

The evolution of wireless communication systems is notorious. The amount of services available to mobile users is enormous and the quality of service should be great in the same proportion. During the last decades, different techniques were proposed aiming at improving the system performance and its capabilities of providing services to a greater number of subscribers. The cellular system, for example, has evolved through many generations to improve the quality of service (QoS), data rate, system reliability, and robustness [1].

Antennas and arrays have played an important role along this evolution. Several designs and techniques were applied to wireless communications in order to improve the system performance, such as MIMO systems combined with antenna array and smart antenna concepts [2–4].

As a simpler alternative to smart antennas, an array with switched beams is an interesting technique to be explored. This approach relies on the use of predefined beam-pointing directions that can be set at any time as it is required. The lower level of complexity compared to adaptive beamforming is an important advantage of this technique. It is based on a quantized version of space, in contrast to the continuous space that is covered by fully smart antennas.

In addition, the radiation pattern of the antenna array is an important aspect due to the necessity of suppressing the radiated power towards unwanted directions. In order to deal with this challenge, some methods of pattern synthesis are used to provide the excitation current of each antenna that composes the array. Fourier Transform, Woodward-Lawson, and Dolph-Chebyshev could be mentioned as the most common methods applied to fit the desired radiation pattern and control sidelobe level (SLL) [5, 6]. However, these techniques generally do not take mutual coupling into account. This can be a limitation for accurate beamforming.

In this paper, the study of arrays with switched beams is investigated. The beams have been synthesized by an

approach that combines genetic algorithm (GA) and sequential quadratic programming (SQP). This approach includes mutual coupling between the array elements in the synthesis process. These two techniques have been chosen for the present work because they combine both global and local optimization algorithms and they have been used successfully for other beam shaping problems [2]. The analysis presented in this paper provides a better insight on how to design linear array with switched beams, seeking for an optimal compromise between the number of antennas and beams for the antenna array at the radio base station (RBS) aiming at maximizing the signal-to-noise ratio (SNR) at the receiver. This analysis is important to improve the performance of a wireless communication system, as investigated in [7–9].

The analysis is applied on an array of Quasi-Yagi elements, which are composed basically of a fed structure (driver) and directors (parasitics). Parasitic antennas have large application combined with beam switching technique [10–12]. In all these cases, different radiation patterns are produced by commuting PIN diodes and modifying the electrical length of the parasitic elements. The advantages and feasibility of Quasi-Yagi elements applied on antennas arrays are highlighted in [13–15]. In [14], Cai et al. present a two-element array producing only one beam while [15] presents an array of 4 elements and 4 different radiation patterns in distinguished directions. In both cases, the patterns are not optimized concerning sidelobe levels. In addition, the array presented in [15] is implemented with microstrip delay lines to produce the appropriated phase shifts. Either in [15] or in PIN diode-based applications, the beam-switched arrays have their beam steering capacity limited by their structure. In this context, we present an analysis for optimal design of Quasi-Yagi beam-switched linear array, digitally controlled, to yield a coverage of a given azimuth sector. Further, it must reach the best SNR by taking into account the trade-off between array size and feedback quantization. Since the array is digitally controlled, the number of beam-steering and directions are easily adapted for different scenarios. This characteristic makes the array more flexible and less dependent on its layout structure as for the case of integrating shift delay lines and embedded components into the array structure.

The paper is organized as follows. Section 2 presents the system model considered in this analysis. In Section 3, the main characteristics of Quasi-Yagi antennas are presented along with the model specifications applied in this paper. The theoretical background on optimization algorithms for array synthesis is addressed in Section 4. In Section 5, the array with switched beam for wireless communications system applications is presented. Section 6 presents the simulation results, which are used to evaluate different sets of switched beams. Finally, Section 7 presents the conclusions and some final remarks.

2. System Model

The system model considered in this paper is composed of a RBS, where a linear antenna array is installed on, and a mobile user (MU), which is moving in the azimuthal direction

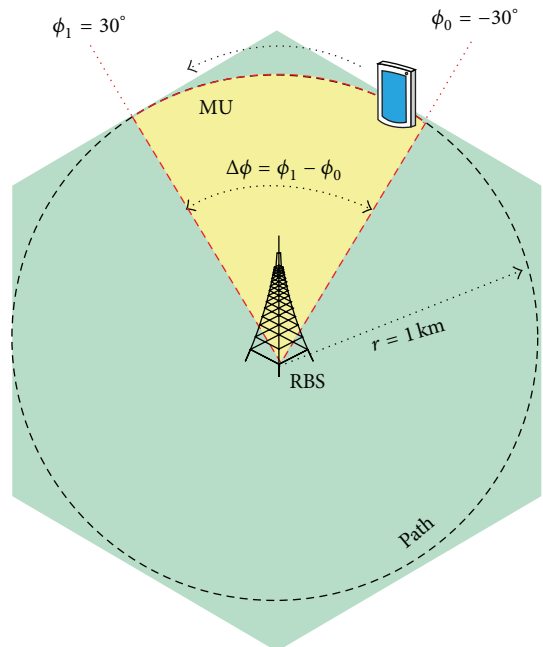

Figure 1: Mobile user scenario. The user moves with a uniform speed with constant radial distance from the RBS.

assuming a constant radial distance from the radio station, as shown in Figure 1. This scenario was chosen to simplify the analysis, reducing the amount of variables involved in the problem, and to emphasize the movement of the MU toward the azimuthal direction. This enforces the system to switch between the available beams as long as it is required.

In the next subsections, the mathematical formulation used to model the signal properties and the relation between the transmitted and received signals is described.

2.1. Mobile User. The mobile terminal is assumed to be a user walking with a uniform speed of 6 km/h. The radial distance between MU and RBS is constant and equals 1 km, as depicted in Figure 1. The transmitting antenna array is considered to be sectorized [16] and its coverage is within −30 and 30 degrees. The MU model considered in this paper is the well-known uniform circular motion (UCM) [17], which suits the characteristics of the scenario under analysis. The equations are presented as follows:

$$v = \omega r, \tag{1}$$

where v is the linear speed and

$$\omega = \frac{\Delta\phi}{t} \tag{2}$$

is the angular velocity. The term $\Delta\phi$ is given in radians and is defined by

$$\Delta\phi = \phi_1 - \phi_0 = \frac{\Delta s}{r}, \tag{3}$$

where ϕ_1 and ϕ_0 are the limits of the coverage area, Δs is the walking distance, and r is the radial distance between RBS and MU.

2.2. Path Loss Model. The power received by the MU is calculated by using the free-space loss model (Friis equation) combined with the log-distance path loss model [18, 19]. Friis equation estimates fading between the RBS and the user and consequently the received power at the mobile terminal. The log-distance path loss model adds the urbanization effects to the losses. The free-space loss model is given by

$$P_L = 10\log\frac{P_r}{P_t} = 10\log\left[\mathrm{PLF}\frac{G_t(\theta_t,\phi_t)\,G_r(\theta_r,\phi_r)\,\lambda^2}{(4\pi)^2 r^2}\right], \quad (4)$$

where PLF is the polarization loss factor, P_L is the total loss between RBS and MU (in dB), P_t is the transmitted power (in Watts), P_r is the received power (in Watts), G_t and G_r stand for the realized gains of the transmit (RBS) and receive (MU) antennas, respectively, and λ is the carrier wavelength in free space. The term r is the straight distance between the RBS and MU. The gains G_t and G_r take into account the reflection coefficient at the inputs of each antenna [20].

The losses caused by the urbanization effects can be computed by

$$L_{\mathrm{dB}}(d) = L(d_o) + 10n\log\left(\frac{r}{r_o}\right), \quad (5)$$

where r_o is a reference distance and n is the loss exponent. In this paper, we consider $r_o = 100$ m as a reference distance and $n = 4$, considering urban building effects.

Finally, the received power is given by

$$P_r\,(\mathrm{dBm}) = P_t\,(\mathrm{dBm}) - P_L\,(\mathrm{dB}) - L_{\mathrm{dB}}(d). \quad (6)$$

In this system model, it is assumed that the received signal at the MU is contaminated with a Gaussian noise with zero mean and variance N_0. Therefore, the SNR (dB) at the receiver is defined as

$$\mathrm{SNR}\,(\mathrm{dB}) = P_r\,(\mathrm{dBm}) - N_0\,(\mathrm{dBm}). \quad (7)$$

3. Quasi-Yagi Antennas

The Quasi-Yagi antenna gathers good features of printed and Yagi-Uda antennas. It has a low-profile structure, which allows installing it easily on the RBS or integrating it into an antenna array. In addition, the Quasi-Yagi antennas can be built using only one laminate, so that it can be considered a cost-effective solution for mass production.

A Quasi-Yagi antenna has been designed to operate with broadband centered at 2.4 GHz. The antenna has been built using an FR4 laminate with the following characteristics: dielectric constant $\varepsilon_r = 4.1$, loss tangent $\tan\delta = 0.02$, and laminate thickness $h = 1.58$ mm. Figure 2 presents the antenna prototype, which is composed of one active dipole and one director. The balun is implemented in microstrip technology and is used to provide a 180-degree phase shift between the two terminals of the active dipole. The antenna dimensions are listed in Table 1.

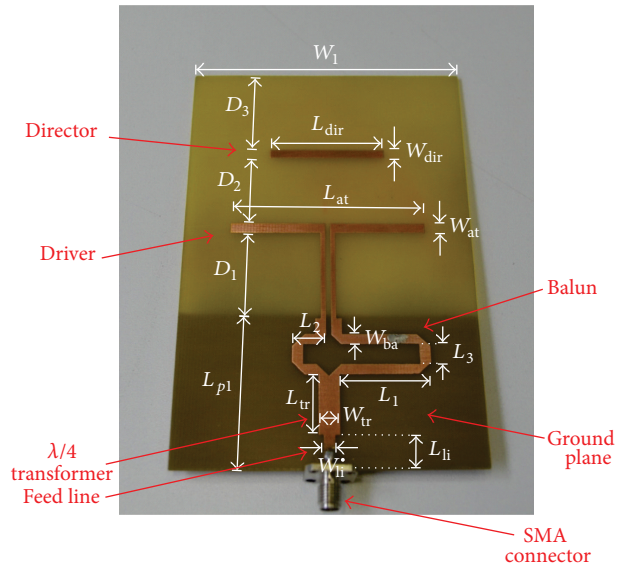

Figure 2: The prototype of the Quasi-Yagi antenna designed and used in this work.

Table 1: Parameters dimensions of the Quasi-Yagi antenna.

Parameter	Dimension (mm)
L_{li}, W_{li}	8.74, 2.86
L_{tr}, W_{tr}	16, 5.4
L_1	23.96
L_2	6.9
L_3	5.4
W_{ba}	2.86
L_{p1}, W_1	41.22, 80
D_1	24.5
D_2	20
L_{at}, W_{at}	54, 3
L_{dir}, W_{dir}	33.15, 3
L_{sub}	120

Figure 3 shows a comparison between simulated and measured curves for the reflection coefficient at the antenna input. One can see that good matching is achieved in the frequency range of 1.93–2.76 GHz considering the criterion of reflection coefficient lower than −10 dB. The reflection coefficient at 2.4 GHz satisfies this criterion for both the simulated and measured curves.

Figures 4 and 5 show calculated radiation patterns in the H- (azimuth) and E-planes (elevation). The gain at 2.4 GHz is 5.24 dBi, which is a good value considering that the antenna has been built on an FR4 laminate. An analysis of the variation of gain inside the band 1.93–2.76 GHz showed that the maximum gain achieved is 6.0 dBi at 2.76 GHz. The gain decreases for lower frequencies. The criterion assumed to determine the gain bandwidth was to consider a maximum variation of 3 dB related to the gain at 2.76 GHz, which is verified to occur at 2.01 GHz. Therefore, taking into consideration both criteria for reflection coefficient and gain variations

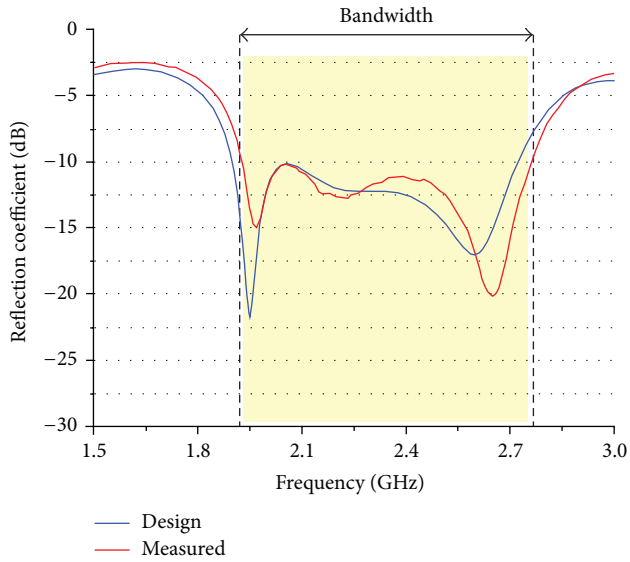

Figure 3: Comparison between simulated and measured results for the reflection coefficient at the antenna input.

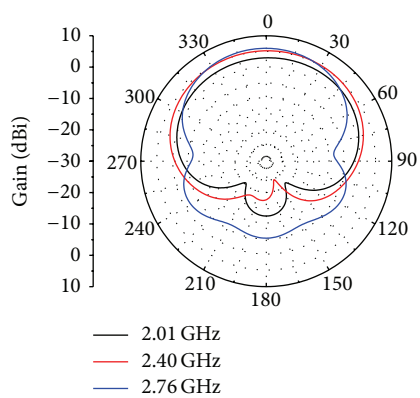

Figure 4: Radiation pattern in the H-plane (azimuth).

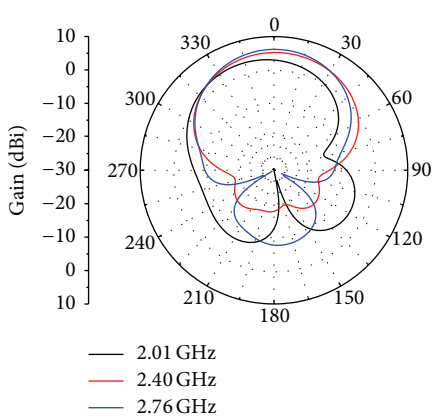

Figure 5: Radiation pattern in the E-plane (elevation).

over the frequency, the antenna operating bandwidth is 2.01–2.76 GHz.

4. Array Synthesis

Algorithms of pattern synthesis are powerful tools to control radiation pattern of an antenna array. These tools calculate the magnitudes and phases that should be applied to each array element in a way that parameters like half-power beamwidth, direction of the main beam, and sidelobe levels reach constraint values. There are some traditional algorithms, such as the Fourier Transform technique that do not produce satisfactory results when complex patterns are specified, unless a large number of elements are considered. Depending on the design needs, this may be a disadvantage, since the larger the array is, the more complex its construction is. The well-known Dolph-Chebyshev technique has good performance for SLL control, but it is limited to arrays composed of isotropic elements.

The complex coefficients for the antenna arrays considered in this paper are calculated by using two combined optimization methods: the genetic algorithm (GA) [21, 22] and the sequential quadratic programming (SQP) [23]. The GA is a method based on the evolution of an initial population that is generated randomly and is used to generate new populations. In the GA, the new individuals are expected to be closer and closer to the optimum solution for the optimization problem, until all the requirements are fulfilled. In the current implementation of GA, each individual is treated as a vector with its components standing for the magnitudes and phases of the currents that should be impressed at the array elements, as given by

$$\mathbf{I_j} = \left[\left|I_1\right| \ \angle\delta_1 \cdots \left|I_i\right| \ \angle\delta_i \cdots \left|I_N\right| \ \angle\delta_N\right], \tag{8}$$

where $\mathbf{I_j}$ stands for the jth individual in a population and $|I_i|$ and $\angle\delta_i$, $i = 1 \cdots N$, are the magnitude and phase of the current to be impressed at the ith array element, respectively. By looking at (8), each individual is composed of $2N$ genes and represents a set of excitation currents that produce the radiation pattern $\vec{E}_{\text{array}}(\phi)$. This pattern is a candidate solution for the synthesis problem.

In order to assess whether the pattern $\vec{E}_{\text{array}}(\phi)$ fulfills the imposed requirements, every individual is assigned with a fitness value based on the error function, which is calculated by [2]

$$g(\phi) = F(\phi) - \left|\vec{E}_{\text{array}}(\phi)\right|, \quad \phi \in [0^\circ, 180^\circ], \tag{9}$$

where $g(\phi)$ is the error between the specified pattern $F(\phi)$ and the calculated pattern $\vec{E}_{\text{array}}(\phi)$. The term $\phi \in [0^\circ, 180^\circ]$ is the angular interval in the azimuth plane in which the synthesis is done. A measure on how close the pattern corresponding to a given individual is to the specified pattern is achieved by the definition of a fitness value, which is calculated by

$$\text{fitness} = \frac{1}{L}\sum_{i=1}^{L}\left|g(\phi_i)\right|^2, \tag{10}$$

where L is the number of samples within the angular region under optimization. For every population, the fitness is calculated for every individual. The process of evolution runs until a predefined maximum number of generations are reached or until the specification for the fitness value is satisfied.

New populations are generated by selecting the individuals that present the best fitness values, by crossings of the individuals of a previous generation and by means of mutation. This last operation is important to avoid that GA converges to local minima. These are standard operations of the classical GA algorithm. Detailed information about them can be found in [21].

For the synthesis of a shaped pattern, the GA could be run until all the specifications are fulfilled. However, depending on how hard the specifications are, it may take several iterations and long computing time for the method to converge. In order to accelerate the synthesis process, the proposed approach considers running GA only for a predefined number of iterations (evolutions), so as to obtain an initial estimation of the coefficients. Even without any estimate for the currents to initialize the synthesis, this strategy is successful because GA is a global-search algorithm.

After the maximum number of generations is reached, the individual with the lowest fitness value is selected and used to start the SQP. Finally, SQP is run as a local-search approach until a set of coefficients that synthesize the pattern according to a specified mask pattern is obtained.

In contrast to other more complex shaped patterns, whereby the synthesized pattern is fixed and must follow a specified contour, the most important requirements for arrays with switched beams are only the direction of the main beam ϕ_m and the maximum allowed sidelobe level SLL. Such a mask is illustrated in Figure 6, which is the graphical representation of $F(\phi)$ in (9). The rectangles describe the region of the sidelobes and the arrow is used to represent the direction of the main beam. The regions between the main beam and the sidelobes are left without restrictions.

The Quasi-Yagi antenna has been used to compose arrays with 2, 4, and 8 elements. The geometry of the model simulated in HFSS for the case of 8 antennas is shown in Figure 7, where the spacing between adjacent elements is uniform and equals $d = 0.5\lambda$. This value is a design trade-off, since mutual coupling increases as d is made smaller, whilst the level of the sidelobes becomes larger and more difficult to control if d is made larger than 0.5λ.

Since the simulator is based on the finite element technique, the mutual coupling between the antennas is taken into account. In order to allow the synthesis, the individual antenna patterns are calculated and exported from HFSS. This is done by exciting only one antenna at a time and by setting the excitation at the other ports to 0. This is done for every antenna that composes the array. Finally, the radiation pattern of the array $\vec{E}_{\text{array}}(\phi)$ is calculated by the weighted vector sum of the individual patterns, whereby the weights are the complex excitation coefficients (currents) calculated by the synthesis algorithm.

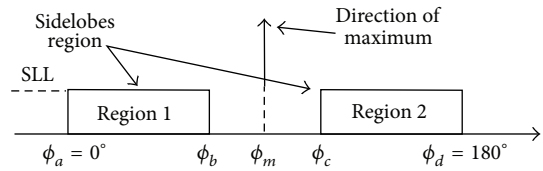

Figure 6: Mask applied for the synthesis of the switched beam arrays.

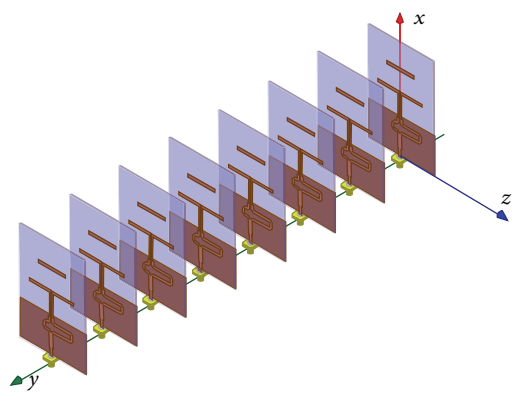

Figure 7: Simulated model of the array composed of 8 elements placed along the y-axis.

5. Beamforming Setup

In an ideal system, the transmitter at RBS should be able to follow the mobile user all the time in any direction inside the cell. However, in a real-world scenario, there is a feedback channel in between the MU and RBS, which can send only a few bits of feedback to the transmitter. It means that the feedback channel is quantized and, consequently, there must be a compromise between the array design, which includes the number of beam-pointing directions, and the SNR requirement.

The number of beams will depend on the amount of bits transmitted on the feedback channel and is governed by the constraints of the system. For example, if the feedback channel supports n bits, then the transmitter should be able to produce beams pointing to 2^n directions in the azimuthal plane.

Before each new transmission takes place, the RBS sends pilot bits with information on the available set of beams and the MU can estimate the SNR level that each pointing direction could yield. With this information, the receiver can evaluate which configuration is the most suitable and, therefore, could deliver the best performance during the current frame. Finally, the receiver feeds back the n bits containing the information (a label) correspondent to the beam-pointing direction (from a set of 2^n beam-pointing), which must be performed by the transmitter. This procedure is performed periodically and the RBS can upload the excitation coefficients (in the antenna array) for each new transmission frame, which makes the maximization of the SNR at the receiver possible.

The switching between the available beams occurs in the intersection point between adjacent beams. At this specific point, the minimum SNR value for the selected beam is reached. As a consequence, the QoS can decrease and only lower data rates become possible if the actual beam is kept during the transmission frame. Thus, at this moment, the switching to the adjacent beam occurs to provide higher gain in the direction of the MU. This approach guarantees that RBS applies the best beam-pointing to maximize the received SNR.

In the next section, simulation results are presented in order to evaluate the system performance for different array sizes and number of feedback bits. Based on the results, one can identify some trade-offs which should be kept in mind during the design of linear arrays with switched beams.

6. Simulation Results

This section presents some simulation results in order to assess the system performance for different array sizes and number of feedback bits. The SNR level is estimated based on the received power calculated using (6), which is sampled according to the speed of the user's motion. In this simulation, arrays of 2, 4, and 8 elements are considered. The beams for each array were synthesized using the mask depicted in Figure 6 by setting the values for ϕ_m so as to minimize the ripple and with SLL = 20 dB. The synthesis was run until the synthesized pattern fulfilled all the specifications given in Figure 6. The resulting sets of patterns are presented in Figure 10. For the simulations, the GA was set up for 40 individuals and for a maximal of 50 generations (iterations). The elapsed times for each case are the following: for the two-element array, 16 s; for the four-element array, 25 s; for the eight-element array, 37 s. The synthesis algorithm was run in MATLAB environment on computer with a core i7 processor with 3.4 GHz clock and 8 GB RAM.

The sets of patterns were tested for different design configurations, where the main motivation was to identify the best solution in terms of array size *versus* number of beam-pointing directions, where the latter is correlated with the number of feedbacks bits. For the simulations, the channel (user position) could be assumed to change randomly. However, it would not be a realistic assumption. Alternatively, a mathematical model can be used to simulate the user mobility within a cellular cell [24]. Therefore, in order to have a more realistic approach for the simulations, it is considered that a user moves at a constant velocity in the azimuthal direction, as illustrated in Figure 8. That is, there exists a constant angular velocity between receiver and transmitter. Thus, the system adaptivity is performed smoothly. The channel path loss model considered in the analysis is given by (6), which is described in more detail in Section 2.2. For all simulations, we assume that N_0 is −100 dBm (thermal noise) and the receiver has an omnidirectional antenna with G_r = 2 dBi.

The approach used to design the beam set (with 2^n steering inside the sector) provides approximately the same ripple variation between adjacent beams and between the sector boundaries, first/last beam and the coverage limits. This approach aims at increasing the QoS in the coverage area, thus keeping the SNR variation as low as possible [25]. The average ripple obtained for each system configuration is depicted in Table 2.

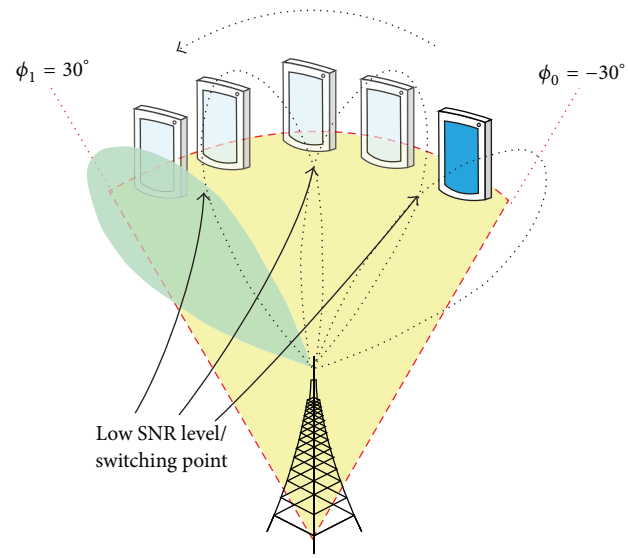

Figure 8: Array with switched beams on a RBS. The switching takes place in the intersection between adjacent beams.

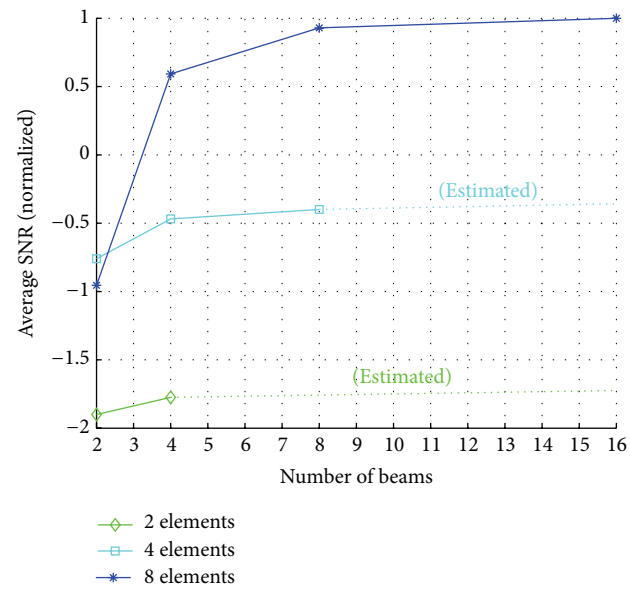

Figure 9: Average SNR as a function of the number of beam-pointing directions for different array sizes.

The ripple presented in Table 2 is basically dependent on the beamwidth. Arrays with few beams already yield low ripple due to broad beamwidth. This is clearly demonstrated by the two-element array. Larger arrays produce narrower beams. Consequently, more beam-pointing directions are required to reach low ripple levels. The worst-case ripple is around 15 dB, when an array of eight elements is combined with 2 beams. This configuration should be avoided since it is

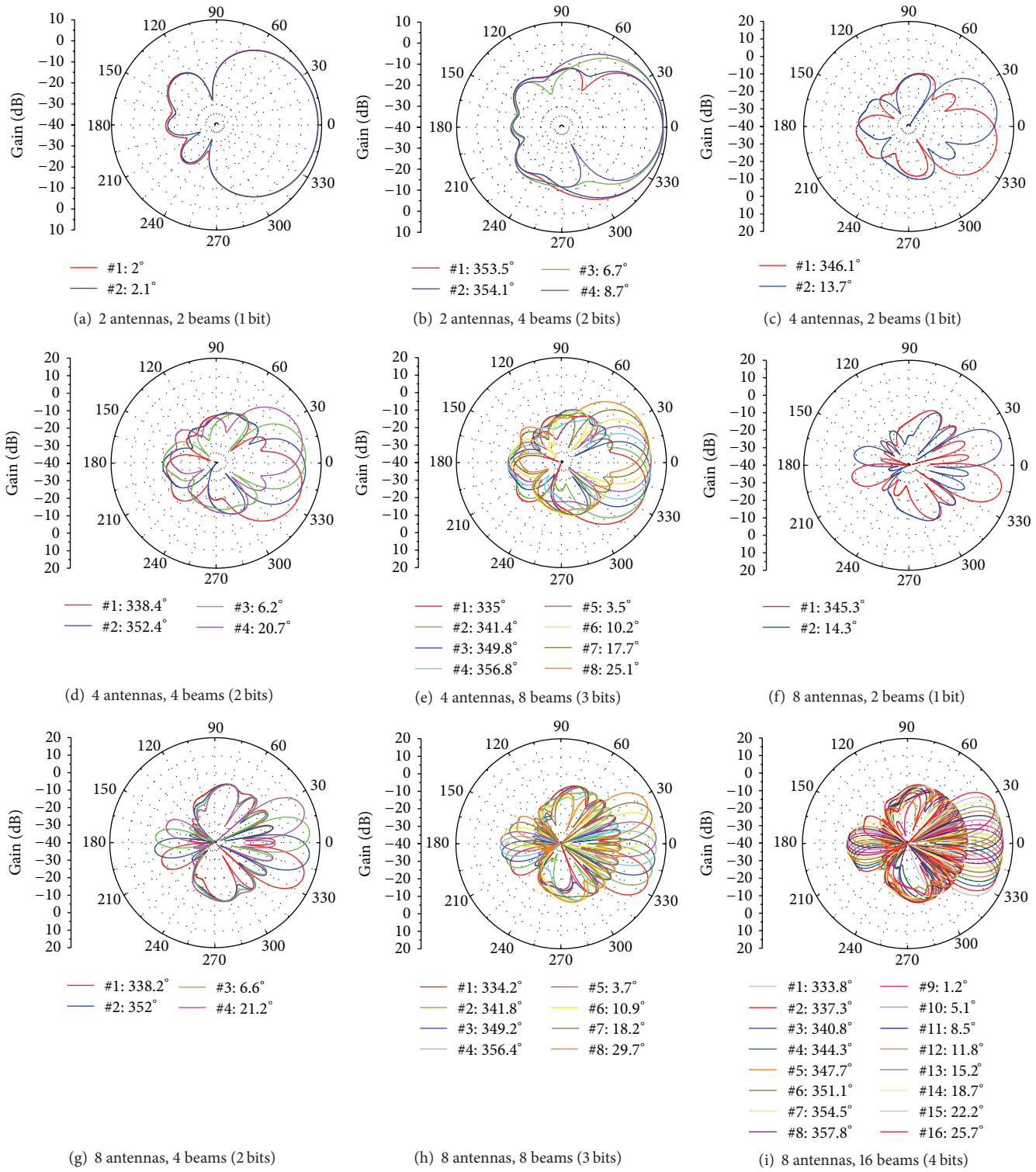

Figure 10: Gain patterns for the analyzed scenarios: linear arrays of 2, 4, and 8 elements. All patterns were synthesized with SLL = −20 dB below the main beam.

a combination of narrow beamwidth with a poor amount of beams.

From this point, it is possible to assess the system performance taking into account different configurations of array sizes × beam quantization levels. The power received at the MU was estimated according to the motion of the subscriber. This estimation was performed for each scenario under investigation.

Table 2: Average ripple between the maximum of lobe and the adjacent beam-pointing.

Array (elements, beams)	Ripple (dB)
(2, 2)	0.1
(2, 4)	0.1
(4, 2)	2.5
(4, 4)	0.7
(4, 8)	0.3
(8, 2)	15
(8, 4)	3
(8, 8)	0.8
(8, 16)	0.2

Figure 9 depicts the average normalized SNR for three array sizes, that is, arrays with 2, 4, and 8 elements. Considering the array with two elements (the green line with diamond dots), it is possible to realize that there is no gain (in a practical point of view) when the number of feedback bits (and the number of beam-pointing directions) is increased. For example, this system has 0.28 dB of gain when the number of feedback bits is increased from one to two. The relative gain (for $n+1$ compared to n bits) is even lower when the number of feedback bits is greater than 2. Based on those data and observing Figure 10, it is reasonable to discard this solution since the beamwidth of the two-element array is barely the same as that of the antenna designed (see Figure 4). As a result, using this array for beam switching applications is not advantageous.

When we compare the performance obtained by the array with four elements, it is notorious that the average SNR is higher than the one with two elements. For this case, one can see some advantage in exploring the feedback channel in order to improve the SNR level at the receiver. The SNR gain is approximately 0.65 dB from one over two feedback bits scenarios, which is already a significative result. Above this level of quantization ($n = 3$ or more), we can identify performance saturation.

Finally, the average SNR is improved in 5.22 dB when it is considered an array of eight elements with eight beam-pointing directions ($n = 3$ feedback bits). The increase in performance tends to become smaller and smaller when the number of feedback bits is greater than 3 (for this system configuration). As one can observe, the improvement made by the addition of feedback bits (or the number of beam-pointing directions) decreases as the number of feedback bits is increased (for all array sizes), giving an indication of performance saturation.

The differences among the analyzed arrays are mainly dependent on beamwidth and equivalent gain of each array. Larger arrays reach higher performances since the array equivalent gains are higher. However, the number of beams is more relevant since the ripple with few beams is greater, as observed in Table 2, and, basically, influenced by narrower beams. Therefore, an analysis such as the one presented in this paper is important and must be developed and evaluated to quantize the amount of beams in a given coverage area that guarantees maximization of SNR levels and, consequently, improvements in the system performance.

7. Conclusion

In this paper, a linear array design for wireless communication systems was proposed. The switched beamforming array scheme provides a coverage of a given angular area in the azimuthal plane and the sidelobe level is controlled simultaneously. The arrays evaluated in this paper are composed of two, four, and eight Quasi-Yagi elements. It was assumed that there is a user walking toward the azimuthal direction under a constant speed. The SNR at the receiver terminal remained as higher as possible according to the system configuration. The improvement made by the addition of feedback bits indicates performance saturation. The quantization of beam-pointing directions employed varies according to array size and should be taken into account for real-world systems in order to optimize the feedback channel usage. The analysis proves that an amount of beams equivalent to the number of elements (n elements and n beam-pointing directions) in a given array is a good trade-off in terms of array cost and SNR performance. An amount of beams bigger than the number of elements causes small improvements in the system performance, tending to saturation.

Conflict of Interests

This research does not have any competing interests concerning professional judgment, such as financial gain. All data shared on this paper has only academic interest and its reproduction is permitted unrestrictedly, since this original is properly cited.

Acknowledgments

This work was partially supported by the Coordination for the Improvement of Higher Education Personnel (CAPES/PROEX), Brazil, under Grant 1345 647, the National Council for Scientific and Technological Development (CNPq), Brazil, under Grants 211271-2013-6 and 306145/2013-8, the Swedish-Brazilian Research and Innovation Centre (CISB), and Saab AB.

References

[1] I. F. Akyildiz, D. M. Gutierrez-Estevez, and E. C. Reyes, "The evolution to 4G cellular systems: LTE-advanced," *Physical Communication*, vol. 3, no. 4, pp. 217–244, 2010.

[2] E. R. Schlosser, M. V. T. Heckler, C. Lucatel, M. Sperandio, and R. Machado, "Synthesis of linear antenna array for 4G mobile communication systems," in *Proceedings of the 15th SBMO/IEEE MTT-S International Microwave and Optoelectronics Conference (IMOC '13)*, pp. 1–5, August 2013.

[3] A. P. Gorbachev and V. M. Egorov, "A modified planar quasi-Yagi antenna for wireless communication applications," *IEEE Antennas and Wireless Propagation Letters*, vol. 8, pp. 1091–1093, 2009.

[4] M. Fernandes, A. Bhandare, C. Dessai, and H. Virani, "A wideband switched beam patch antenna array for LTE and Wi-Fi," in *Proceedings of the IEEE India Conference (INDICON '13)*, pp. 1–6, December 2013.

[5] W. P. M. N. Keizer, "Fast low-sidelobe synthesis for large planar array antennas utilizing successive fast fourier transforms of the array factor," *IEEE Transactions on Antennas and Propagation*, vol. 55, no. 3, pp. 715–722, 2007.

[6] M. D. Migliore, "MIMO antennas explained using the Woodward-Lawson synthesis method," *IEEE Antennas and Propagation Magazine*, vol. 49, no. 5, pp. 175–182, 2007.

[7] L. G. U. Garcia, M. A. Ingale, P.-H. Michaelsen, K. I. Pedersen, and P. E. Mogensen, "Impact of the pilot signal per beam on the ideal number of beams and capacity gain of switched beam forming for WCDMA," in *Proceedings of the IEEE 63rd Vehicular Technology Conference (VTC '06)*, vol. 6, pp. 2808–2812, July 2006.

[8] J. Ramiro-Moreno, K. I. Pedersen, and P. E. Mogensen, "Capacity gain of beamforming techniques in a WCDMA system under channelization code constraints," *IEEE Transactions on Wireless Communications*, vol. 3, no. 4, pp. 1199–1208, 2004.

[9] B. Allen and M. Beach, "On the analysis of switched-beam antennas for the WCDMA downlink," *IEEE Transactions on Vehicular Technology*, vol. 53, no. 3, pp. 569–578, 2004.

[10] Z. Imran and C. Panagamuwa, "Beam-switching planar parasitic antenna array," in *Proceedings of the Loughborough Antennas and Propagation Conference (LAPC '14)*, pp. 160–164, IEEE, Loughborough, UK, November 2014.

[11] J.-W. Baik, S. Pyo, T.-H. Lee, and Y.-S. Kim, "Switchable printed Yagi-Uda antenna with pattern reconfiguration," *ETRI Journal*, vol. 31, no. 3, pp. 318–320, 2009.

[12] C. Kittiyanpunya and M. Krairiksh, "Pattern reconfigurable printed Yagi-Uda antenna," in *Proceedings of the International Symposium on Antennas and Propagation (ISAP '14)*, pp. 325–326, December 2014.

[13] W. R. Deal, N. Kaneda, J. Sor, Y. Qian, and T. Itoh, "A new quasi-yagi antenna for planar active antenna arrays," *IEEE Transactions on Microwave Theory and Techniques*, vol. 48, no. 6, pp. 910–918, 2000.

[14] R.-N. Cai, M.-C. Yang, S. Lin, X.-Q. Zhang, X.-Y. Zhang, and X.-F. Liu, "Design and analysis of printed Yagi-Uda antenna and two-element array for WLAN applications," *International Journal of Antennas and Propagation*, vol. 2012, Article ID 651789, 8 pages, 2012.

[15] N. Nikolic and A. R. Weily, "Printed quasi-vagi antenna with folded dipole driver," in *Proceedings of the IEEE International Symposium on Antennas and Propagation and USNC/URSI National Radio Science Meeting (APSURSI '09)*, pp. 1–4, June 2009.

[16] J. Werner, J. Wang, A. Hakkarainen, M. Valkama, and D. Cabric, "Primary user localization in cognitive radio networks using sectorized antennas," in *Proceedings of the 10th Annual Conference on Wireless On-Demand Network Systems and Services (WONS '13)*, pp. 155–161, March 2013.

[17] D. Halliday, R. Resnick, and J. Walker, *Fundamentals of Physics*, John Wiley & Sons, 8th edition, 2007.

[18] T. Rappaport, *Wireless Communications: Principles and Practice*, Prentice Hall, 2nd edition, 2002.

[19] J. R. Fernandez, M. Quispe, G. Kemper, J. Samaniego, and D. Díaz, "Adjustments of log-distance path loss model for digital television in lima," *Proceedings of the 30th Simposio Brasileiro de Telecomunicações*, pp. 13–16, September 2012.

[20] IEEE, "IEEE standard for definitions of terms for antennas," IEEE Standard 145-2013, IEEE Standards Association, 2014, (Revision of IEEE Std 145-1993).

[21] J. M. Johnson and Y. Rahmat-Samii, "Genetic algorithms in engineering electromagnetics," *IEEE Antennas and Propagation Magazine*, vol. 39, no. 4, pp. 7–21, 1997.

[22] J. M. Johnson and Y. Rahmat-samii, "Genetic algorithm optimization and its application to antenna design," in *Proceedings of the IEEE Antennas and Propagation International Symposium*, vol. 1, pp. 326–329, June 1994.

[23] S. Koziel and S. Ogurtsov, "Linear antenna array synthesis using gradient-based optimization with analytical derivatives," in *Proceedings of the IEEE Antennas and Propagation Society International Symposium (APSURSI '12)*, pp. 1–2, Chicago, Ill, USA, July 2012.

[24] M. K. Karray, "User's mobility effect on the performance of wireless cellular networks serving elastic traffic," *Wireless Networks*, vol. 17, no. 1, pp. 247–262, 2011.

[25] M. Alasti, B. Neekzad, J. Hui, and R. Vannithamby, "Quality of service in WiMAX and LTE networks," *IEEE Communications Magazine*, vol. 48, no. 5, pp. 104–111, 2010.

Hindawi Publishing Corporation
International Journal of Antennas and Propagation
Volume 2015, Article ID 904153, 13 pages
http://dx.doi.org/10.1155/2015/904153

Research Article

On the Cross Correlation Properties of MIMO Wideband Channels under Nonisotropic Propagation Conditions

Ana Maria Pistea[1] and Hamidreza Saligheh Rad[2]

[1] *Military Technical Academy, Bucharest, 050141 Bucharest, Romania*
[2] *Tehran University of Medical Sciences, Tehran 16656, Iran*

Correspondence should be addressed to Hamidreza Saligheh Rad; hamid.saligheh@gmail.com

Received 20 August 2014; Accepted 12 December 2014

Academic Editor: Xinyi Tang

Wideband (WB) and ultrawideband (UWB) systems combined with multiple-input multiple-output (MIMO) technology increase both the systems performances and the complexity of the channel models required to evaluate their capabilities. Because in real scenarios waves propagate nonisotropically, the accuracy of the channel model is increased if nonisotropic propagation is considered. The channel bandwidth is the key term in the evaluation process of these systems because large bandwidths introduce frequency selectivity, a unique phenomenon of WB and UWB systems with more complexity in the latter case. This is due to the fact that, unlike WB technology in which the propagating signal is the only affected parameter by the frequency selectivity, in the UWB case, this phenomenon also affects the antenna propagation pattern (APP). In this paper, we developed a novel channel model based on the statistical analysis of two-dimensional cross correlation functions (CCFs) of WB/UWB MIMO nonisotropic channels. A mathematical solution to assess the frequency selective behavior of the UWB APP is also presented. The CCF reveals how the power spectral density (PSD) of the channel is influenced by bandwidth, nonisotropic propagation, and APP.

1. Introduction

The design of high quality wideband (WB) and ultrawideband (UWB) multiple-input multiple-output (MIMO) wireless systems requires the development of two-dimensional (2D) space-time-frequency (STF) channel models along with the evolution from narrowband (NB) to WB/UWB transmissions. This evolution from NB to WB/UWB MIMO channels brings new and more complex propagation phenomena involving the following open questions.

(1) What are the main propagation phenomena that appear in a 2D propagation scenario when the channel bandwidth increases?

(2) In a 2D scenario, how does the influence of the antenna propagation pattern (APP) on NB channels differ from the influence of the APP on WB/UWB channels characteristics?

(3) Is a 2D channel model developed for the study of WB channels adequate for the analysis of UWB channels?

An exhaustive approach to characterize WB/UWB MIMO channels and to answer the questions enumerated above is to statistically analyze the behavior of their space-time-frequency (STF) channel transfer functions (CTFs). We propose a model for both WB and UWB MIMO channels based on two-dimensional (2D) STF cross correlation function (CCF) between the CTFs of two subchannels of a multicarrier (orthogonal frequency division multiplexing, OFDM) channel. A subchannel represents the connection between two antennas, one at the base station (BS) and the other at the mobile station (MS), which transmit/receive the signal at specific time and frequency.

The calculation of the CCF for WB/UWB MIMO channels has attracted the attention of several researchers, for example, [1–5]. Ma and Pätzold extended an NB MIMO channel model to a version adequate for WB channels analysis. The main improvement made to extend the applicability of the NB model was to add the elements which introduce the frequency selectivity caused by the propagation channel. This model presents the 2D CCF derived only for isotropic propagation

[1]. Pätzold and Hogstad developed a WB MIMO channel model with temporal, spatial, and frequency correlation properties. This model presents the 2D CCF derived for both isotropic and nonisotropic propagation assuming a specific geometry of scatterers around receiver [2]. Saleh and Valenzuela (S-V) developed one of the first UWB channel models which was proposed to reproduce the multipath effect of indoor environments. Using S-V results, Zou et al. determined a CCF expression of multiband OFDM-UWB discrete-time base-band channel impulse response [3, 4]. Abdi and Kaveh propose an ST-CCF for a MIMO frequency nonselective Rician fading channel, assuming a one ring of scatterers model around the MS [5]. This model is as an example of an outdoor environment, where the von-Mises probability density function (PDF) is suggested to model the nonisotropic propagation environment around the user.

As a summary, our literature review shows that the general approach is to develop channel models for WB transmissions separated from the channel models for UWB communications. Another trend is to include the effects of the propagation environment (waves clustering, frequency selectivity) and to ignore the frequency selective behavior of the antenna patterns. Because UWB systems were mainly developed for indoor applications the research in the field of UWB outdoor channel modeling was not a priority [6–8]. From the literature review, it was also observed that most of the MIMO-CCF models are based on a specific geometry for scatterers distribution around MS to characterize the nonisotropic propagation.

Lately, UWB technology in combination with MIMO systems finds more and more interest in areas such as location tracking application for outdoor emergency services [9, 10], location tracking and sensor applications for mobile outdoor users [11], and medical [12] and electronic warfare applications [13]. Even more, some research results [14–16] proved that a joint radar and wireless communication system would constitute a unique platform for future intelligent environmental sensing and ad hoc communication networks, in terms of both spectrum efficiency and cost effectiveness. This evolution regarding the use of UWB systems in outdoor environments, as radar or communication system, has led to the formulation of specific requirements aiming at investigating the influence of outdoor propagation on UWB mobile systems [17, 18].

The model proposed in this paper describes the CCF between two subchannels of an outdoor WB/UWB MIMO channel employing directional and omnidirectional antennas and in the presence of nonisotropic wave propagation in 2D space. Instead of assuming a specific geometry for scatterers in space (models based on specific geometries of scatterers in the space are just able to predict the behavior of that particular propagation scenario), we used specific mathematical relationships between the physical parameters of the wireless channel along with appropriate assumptions on their PDFs to derive a channel model based on the CCF of outdoor WB and UWB MIMO channels. This model is an extension of a 2D NB channel model [19]. The evolution through systems with (ultra)wide bandwidths implies new propagation effects that make the NB model inappropriate for WB/UWB transmissions. In order to extend the NB channel model to a version adequate for WB/UWB channels analysis, the mathematical structure of the model needs to be updated with the elements which characterize the new propagation phenomena (represented by channel frequency selectivity, waves clustering) and with the elements which define the performances of the new systems (represented by operating bandwidth, frequency selectivity of the antenna). We represent the nonisotropic scatterers by the Fourier series expansion (FSE) of the PDF of the propagating directions. We also consider the effect of directional and omnidirectional antenna element patterns by the FSE of the APPs. The expression of the CCF turns out to be a composition of linear expansions of Bessel functions of the first kind. Fourier analysis of the derived CCF is used to determine the power spectral density (PSD) of WB and UWB channels in a stationary scenario. The mathematical set-up of the stationary scenario transforms the MIMO channel into a multiple-input single-output (MISO) channel to be analyzed as a special case. The contribution in this 2D-CCF model is fourfold.

(1) It includes the main propagation phenomena that appear in 2D WB/UWB MIMO outdoor scenarios and permits the evaluation of combined effects of channel bandwidth, nonisotropic scattering, APP (omnidirectional or directional), and the array interelement distance on the CCF of WB and UWB MIMO channels.

(2) This model can be used for the analysis of both WB and UWB propagation channels. The key to apply a model for the analysis of both types of channels is to use the appropriate expressions for APPs. Since WB APP is not frequency selective, the relative bandwidth being a small fraction of the central frequency and the UWB APP is frequency selective and different antenna patterns expressions for these two types of systems should be used. In this paper we propose mathematical expression for UWB APP.

(3) It accurately reflects the influence of the MS direction (and speed) on the spectral characteristics of WB and UWB channels.

(4) It gives mathematical expressions to evaluate the channel power spectrum of WB and UWB wireless channels.

In [20] a three-dimensional (3D) version of this model was presented. The difference between 2D and 3D versions of the proposed model consists of APP and nonisotropic propagation representations. In the case of the 2D model the APP and the propagation environment are represented depending on azimuth angle spread (AAS). The 3D version of the model represents these two elements as a function of both AAS and elevation angle spread (EAS). From the obtained results it was observed that the 2D model provides a good representation of how the frequency selectivity affects the signal spectrum. A 2D model for most propagation environments is more eligible when we get closer to the ground because a propagation environment behaves similar

to a 2D environment. Another advantage is that such model represents the propagation environment fairly accurately, with minimum complexity and difficulty. The model presented in this paper is an extension of the conference paper presented in [21]. There are significant differences between the results presented in [21] and the content of the current work, where both the CCF and the PSD are derived and evaluated for WB/UWB MIMO channels while [21] describes only the PSD of WB/UWB systems in a stationary case for MISO channels. The latter paper is mostly about PSD, the derivation process of the CCF (which is the root of the PSD) was not presented, and the model cannot be extended to be used in other scenarios (e.g., indoor propagation, MIMO channels). This statement is also valid for [20] which does not contain the derivation process of the three-dimensional CCF. In the present work are provided details regarding the calculation of the moment generating functions (MGFs-$\Phi_{\tau,s}$) of the delay profile (τ, T) and details regarding the calculation of the number of Fourier series coefficients (FSCs) for different PDFs of the AAS necessary to approximate Laplace and von-Mises distributions and how they are further involved in assessing the CCF. Since in [20, 21] CCF was not derived and graphically represented this connection between FSCs, APP, distribution of the propagation environment and CCF behavior cannot be established.

The rest of this paper is organized as follows: in Section 2, the notations and the parameters included in the 2D WB/UWB channels model are described; in Section 3, the WB/UWB CCF expression is derived and is numerically evaluated. In Section 4, the Fourier analysis of the CCF which results in the PSD of the WB and UWB channels is presented; in Section 5, conclusions are presented.

2. Two-Dimensional Wideband/UWB MIMO Model Description

In this section, we describe the propagation scenario, the notations used throughout this paper, and the elements (accompanied by their mathematical expressions) introduced in the structure of the CTF valid for WB and UWB channels. We also emphasize the differences which exist between WB and UWB channel models and how these differences are included in our model.

By definition, a channel is considered WB if the fractional bandwidth (B_f) (the ratio of bandwidth at −10 dB points to center frequency) is $1\% < B_f \leq 20\%$ while UWB channels are characterized by $20\% < B_f \leq 200\%$ [22–24]. For both, WB and UWB scenarios, we consider a moving MS with a constant speed vector V (m/sec) and a fixed BS in a 2D nonisotropic propagation environment. The resulting CTF is determined by the pth transmitting antenna element at the BS side, the propagation environment, and the mth receiving antenna element at the MS. CTF description is based on two categories of elements: (C1) elements assigned to the communication system, which are the system bandwidth and APPs at the BS and at the MS, and (C2) elements assigned to the wireless channel represented by nonisotropic propagation, frequency selectivity, and clustering phenomenon. Both categories of elements enumerated above changed their mathematical representation once with the evolution from NB to WB and UWB channels as it is presented in the following lines.

(C1) The APPs of the pth and mth antenna of the BS and the MS array, $G_p^B(\Theta^B, \omega)$, $G_m^M(\Theta^M, \omega)$, give the response of the antenna in terms of the propagation directions, Θ, and frequency, ω. These functions implicitly include the effect of mutual coupling caused by the neighboring antenna elements. Are all periodic functions of 2π, where Θ^B- and Θ^M- are unity vectors which represent a propagation direction (DOD or DOA) at BS or MS, respectively. We assume that the DOA (to the receiver) and the DOD (from the transmitter) are independent. Therefore, we represent them by their FSCs as follows:

$$G(\Theta;\omega) = \sum_{k=-\infty}^{\infty} \mathcal{G}_k e^{jk\Theta}, \quad \mathcal{G}_k = \frac{1}{2\pi}\int_{-\pi}^{\pi} G(\Theta;\omega)\, e^{-jk\Theta} d\Theta. \tag{1}$$

For NB channels, it is assumed that the response of the antenna does not change significantly over the bandwidth since the relative bandwidth is a small fraction of the central frequency [19]. This assumption is also true for WB channels but proved to be false once with the evolution through ultrawide bandwidths. UWB antenna patterns are frequency selective and this characteristic should be considered in the design process of UWB channel models. The radiation pattern depicts the relative strength distribution of the transmitted or received power by the antenna. In [25, page 19] it is suggested that, in order to correctly evaluate the received and the transmitted power of UWB signals, the radiation pattern should be determined across the entire frequency spectrum. This requirement is the consequence of the frequency selectivity phenomenon. Thus, according to the method suggested in [25], depending on the signal bandwidth, we propose two approaches for 2D APP calculation as follows:

(a) for WB signals, APP is calculated depending on the central angular frequency, ω;

(b) for UWB signals, we calculate APP depending on the central frequency and by integrating $G(\Theta, \omega)$ across all the frequencies of the transmitted signal.

Table 1 presents the APPs of two WB/UWB antennas. The helical (directional) and rectangular (omnidirectional) antennas are often used for antenna arrays and (ultra)wide bandwidth applications [22].

f_H, f_L are the upper and the lower frequencies of the UWB channel bandwidth, the parameter h is proportional with the size of the antenna, and G_0 is the real and positive constant antenna gain that varies for each antenna.

(C2) The nonisotropic propagation is characterized by the nonuniform distribution of the waveforms around the MS and the BS in space. In order to describe a nonisotropic channel the PDF of the propagating directions, known as azimuth angular spread (AAS), can be used. In the proposed model, the PDF of the propagation directions is denoted by $f^B(\Theta^B)$, at the BS, and $f^M(\Theta^M)$, at the MS. One candidate for

Table 1: 2D antenna radiation patterns.

Antenna type		APP, $G(\Theta,\omega)$, $\forall\Theta \in [-\pi,\pi)$
Helical antenna	WB	$jG_0 \cdot \frac{\omega}{2c} \cdot h \cdot \sin\Theta$
	UWB	$\frac{1}{(f_H - f_L)} \int_{f_L}^{f_H} jG_0 \cdot \frac{\omega}{2c} \cdot h \cdot \sin\Theta d\omega$
Rectangular antenna	WB	$jG_0 \frac{\sin(((\omega/2c) \cdot h \cdot \sin\Theta))}{((\omega/2c) \cdot h \cdot \sin\Theta)}$
	UWB	$\frac{1}{(f_H - f_L)} \int_{f_L}^{f_H} jG_0 \frac{\sin(((\omega/2c) \cdot h \cdot \sin\Theta))}{((\omega/2c) \cdot h \cdot \sin\Theta)} d\omega$

Table 2: Nonisotropic AAS and corresponding Fourier series coefficients.

PDF, $f_\Theta(\Theta)$, $\forall\Theta \in [-\pi,\pi)$, $\mathscr{F}_k$	
Laplace	$f_\Theta(\Theta) = \frac{e^{\lvert((-\sqrt{2}\Theta)/\sigma)\rvert}}{\sqrt{2}\sigma}$
	$\mathscr{F}_k = \frac{e^{-((\pi(\sqrt{2}+jk\sigma))/\sigma)}(e^{((2\sqrt{2}\pi)/\sigma)} - e^{j2k\pi})}{2\pi(j\sqrt{2}k\sigma - 2)}$
Von-Mises	$f_\Theta(\Theta) = \frac{e^{\lvert n*\cos(\Theta-\mu)\rvert}}{2\pi J_0(n)}$
	$\mathscr{F}_k = \frac{J_k(n)}{J_0(n)}$

the PDF of the nonisotropic AAS is Laplace distribution [26]. Another distribution which characterizes the nonisotropic environment is the von-Mises PDF [27]. Since these PDFs are periodic functions with period 2π, in Table 2 we represent them by the corresponding FSC:

$$f_\Theta(\Theta) = \sum_{k=-\infty}^{+\infty} \mathscr{F}_k e^{jk\Theta}, \quad \mathscr{F}_k = \frac{1}{2\pi}\int_{-\pi}^{\pi} f_\Theta(\Theta) e^{-jk\Theta} d\Theta. \tag{2}$$

Von-Mises PDF is strongly influenced by parameter n, which determines the order of the channel nonisotropy. In other words n controls the width of DOA of scattered components. This parameter can take values in the range $n \in [0,\infty)$. When $n \to \infty$, $f_{\Theta^M}(\Theta) = \delta(\Theta - \mu)$, the propagation environment is considered extremely nonisotropic-scattered concentrated at $\Theta = \mu$, where $\mu \in [-\pi,\pi)$ is the mean DOA at the MS. For large n, say $3 \le n \le 20$, we have a typical nonisotropic environment [27]. When FSCs are determined this parameter appears in the argument of the Bessel functions represented by the modified Bessel function of the first kind, $J_k(\cdot)$, and the zero-order modified Bessel function, $J_0(\cdot)$.

The isotropic propagation environment can be mathematically represented in a similar way, using the following expression of the FSC: $\mathscr{F}_k = (1/2\pi)\delta_k$. Laplace and von-Mises distributions are specific to WB/UWB MIMO channels.

The complexity of the nonisotropic propagation environment is increased by two phenomena which appear only in the case of WB and UWB channels.

Clustering Phenomenon. NB systems receive most of the multipath components (MPCs) within the symbol duration. In these circumstances, the receiver acts as if there was a single multipath component. Due to the better time resolution of WB and UWB systems the multipath components tend to arrive in cluster, rather than in a continuum as it is common for NB channels. The authors of [28] define a cluster as an accumulation of MPCs with similar time of arrivals and angle of arrivals. As a consequence of this phenomenon, the CTF of WB/UWB channels is the summation of the dominant I paths and L clusters. In the case of NB channels the CTF appeared to be only the summation of I paths.

The propagation delay of the ith path within the lth cluster between the pth (at the BS) and mth (at the MS) antenna elements $\tau_{pm,il}$ is decomposed into three components: one component which represents the delay depending on the distance between BS and MS and other two components which vary as a function of the local coordinates of BS and MS:

$$\tau_{pm,il} = \tau_{il} - \left(\tau_{p,il}^B + \tau_{m,il}^M\right),$$
$$\tau_{p,il}^B \triangleq \frac{a_p^B \Theta_{il}^B}{c}; \qquad \tau_{m,il}^M \triangleq \frac{a_m^M \Theta_{il}^M}{c}, \tag{3}$$

where $(\cdot)^T$ represents the transpose operator, τ_{il} is the delay between local coordinates O^B or O^M, and $\tau_{p,il}^B$, $\tau_{m,il}^M$ represent the propagation delays from antenna a_p^B to a_m^M located in their corresponding coordinates O^B or O^M. T_l is the cluster arrival rate and is considered to be constant in time. Θ_{il}^B and Θ_{il}^M were previously defined.

Frequency Selectivity Phenomenon. This refers to the different attenuation that the signal subbands undergo. In our model, the frequency selectivity of the radio channel is characterized by two components. These components are represented by APP (valid only for UWB channels) and by the term $(\omega_{bw}/\omega)^\eta$. The parameter ω_{bw} represents the signal bandwidth $\omega_{bw} = \omega_H - \omega_L$; ω_L and ω_H are the lower and the upper angular frequencies. η depends on the geometric configuration of the objects which produce the signal's diffraction. The following values can be assigned to η: -1 (diffraction by corner or tip), 0.5 (diffraction by axial cylinder face), and 1 (diffraction by broadside of a cylinder) [29]. When modeling NB channels, it was adequate to define the path gain depending on the path time-delay [19]. This is not sufficient for WB/UWB MIMO channels

where the frequency selectivity phenomenon influences the gain of the channel. In the ray based propagation models which can be applied to signals transmitted at high frequency ranges, like WB and UWB signals, it can be assumed that one propagation path has DOA and time of arrival that does not depend on frequency but has a frequency dependent complex path gain. In our model the path gain of the ith path within the lth cluster which propagates from the pth antenna to the mth antenna is expressed as the extension of Friis' transmission formula $g_{pm,il} = 1/2\omega\tau_{il}$.

When putting together the elements described in (C1) and (C2), the CTF of WB and UWB channels results in the following expression:

$$h_{pm}(t,\omega) = \left(\frac{\omega_{bw}}{\omega}\right)^{\eta} \sum_{l=1}^{L}\sum_{i=1}^{I} G_p^B\left(\Theta_{il}^B;\omega\right) \times G_m^M\left(\Theta_{il}^M;\omega\right) g_{pm,il} e^{j(\phi_{il}-\overline{\omega_{il}}t-\omega\tau_{il}-\omega T_l)}. \quad (4)$$

The resulting CTF is represented by the double summation of clusters, l, and of the propagation waveforms, i, over a maximum number of clusters, L, and paths, I. Within each cluster (path) the signal reaches the receiver with a response described by the PDFs of some random variables. These random variables are phase, delay, DOD, and DOA. In the resulting CTF each l cluster and implicitly each i wave are associated with a path attenuation gain, $g_{pm,il}$, a path phase shift, ϕ_{il}, and a time-varying delay, $\tau_{pm,il}(t) \triangleq \tau_{pm,il} + (t/c)V^T\Theta_{il}^M$. The Doppler shift, of the ith received wave within the lth cluster, is represented by $\overline{\omega_{il}} = (\omega/c)V^T\Theta_{il}^M$ where V and c are the MS velocity vector and the speed of light, respectively.

3. Two-Dimensional Cross Correlation Function of WB/UWB MIMO Channels

The CCF expression of the CTFs, $h_{pm}(t_1,\omega_1)$ and $h_{qn}(t_2,\omega_2)$, of two arbitrary subchannels of a MIMO channel is the result of the following definition:

$$R_{pm,qn}(t_1,t_2,\omega_1,\omega_2) \triangleq E\left[h_{pm}(t_1,\omega_1)\, h_{qn}^*(t_2,\omega_2)\right]. \quad (5)$$

In the CCF expression there are three dimensions: space, two pairs of antenna elements (p,m,q,n), time (t_1,t_2), and central frequencies (ω_1,ω_2). According to these three dimensions, we call it STF-CCF. The expectation operation is performed over all introduced random variables. In the presence of enough number of multipaths by invoking the central limit theorem the CTF can be considered a Gaussian random process. Therefore, the above second-order statistics fully characterize statistical behavior of the channel. By replacing (4) with (5), the CCF results in the following expression:

$$\begin{aligned} R_{pm,qn}(t_1,t_2,\omega_1,\omega_2) &= \frac{(\omega_{bw1}\omega_{bw2})^{\eta}}{(\omega_1\omega_2)^{\eta}} \\ &\times \sum_{l=1}^{L}\sum_{i=1}^{I}\Big\{E\Big[G_p^B\left(\Theta_{i_1l_1}^B;\omega_1\right) G_m^M\left(\Theta_{i_1l_1}^M;\omega_1\right) \\ &\quad \times g_{pm,i_1l_1} \times g_{qn,i_2l_2} \\ &\quad \times e^{(-j\omega_1 T_{pm,l_1} - j\omega_1\tau_{pm,i_1l_1}(t_1))}\Big] \\ &\times E\Big[G_q^{B^*}\left(\Theta_{i_2l_2}^B;\omega_2\right) G_n^{M^*}\left(\Theta_{i_2l_2}^M;\omega_2\right) \\ &\quad \times e^{j(\phi_{i_1l_1}-\phi_{i_2l_2})} \\ &\quad \times e^{(-j\omega_2 T_{qn,l_2} - j\omega_2\tau_{qn,i_2l_2}(t_2))}\Big]\Big\}. \end{aligned} \quad (6)$$

Regrouping dependent and independent random variables and using the elements described in (C1) and (C2) we obtain

$$\begin{aligned} R_{pm,qn}(t_1,t_2;\omega_1,\omega_2) &= \frac{(\omega_{bw1}\omega_{bw2})^{\eta}}{(\omega_1\omega_2)^{\eta}(4\omega_1\omega_2)} \\ &\times \Bigg\{\sum_{l=1}^{L}\sum_{i=1}^{I} E\Big[\left(\tau_{i_2l_2}\tau_{i_1l_1}\right)^{-1} \\ &\quad \times e^{j((\omega_2\tau_{i_2l_2}-\omega_1\tau_{i_1l_1})+(\omega_2 T_{l_2}-\omega_1 T_{l_1}))}\Big] \\ &\times E\left[e^{j(\phi_{i_1,l_1}-\phi_{i_2,l_2})}\right] \\ &\times E\Big[G_p^B\left(\Theta_{i_1l_1}^B;\omega_1\right) G_q^{B^*}\left(\Theta_{i_2l_2}^B;\omega_2\right) \\ &\quad \times e^{j((\omega_1/c)a_p^{B^T}\Theta_{i_1l_1}^B-(\omega_2/c)a_q^{B^T}\Theta_{i_2l_2}^B)}\Big] \\ &\times E\Big[G_m^M\left(\Theta_{i_1l_1}^M;\omega_1\right) G_n^{M^*}\left(\Theta_{i_2l_2}^M;\omega_2\right) \\ &\quad \times e^{j((\omega_1/c)(a_m^M-Vt_1)^T\Theta_{i_1l_1}^M-(\omega_2/c)(a_n^M-Vt_2)^T\Theta_{i_2l_2}^M)}\Big]\Bigg\}. \end{aligned} \quad (7)$$

Equations (8)÷(14) present the calculation methodology of the expectations in (7). We present the calculation methodology at the MS side but one should note that the same calculation procedure is valid for the BS side. The calculation of this equation is performed for two cases.

Case 1. The paths are considered similar and this is equivalent to $i_1 = i_2 = i, l_1 = l_2 = l$; some of the random variables in this expression become identical and, by using the Fourier series

expansions for both APPs and AASs, we are able to calculate these expectations either at the BS or at the MS.

Case 2. The paths are considered to be dissimilar. This is equivalent to $i_1 \neq i_2$, $l_1 \neq l_2$; we assume that the DOD or DOA PDFs of different propagation waves are independent of each other; that is, $\Theta^M_{i_1 l_1}$ and $\Theta^M_{i_2 l_2}$ (or $\Theta^B_{i_1 l_1}$ and $\Theta^B_{i_2 l_2}$) are independent.

(i) The calculation of the first expectation in (7) is carried out as follows:

$$E\left[\left(\tau_{i_2 l_2}\tau_{i_1 l_1}\right)^{-1} e^{j(\omega_2 \tau_{i_2 l_2} - \omega_1 \tau_{i_1 l_1})} \times e^{(\omega_1 T_{m,p,l_1} - \omega_2 T_{m,p,l_2})}\right] = \begin{cases} \Phi_\tau^{(-1)}\left(j\left(\omega_2-\omega_1\right)\right) \\ \quad \times \Phi_T\left(j\left(\omega_1-\omega_2\right)\right), & \text{Case 1}, \\ \Phi_\tau^{(-1)}\left(j\omega_2\right)\Phi_\tau^{(-1)}\left(-j\omega_1\right) \\ \quad \times \Phi_T\left(-j\omega_2\right)\Phi_T\left(j\omega_1\right), & \text{Case 2}. \end{cases} \tag{8}$$

The elements denoted by $\Phi_{\tau,T}(s)$ represent the moment generating functions (MGFs) of the delay profile (τ, T) evaluated at the difference between two frequencies. $\Phi_{\tau,T}(s)$ suggests that channel similarity depends on frequency differences and not on absolute frequencies. The value of this parameter tends to decay when the frequency differences increase. The definition of the MGF of a random variable x with the PDF $f_X(x)$ is defined as follows [30, page 415]: $\Phi_X(s) = E[e^{jsX}] = \int_{-\infty}^{\infty} e^{js\xi} f_X(\xi) d\xi$. The probability densities of the absolute times of arrival of clusters and paths used to calculate the MGFs are represented by [31]

$$p_{T_l}(T) = \frac{\Lambda^{L+1} T^L e^{-\Lambda T}}{L!}, \qquad p_{\tau_{i,l}}(\tau) = \frac{\lambda^I \tau^{I-1} e^{-\lambda\tau}}{(I-1)!}, \tag{9}$$

where Λ and λ are the cluster arrival rate and ray arrival rate. The parameter $1/\Lambda$ is typically in the range of 10–50 ns, while $1/\lambda$ shows wide variations from 0.5 ns in non-line-of-sight (NLOS) situations to more than 5 ns in LOS situations [32].

(ii) The calculation of the second expectation in (7) is performed as follows.

Considering the case of the planar wave propagation, we take into account the phase contribution of surrounding scatterers by a random phase change parameter $\phi_{il} \sim U[-\pi, \pi)$. Since the path phase shifts, ϕ_{il}, appear in (4) in the form of $e^{j\phi_{il}}$, the correlations of $e^{j\phi_{il}}$ over different paths and clusters, $E[e^{j(\phi_{i_1 l_1} - \phi_{i_2 l_2})}]$, have impact on the channel characteristics. We assume that $E[e^{j(\phi_{i_1 l_1} - \phi_{i_2 l_2})}]$ can take the following values:

$$E\left[e^{j(\phi_{i_1,l_1} - \phi_{i_2,l_2})}\right] = \begin{cases} 1, & \text{Case 1}, \\ k^2, & \text{Case 2}. \end{cases} \tag{10}$$

(iii) The calculation of the third expectation in (7) is based on the following methodology:

$$\begin{aligned} \text{Case 1}: E\Big[&G_m^M\left(\Theta_{il}^M;\omega_1\right) G_n^{M^*}\left(\Theta_{il}^M;\omega_2\right) \\ &\times e^{j((\omega_1/c)(a_m^M - Vt_1)^T \Theta_{il}^M - (\omega_2/c)(a_n^M - Vt_2)^T \Theta_{il}^M)}\Big] \\ &= \int_{-\pi}^{\pi} G_m^M\left(\Theta_{il}^M;\omega_1\right) G_n^{M^*}\left(\Theta_{il}^M;\omega_2\right) \\ &\qquad \times e^{(j/c)(d_{mn}^M)^T \Theta_{il}^M} f_{\Theta^M}\left(\Theta_{il}^M\right) d\Theta_{il}^M \\ &= \int_{-\pi}^{\pi} \sum_{k=-\infty}^{\infty} \left(\mathcal{G}_{m,k}^M(\omega_1) \otimes \mathcal{G}_{n,-k}^{M^*}(\omega_2) \otimes \mathcal{F}_k^M\right) \\ &\qquad \times e^{jk\Theta_{il}^M + j(|d_{mn}^M| \cos(\Theta_{il}^M - \angle d_{m,n}^M)/c)} d\Theta_{il}^M \\ &= 2\pi \sum_{k=\infty}^{\infty} j^k e^{jk\angle d_{m,n}^M} \\ &\qquad \times \left(\mathcal{G}_{m,k}^M(\omega_1) \otimes \mathcal{G}_{n,-k}^{M^*}(\omega_2) \otimes \mathcal{F}_k^M\right) J_k\left(\frac{\left|d_{mn}^M\right|}{c}\right), \end{aligned} \tag{11}$$

where $\mathcal{G}_{m,k}^M$, $\mathcal{G}_{n,k}^M$, and $\mathcal{F}_k^M$ are the FSCs of the APPs (defined in (1)) and the AAS (defined in (2)) in the corresponding coordinates, respectively, $J_k(u) \triangleq (j^{-k}/\pi)\int_0^\pi e^{j(k\xi + u\cos\xi)} d\xi$ is the kth-order Bessel function, $\otimes$ is the linear convolution, and $|\cdot|$ is the Euclidean norm.

The definition of the linear convolution can be formulated as follows [33, page 155]: given two discrete-time signals, x_n and y_n, the linear convolution between them is defined as follows: $z_n \triangleq x_n \otimes y_n = \sum_{k=\infty}^{\infty} x_k y_{n-k}$.

The vectors and $d_{m,n}^M$ and $d_{p,q}^B$ are the separation vectors between two antenna elements at the MS (m, n) and at the BS (p, q). Large distances often result in less STF correlation as the Bessel functions asymptotically decrease. The norms of $d_{m,n}^M$ and $d_{p,q}^B$ represent shifted distances (between $\omega_1 a_p^B$ and $\omega_2 a_q^B$) at the BS and (between $\omega_2(t_2 V + a_n^M)$ and $\omega_1(t_1 V + a_m^M)$) at the MS. Parameters $d_{(\cdot,\cdot)}^{(\cdot)}$ contain space, time, and frequency separations between $h_{pm}(t_1, \omega_1)$ and $h_{qn}(t_2, \omega_2)$. These two vectors, illustrate theimpact of the antennas' location (spatial correlation), of thecarrier frequencies (frequency correlation), of the time indices and of the mobile speed on the CCF at BS and MS. The value of the $d_{m,n}^M$ and $d_{p,q}^B$ can be determined based on the following equations:

$$\begin{aligned} &d_m^M \triangleq \omega_1\left(a_m^M - t_1 V\right), \qquad d_n^M \triangleq \omega_2\left(a_n^M - t_2 V\right), \\ &d_{m,n}^M \triangleq \left(\omega_2 t_2 - \omega_1 t_1\right) V + \left(\omega_1 a_m^M - \omega_2 a_n^M\right), \\ &d_p^B \triangleq \omega_1 d_p^B, \qquad d_q^B \triangleq \omega_2 d_q^B, \qquad d_{p,q}^B \triangleq \omega_1 a_p^B - \omega_2 a_q^B. \end{aligned} \tag{12}$$

Similar to the calculation in the first case, for the second case, we have (in MS)

$$\begin{aligned}\text{Case 2}: E\Big[&G_m^M\left(\Theta_{i_1l_1}^M;\omega_1\right)G_n^{M^*}\left(\Theta_{i_2l_2}^M;\omega_2\right)\\&\times e^{j((\omega_1/c)(a_m^M-Vt_1)^T\Theta_{i_1l_1}^M-(\omega_2/c)(a_n^M-Vt_2)^T\Theta_{i_2l_2}^M)}\Big]\\=&\left(2\pi^2\right)\\&\times\left[\sum_{k=-\infty}^{\infty}j^k e^{jk\angle d_m^M}\left(\mathcal{G}_{m,k}^M(\omega_1)\otimes\mathcal{F}_k^M\right)J_k\left(\frac{\left|d_m^M\right|}{c}\right)\right]\\&\times\left[\sum_{k=-\infty}^{\infty}j^k e^{jk\angle d_n^M}\left(\mathcal{G}_{n,-k}^M(\omega_2)\otimes\mathcal{F}_k^M\right)J_k\left(\frac{\left|d_n^M\right|}{c}\right)\right].\end{aligned}\tag{13}$$

We formulate the CCF including both cases using the derivations presented above:

$$\begin{aligned}&R_{pm,qn}(t_1,t_2,\omega_1,\omega_2)\\&=\frac{(\omega_{bw1}\omega_{bw2})^\eta}{(\omega_1\omega_2)^\eta(4\omega_1\omega_2)}\\&\times\Phi_\tau^{-(1)}(j(\omega_1-\omega_2))\Phi_T(j(\omega_2-\omega_1))\\&\times\left\{\mathcal{W}\left(d_{p,q}^B,\mathcal{H}_k^B\right)\times\mathcal{W}\left(d_{m,n}^M,\mathcal{H}_k^M\right)\right\}\\&+k^2\Phi_\tau^{(-1)}(j\omega_2)\Phi_\tau^{(-1)}(-j\omega_1)\Phi_T(-j\omega_2)\Phi_T(j\omega_1)\\&\times\Big\{\mathcal{W}\left(d_p^B,\mathcal{G}_{p,k}^B(\omega_1)\otimes\mathcal{F}_k^B\right)\\&\quad\times\mathcal{W}\left(d_q^B,\mathcal{G}_{q,-k}^{B*}(\omega_2)\otimes\mathcal{F}_k^B\right)\\&\quad\times\mathcal{W}\left(d_m^M,\mathcal{G}_{m,k}^M(\omega_1)\otimes\mathcal{F}_k^M\right)\\&\quad\times\mathcal{W}\left(d_n^M,\mathcal{G}_{n,-k}^{M*}(\omega_2)\otimes\mathcal{F}_k^M\right)\Big\}.\end{aligned}\tag{14}$$

We evaluate the CCF presented in (14) for the scenario, $i_1 = i_2 = i$, $l_1 = l_2 = l$, and $k^2 = 0$. The final expression of the CCF obtained in this scenario is presented in

$$\begin{aligned}&R_{pm,qn}(t_1,t_2,\omega_1,\omega_2)\\&=\frac{(\omega_{bw1}\omega_{bw2})^\eta}{(\omega_1\omega_2)^\eta(4\omega_1\omega_2)}\\&\times\Phi_\tau^{-(1)}(j(\omega_2-\omega_1))\Phi_T(j(\omega_2-\omega_1))\\&\times\mathcal{W}\left(d_{pq}^B,\mathcal{G}_{p,k}^B(\omega_1)\otimes\mathcal{G}_{q,-k}^{B*}(\omega_2)\otimes\mathcal{F}_k^B\right)\\&\times\mathcal{W}\left(d_{mn}^M,\mathcal{G}_{m,k}^M(\omega_1)\otimes\mathcal{G}_{n,-k}^{M*}(\omega_2)\otimes\mathcal{F}_k^M\right),\end{aligned}\tag{15}$$

where

$$\begin{aligned}\mathcal{W}(d,\mathcal{H}_k)&\triangleq 2\pi\sum_{k=-\infty}^{\infty}j^k e^{jk\angle d}\mathcal{H}_k(\omega)J_k\left(\frac{|d|}{c}\right),\\\mathcal{H}_k&=\mathcal{G}_k(\omega_1)\otimes\mathcal{G}_{-k}^*(\omega_2)\otimes\mathcal{F}_k.\end{aligned}\tag{16}$$

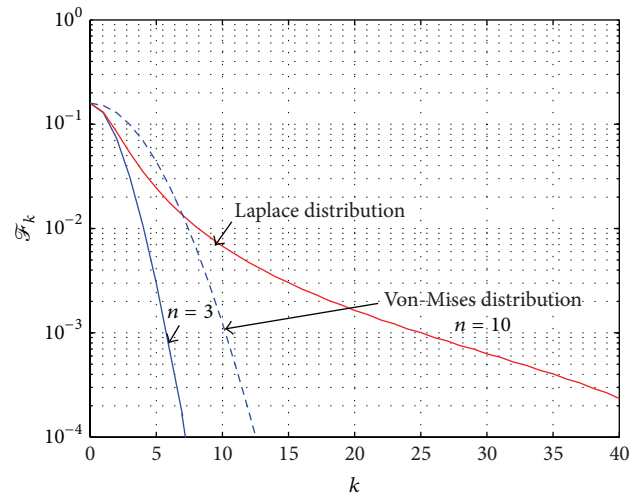

Figure 1: Fourier series coefficients for two AAS PDFs, to approximate Laplace and von-Mises distributions (with orders of nonisotropy $n = 3, 10$) determined to correspond to the real PDFs for the nonisotropic propagation environment.

The CCF appeared to be the convolution of two categories of FSCs as follows.

(i) $\mathcal{F}_k^{(\cdot)}$ are the kth FSCs of PDFs of the nonisotropic AAS at both MS and BS sides. This means that the CCF is represented as the same linear combination of FSCs associated with these PDFs. This allows accurate modeling for various 2D wireless propagation environments. In our model, we determined the necessary number of FSCs by calculating integral (2) for each of the two PDFs that describe the nonisotropic propagation environment. In Figure 1 the FSCs of Laplace and von-Mises PDFs (at the MS) are compared. For the von-Mises distribution, FSCs are presented when the propagation environment has two different orders of nonisotropy.

(ii) $\mathcal{G}_{(\cdot,k)}^{(\cdot)}$ are the kth FSCs of 2D WB/UWB APPs, at both BS and MS sides, used to investigate the impact of directional and omnidirectional antennas. At this point we differentiate the WB APP which is not frequency selective from the frequency selective UWB APPs.

3.1. CCF Numerical Evaluation. Low correlation between received signals is a necessary condition for good MIMO performances. This low correlation is achieved when each antenna provides a unique weighting for each l cluster with I multipath components. In order to achieve space diversity with MIMO systems, the antennas need to be as compact as possible but also to be able to recover signals with dissimilar multipath fading. An optimal solution may be a low threshold for correlation rather than zero correlation between antennas. Low correlation is often considered when CCF < 0.7 [25]. Correlation values are especially significant in applications where the evaluation of the channel capacity is necessary.

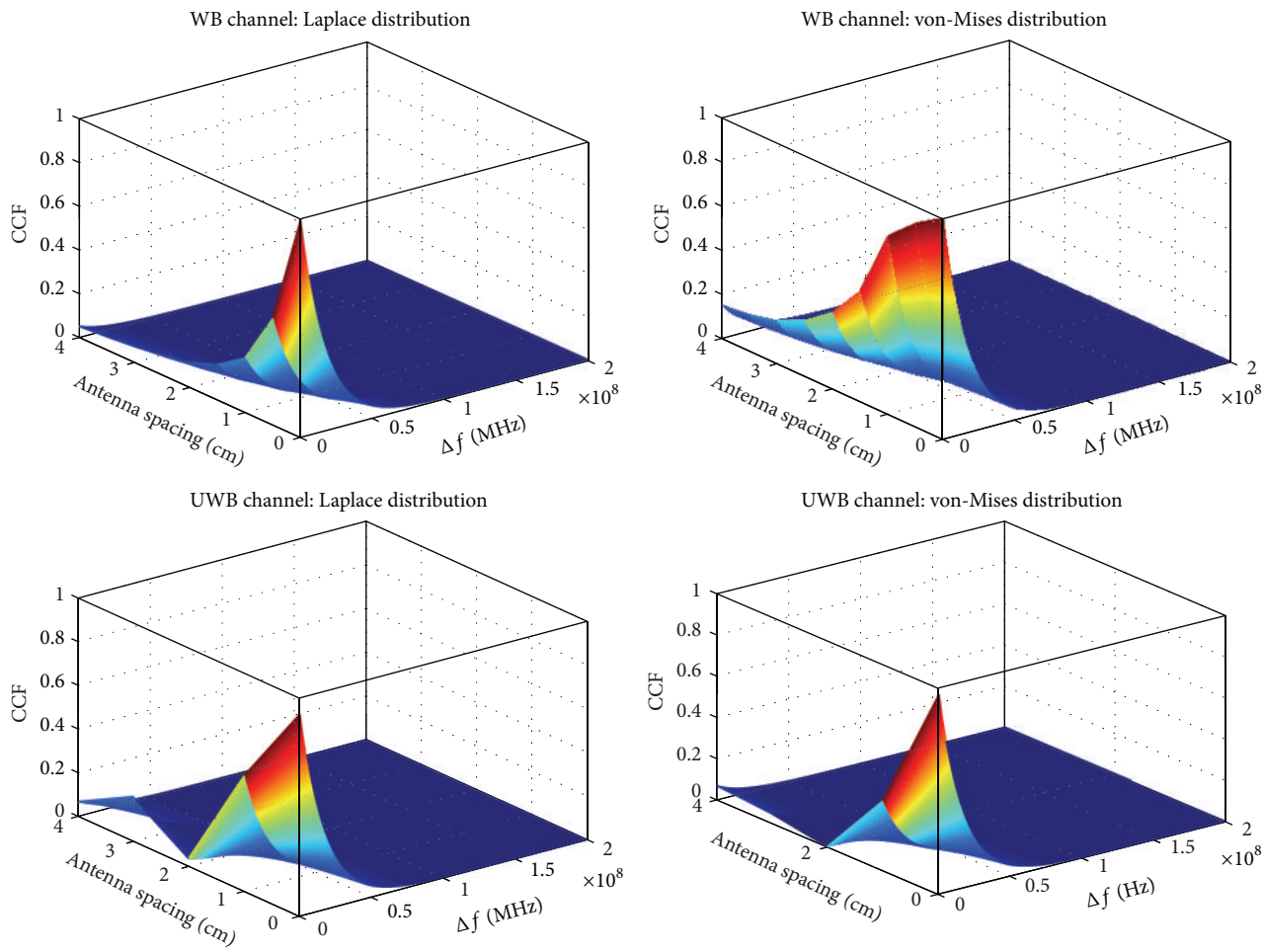

Figure 2: CCF corresponding to WB and UWB signals with omnidirectional APP, Laplace, and von-Mises PDFs of the propagation environment, with antenna spacing $\lambda/2 = c\pi/\omega_H$ and frequency offsets $\Delta f = f_2 - f_1$.

Figures 2 and 3 depict the effect of the distribution of the nonisotropic propagation environment, the APP (directional, omnidirectional), the antenna spacing, and the carrier frequency offset, $\Delta f = f_2 - f_1$ (where f_1 is constant at 5 GHz for WB channels and at 3.1 GHz for UWB channels) on the normalized CCF$|R(t_1, t_2, \omega_1, \omega_2)|^2/|R(t_1, t_1, \omega_1, \omega_1)|^2$. In the reported figures, the unit for the antenna spacing is half of the highest frequency of the signal bandwidth, $\lambda/2 = c\pi/\omega_H$, where $\omega_H = 2\pi f_H$.

In [22, page 26] measurement results for spatial correlation of UWB MIMO channels with omnidirectional antennas are presented. The measured data show that the spatial correlation is a monotonously decreasing function of the antenna distance. A complete characterization of MIMO UWB channels correlations is provided in [34]. It was stated that, for about 4 cm antenna spacing, the correlation function follows a pattern of the first kind zeroth-order Bessel function with distance. It was also found that a value of 2 cm for antenna spacing is sufficient for CCF $\leq$ 0.5. In [35–37] it was stated that the CCF values are higher for directional antennas than for omnidirectional antennas. This is because their beamwidth limits the effective angular spread and their ability to capture multipath signals from all directions. The results, regarding the spatial correlation, presented in Figures 2 and 3, are consistent with the CCF's behavior described in the mentioned references. In the reported figures the influence of the frequency correlation is also evaluated. It can be observed how CCF decreases as Δf increases. This decrease results not only from the Bessel functions (as the central frequencies appear in the Bessel operands) but also from the term produced by the MGF of the delay profile. As the figures show, the CCF is maximum when $\Delta f = 0$ and when there is no separation between the antennas of the MIMO system. CCF also decreases when WB APP is replaced by UWB APP. This is because UWB signals offer a higher degree of diversity owing to their abundant multipaths. In Figure 1 it can be observed that the number of FSCs necessary to approximate Laplace PDF is larger than the number of FSCs necessary to approximate von-Mises distribution. This indicates that a propagation environment described by Laplace PDF is characterized by a higher order of nonisotropy which provides better diversity and lower correlation between MIMO subchannels. The graphical representations of CCF show that the correlation decreases faster when the environment has

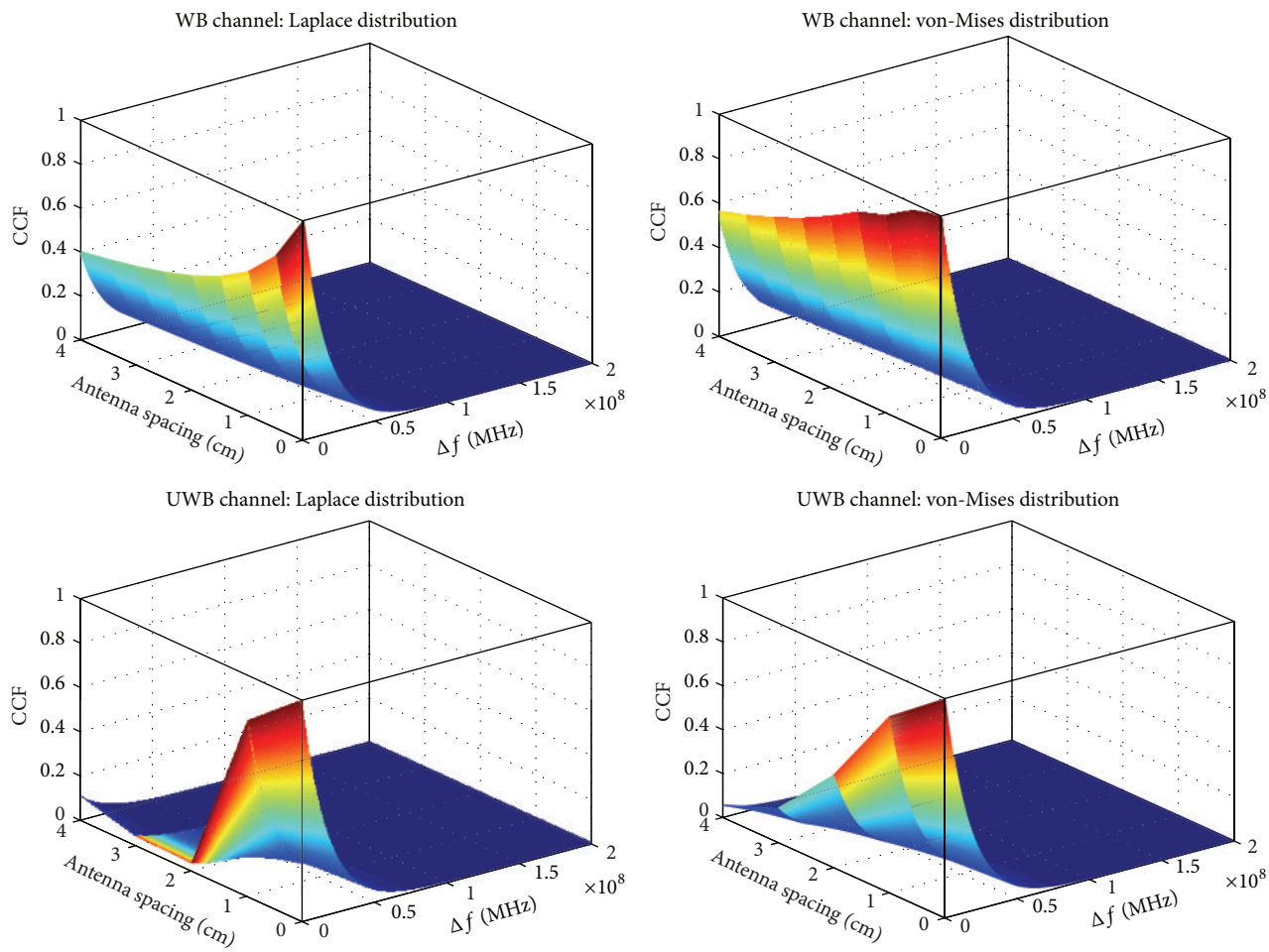

Figure 3: CCF corresponding to WB and UWB signals with directional APP, Laplace, and von-Mises PDFs of the propagation environment, with antenna spacing $\lambda/2 = c\pi/\omega_H$ and frequency offsets $\Delta f = f_2 - f_1$.

Laplacian distribution, for both WB and UWB channels. In [38] the influence of parameters like antenna element spacings, environment parameters, and scattering density, on the spatial correlation properties of multilink MIMO channels, was presented. Based on different propagation phenomena like those previously mentioned new key technical issues in developing and realizing multiinput multioutput technology were presented in [39].

4. Fourier Analysis of the 2D STF-CCF of WB/UWB MIMO Channels

The derived CCF can be used to analyze the power spectral density (PSD) of WB and UWB MIMO channels. PSD gives the distribution of the signal power among various frequencies and also reveals the presence or the absence of repetitive patterns and correlation sequences in the signal process. These structural patterns are useful in a wide range of applications like data forecasting, signal detection and coding, pattern recognition, and radar and decision-making systems. The analyzed PSD corresponds to a multiple-input single-output (MISO) channel which is a particular case of MIMO channel. This analysis corresponds to the stationary scenario when $\omega_1 = \omega_2 = \omega$ and $m = n = 1$. Considering $\angle d_{1,1}^M = \angle V + \angle(t_2 - t_1)$ we get

$$\begin{aligned} R_{p1,q1}(t_1, t_2, \omega, \omega) &= \pi \frac{\omega_{bw}^{2\eta}}{2\omega^{2\eta+2}} \mathscr{W}\left(d_{p,q}^B, \mathscr{H}_k^B\right) \\ &\quad \times \sum_{k=-\infty}^{\infty} j^k e^{jk\angle V} \left(\mathscr{G}_{1,k}^M(\omega) \otimes \mathscr{G}_{1,-k}^{M*}(\omega) \otimes \mathscr{F}_k^M\right) \\ &\quad \times J_k\left(\frac{\omega(t_2 - t_1)|V|}{c}\right). \end{aligned} \tag{17}$$

Using the Fourier transform of $J_k(u)$, which is given by

$$\begin{aligned} J_k(\Lambda) \triangleq F[J_k(u)] &= \int_{-\infty}^{\infty} e^{-j\Lambda\xi} J_k(\xi)\, d\xi \\ &= \begin{cases} \left(2(-j)^k T_k(\Lambda)\right)/\sqrt{1-\Lambda^2}, & |\Lambda| < 1, \\ 0, & |\Lambda| \geqq 1, \end{cases} \end{aligned} \tag{18}$$

where $F[\cdot]$ denotes the Fourier transform and $T_k(\Lambda) \triangleq \cos[k\cos^{-1}(\Lambda)]$ is the kth-order Chebyshev polynomial

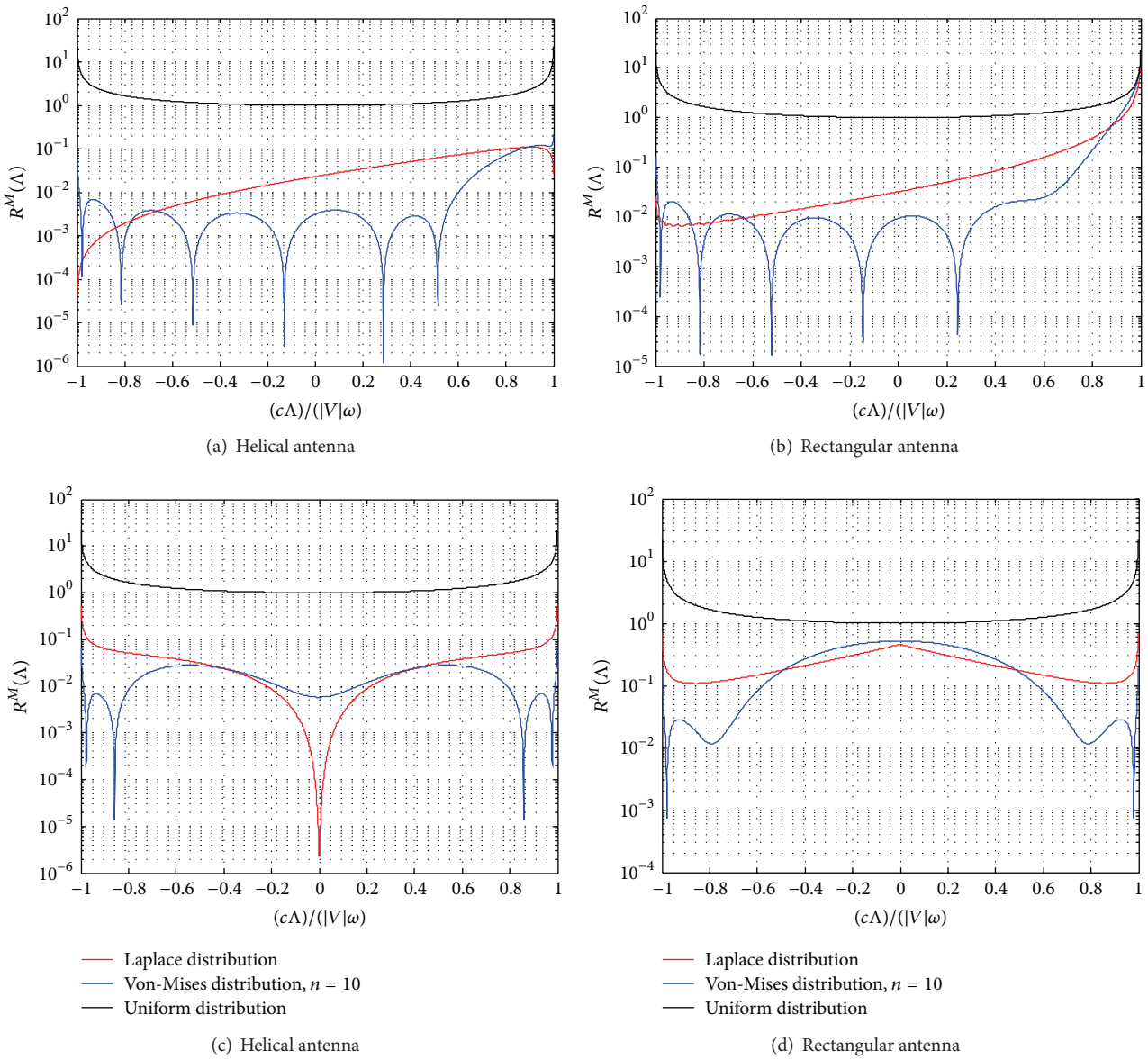

(a) Helical antenna (b) Rectangular antenna

(c) Helical antenna (d) Rectangular antenna

Figure 4: PSD of WB channels, MS moves in the positive direction of the x-axis ((a), (b)) and y-axis ((c), (d)), two antenna types employed at the MS, nonisotropic propagation (Laplacian or von-Mises distributed), and isotropic environment (uniformly distributed).

function of the first kind [[16], page 486], the Fourier transform of the CCF derived for stationary case versus the time-difference index, $\Delta t \triangleq t_2 - t_1$, results in the following equation:

$$\begin{aligned} R_{p1,q1}(\Lambda,\omega) &\triangleq \int_{-\infty}^{\infty} e^{-j\Lambda\Delta t} R_{1p,1q}(t_1,t_2,\omega,\omega)\, d\Delta t \\ &= \frac{\omega_{bw}^{2\eta}}{2\omega^{2\eta+2}} \mathscr{W}\left(d_{q,p}^{M}, \mathscr{H}_k^B\right) \frac{\pi c}{|V|} \\ &\quad \times \sum_{k=-\infty}^{\infty} \left[\left(e^{jk\angle V} \mathscr{G}_{1,k}^{M}(\omega) \otimes \mathscr{G}_{1,-k}^{M*}(\omega) \otimes \mathscr{F}_k^M\right) C_k\right], \end{aligned} \tag{19}$$

where $\mathscr{H}_k^B \triangleq \mathscr{G}_{p,k}^B(\omega) \otimes \mathscr{G}_{q,-k}^{B*}(\omega) \otimes \mathscr{F}_k^B$ and Λ is a frequency variable in the interval $-(\omega/c)|V| < \Lambda < (\omega/c)|V|$. Note that $R_{p1,q1}(\Lambda,\omega) = 0$ for all $|\Lambda| \geqslant (\omega/c)|V|$. We denote $C_k = (T_k(c\Lambda/|V|\omega))/\sqrt{1-(c\Lambda/|V|\omega)^2}$; $T_k(\cdot)$ is the Chebyshev polynomials which form a complete orthogonal set on the interval $-1 \leqslant u < 1$, with respect to the weighting function $1/\sqrt{1-u^2}$.

Therefore, any bandlimited CCF (in the interval $-(\omega/c)|V| \leqslant \Lambda \leqslant (\omega/c)|V|$) can be expanded in terms of Chebyshev polynomials as shown in (19). The PSD, $R^M(\Lambda)$, is the last term in (19) and shows the channel variations caused around or by the MS speed and direction and the impact of

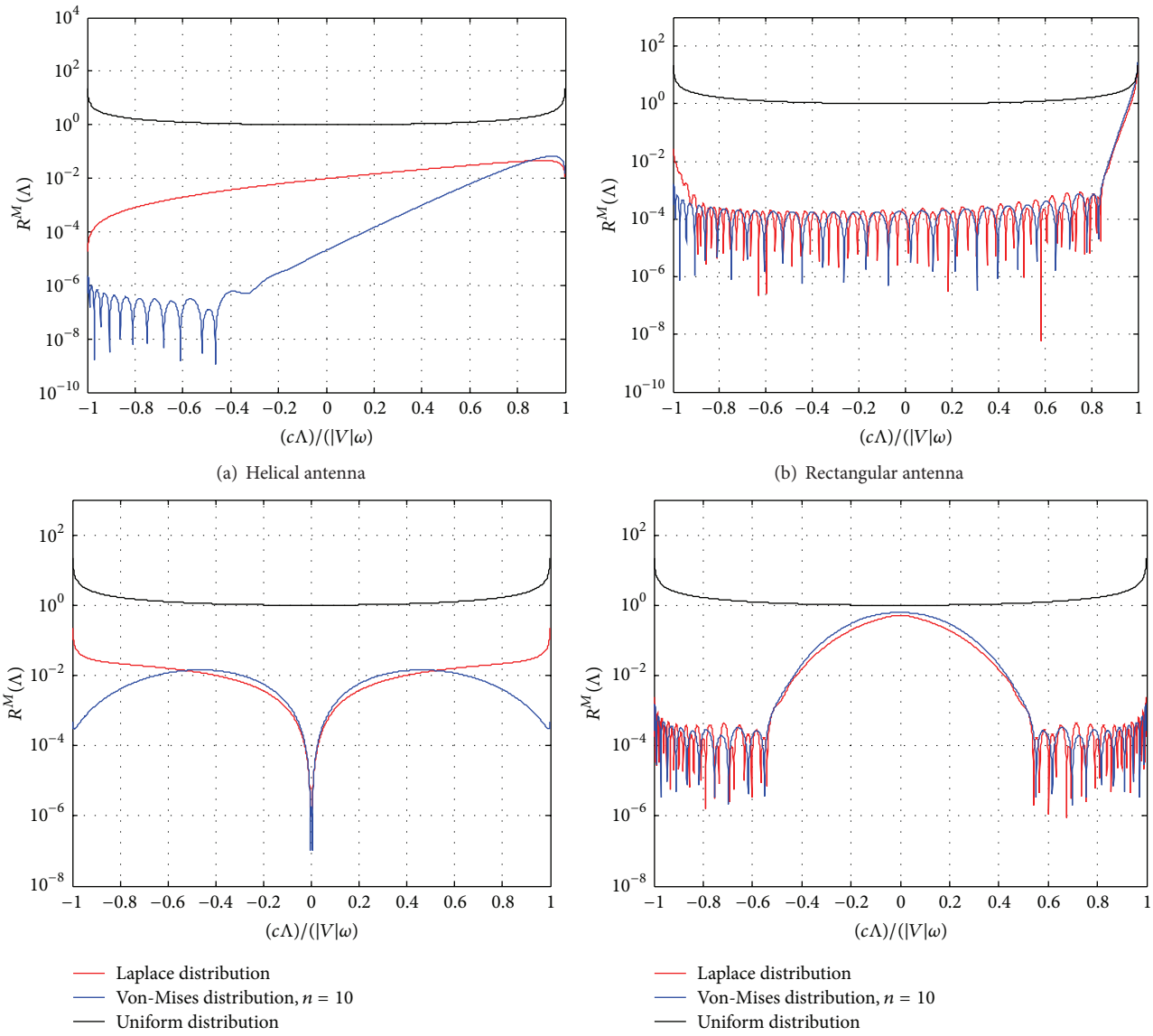

(a) Helical antenna

(b) Rectangular antenna

(c) Helical antenna

(d) Rectangular antenna

Figure 5: PSD of UWB channels, MS moves in the positive direction of the x-axis ((a), (b)) and y-axis ((c), (d)), two antenna types employed at the MS, nonisotropic propagation (Laplacian or von-Mises distributed), and isotropic environment (uniformly distributed).

the nonisotropic environment, of the channel bandwidth, and of the APP:

$$R^M(\Lambda) \triangleq \sum_{k=-\infty}^{\infty} e^{jk\angle V} \left(\mathcal{G}_{1,k}^M(\omega) \otimes \mathcal{G}_{1,-k}^{M*}(\omega) \otimes \mathcal{F}_k^M\right) C_k. \quad (20)$$

In Figures 4 and 5, the PSD of WB and UWB signals is depicted. The presented results illustrate (20) with the influence of the following elements.

(i) The channel bandwidth for WB channels was equal to 200 MHz with the central frequency $f = 2.5$ GHz. For UWB channels the results correspond to a bandwidth delimited by $3.1 \div 10.6$ GHz,

(ii) APPs, specific to WB and UWB systems, employed at the MS side (directional and omnidirectional antennas),

(iii) nonisotropic propagation environment around the MS (Laplace and von-Mises PDFs),

(iv) direction of the MS speed, the positive x-axis or y-axis direction.

From the comparative analysis of PSD obtained for WB and UWB channels relevant conclusions can be drawn regarding its distribution in the interval $-(\omega/c)|V| < \Lambda < (\omega/c)|V|$ as follows.

(i) The PSD fluctuations are more pronounced in the case of UWB channels compared to WB channels. This is

the effect of the frequency selectivity phenomenon whose effects increase with signal frequency and bandwidth. The noticeable increase of frequency selectivity that occurs in the case of UWB channels clearly differentiated them from other channels with narrower bandwidth. This characteristic may be helpful in the identification process of the channel's type for its bandwidth from its PSD only. In Figures 4(a), 4(b), 5(a), and 5(b) it can be observed that MS movement in the positive direction of the x-axis produces a PSD with larger values at positive Λ than at negative Λ. This asymmetry of the PSD is also determined by the Doppler spectrum which concentrates towards positive frequency axis.

(ii) The PSD shape is asymmetrical (Figures 4(a), 4(b), 5(a), and 5(b)) or symmetrical (Figures 4(c), 4(d), 5(c), and 5(d)) as a consequence of the interaction between the beam of the antenna pattern, the direction of the MS speed, and the distribution of the propagation directions around the MS. Figures 4(c), 4(d), 5(c), and 5(d) depict the shape of the PSD which is symmetrically distributed around $\Lambda = 0$, because the PDF which characterizes the nonisotropic propagation and the APPs are symmetrical around $\Theta^M = 0$ and are perpendicular towards the speed direction. For both WB and UWB channels, the maximum Doppler shift is $(\omega/c)|V|$ (i.e., $R^M(\Lambda) = 0$, if $|\Lambda| \geqslant (\omega/c)|V|$).

The obtained results are consistent with those proposed in [19, 37]. In [19] the PSD of a narrowband channel in nonisotropic propagation environment is similar to the PSD shape we obtained for WB channels. Between our results and those presented in [38] there are similarities regarding the U-shape of the PSD but there are also differences determined by parameters specific to channels with large bandwidths, like frequency selectivity, higher central frequency, and APPs typically used for this type of systems. Comparing the PSD shape obtained for WB channels with the PSD obtained for UWB channels and even with the PSD obtained for narrowband channels in [19] we can conclude that the channel bandwidth has a great influence on the channel power spectrum. With the increase of signal bandwidth larger variations can be observed over (because of the increased frequency selectivity) the PSD of UWB channels.

5. Conclusion

In this paper we proposed an outdoor channel model for WB/UWB MIMO systems, with moving receiver, based on the mathematical expression of a 2D STF-CCF. The impact of channel bandwidth, nonisotropic propagation, and omnidirectional and directional antennas on the CCF was evaluated. The increase of the channel bandwidth (from WB to UWB) generated the necessity to develop two approaches for the APPs calculation. The derived CCF appeared to be a combination of linear series expansion of Bessel functions. The coefficients of the CCF expansion are represented by the convolution of the Fourier coefficients of the APPs and the AASs specific to WB and UWB channels. The Fourier transform of the CCF in a stationary scenario showed that the PSD diverges from the U-shaped function, that is, Clarke/Jake model. This deviation depends on the AAS, the employed antennas, and the MS speed direction. The increase of the channel bandwidth also generated a more frequency selective PSD for UWB channels compared to the PSD of WB channels. This information can be useful for applications of signal detection and recognition since the increased frequency selectivity makes the identification of the channel's type for its bandwidth from its PSD only possible.

Conflict of Interests

The authors declare that there is no conflict of interests regarding the publication of this paper.

Acknowledgments

This paper has been financially supported within the Project entitled "Horizon 2020: Doctoral and Postdoctoral Studies—Promoting the National Interest through Excellence, Competitiveness and Responsibility in the Field of Romanian Fundamental and Applied Scientific Research," Contract number POSDRU/159/1.5/S/140106. This project is cofinanced by the European Social Fund through Sectoral Operational Programme for Human Resources Development 2007–2013, "Investing in People!"

References

[1] Y. Ma and M. Pätzold, "Wideband two-ring MIMO channel models for mobile-to-mobile communications," in *Proceedings of 10th International Symposium on Wireless Personal Communications*, pp. 380–384, Jaipur, India, December 2007.

[2] K. Witrisal and M. Pausini, "Statistical analysis of UWB channel correlation functions," *IEEE Transactions on Vehicular Technology*, vol. 57, no. 3, pp. 1359–1373, 2008.

[3] N. Gvozdenovic and M. Eric, "Localization of users in multiuser MB OFDM UWB systems based on TDOA principle," in *Proceedings of the 19th Telecommunications Forum (TELFOR '11)*, pp. 326–329, Belgrad, Serbia, November 2011.

[4] Q. Zou, A. Tarighat, and A. H. Sayed, "Performance analysis of multiband-OFDM UWB communications with application to range improvement," *IEEE Transactions on Vehicular Technology*, vol. 56, no. 6, pp. 3864–3878, 2007.

[5] A. Abdi and M. Kaveh, "A space-time correlation model for multielement antenna systems in mobile fading channels," *IEEE Journal on Selected Areas in Communications*, vol. 20, no. 3, pp. 550–560, 2002.

[6] T. Santos, J. Karedal, P. Almers, F. Tufvesson, and A. F. Molisch, "Modeling the ultra-wideband outdoor channel: measurements and parameter extraction method," *IEEE Transactions on Wireless Communications*, vol. 9, no. 1, pp. 282–290, 2010.

[7] M. Di Renzo, F. Graziosi, R. Minutolo, M. Montanari, and F. Santucci, "The ultra-wide bandwidth outdoor channel: from measurement campaign to statistical modelling," *Mobile Networks and Applications*, vol. 11, no. 4, pp. 451–467, 2006.

[8] C. F. Souza and J. C. R. Dal Bello, "UWB signals transmission in outdoor environments for emergency communications,"

in *Proceedings of the 11th IEEE International Conference on Computational Science and Engineering Workshops*, pp. 343–348, San-Paolo, Italy, July 2008.

[9] Y. Wang, X. Yu, Y. Zhang et al., "Using wavelet entropy to distinguish between humans and dogs detected by UWB radar," *Progress in Electromagnetics Research*, vol. 139, pp. 335–352, 2013.

[10] W. Zhou, J. T. Wang, H. W. Chen, and X. Li, "Signal model and moving target detection based on MIMO synthetic aperture radar," *Progress in Electromagnetics Research*, vol. 131, pp. 311–329, 2012.

[11] A. E. Waadt, S. Wang, C. Kocks et al., "Positioning in multiband OFDM UWB utilizing received signal strength," in *Proceedings of the 7th Workshop on Positioning, Navigation and Communication (WPNC '10)*, pp. 308–312, March 2010.

[12] W. Z. Li, Z. Li, H. Lv et al., "A new method for non-line-of-sight vital sign monitoring based on developed adaptive line enhancer using low centre frequency UWB radar," *Progress in Electromagnetics Research*, vol. 133, pp. 535–554, 2013.

[13] I. C. Vizitiu, *Fundamentals of Electronic Warfare*, Matrix Rom Publishing House, 2011.

[14] K. Mizui, M. Uchida, and M. Nakagawa, "Vehicle-to-vehicle communication and ranging system using spread spectrum technique (Proposal of Boomerang Transmission System)," in *Proceedings of the 43rd IEEE Vehicular Technology Conference*, pp. 335–338, Secaucus, NJ, USA, May 1993.

[15] C. Sturm and W. Wiesbeck, "Waveform design and signal processing aspects for fusion of wireless communications and radar sensing," *Proceedings of the IEEE*, vol. 99, no. 7, pp. 1236–1259, 2011.

[16] B. J. Donnet and I. D. Longstaff, "Combining MIMO radar with OFDM communications," in *Proceedings of the 3rd European Radar Conference (EuRAD '03)*, pp. 37–40, September 2006.

[17] CEPT Report 34: Report B from CEPT to European Commission in response to the Mandate 4 on Ultra-Wideband (UWB), 2009.

[18] European Communications Office, "Specific UWB applications in the bands 3.4–4.8 GHz and 6–8.5 GHz location tracking applications for emergency services (LAES), location tracking aplications 2 (LT2) and location tracking and sensors applications for automotive and transportation environments (LTA)," ECC Report 170, 2011.

[19] H. S. Rad and S. Gazor, "The impact of non-isotropic scattering and directional antennas on MIMO multicarrier mobile communication channels," *IEEE Transactions on Communications*, vol. 56, no. 4, pp. 642–652, 2008.

[20] A. M. Pistea and H. Saligheh Rad, "Three dimensional space-time-frequency description of WB and UWB MIMO channels," *IEEE Communications Letters*, vol. 16, no. 2, pp. 205–207, 2012.

[21] A. M. Pistea, T. Palade, A. Moldovan, and H. S. Rad, "The impact of antenna directivity and channel bandwidth on the power spectral density of wideband and UWB MISO channels," in *Proceedings of the 7th International Conference on Wireless and Mobile Communications (ICWMC '11)*, pp. 36–41, Luxembourg City, Luxembourg, June 2011.

[22] C. A. Balanis, *Antenna Theory: Analysis and Design*, John Wiley & Sons, 2nd edition, 1996.

[23] M. Ghavami, L. B. Michael, and R. Kohno, *Ultra Wideband Signals and Systems in Communication Engineering*, John Wiley & Sons, 2004.

[24] A. F. Molisch, K. Balakrishnan, D. Cassioli et al., "IEEE 802.15.4a channel model—final report," Technical Report Document IEEE 802.15-04-0662-02-004a, 2005.

[25] T. Kaiser and F. Zheng, *Ultra-Wideband Systems with MIMO*, John Wiley & Sons, 2010.

[26] A. Abdi, J. A. Barger, and M. Kaveh, "A parametric model for the distribution of the angle of arrival and the associated correlation function and power spectrum at the mobile station," *IEEE Transactions on Vehicular Technology*, vol. 51, no. 3, pp. 425–434, 2002.

[27] J. Ren and R. G. Vaughan, "Spaced antenna design in directional scenarios using the von mises distribution," in *Proceedings of the 70th IEEE Vehicular Technology Conference (VTC '09)*, pp. 1–5, Anchorage, Alaska, USA, September 2009.

[28] Q. Spencer, M. Rice, B. Jeffs, and M. Jensen, "A statistical model for angle of arrival in indoor multipath propagation," in *Proceedings of the 47th IEEE Vehicular Technology Conference*, vol. 3, pp. 1415–1419, Phoenix, Ariz, USA, May 1997.

[29] R. C. Qiu and I.-T. Lu, "Wideband wireless multipath channel modeling with path frequency dependence," in *IEEE International Conference on Communications (ICC '96), Conference Record, Converging Technologies for Tomorrow's Applications*, vol. 1, pp. 277–281, Dallas, Tex, USA, June 1996.

[30] J. P. M. de Sá, *Applied Statistics Using SPSS, STATISTICA, MATLAB and R*, Springer, 2003.

[31] J. Wallace, *Characterization and identification of ultrawideband radio propagation channels [Ph.D. thesis]*, Faculty of the Graduate School, University of Southern California, 2005.

[32] A. F. Molisch, "Ultrawideband propagation channels-theory, measurement, and modeling," *IEEE Transactions on Vehicular Technology*, vol. 54, no. 5, pp. 1528–1545, 2005.

[33] M. C. Jeruchim, P. Balaban, and K. S. Shanmugan, *Simulation of Communication Systems*, Applications of Communications Theory, Plenum Press, New York, NY, USA, 1992.

[34] W. Q. Malik, "Spatial correlation in ultrawideband channels," *IEEE Transactions on Wireless Communications*, vol. 7, no. 2, pp. 604–610, 2008.

[35] D. Gesbert, H. Bölcskei, D. A. Gore, and A. J. Paulraj, "Outdoor MIMO wireless channels: models and performance prediction," *IEEE Transactions on Communications*, vol. 50, no. 12, pp. 1926–1934, 2002.

[36] P. Jin, N. A. Goodman, and K. L. Melde, "Exploiting directional antennas for reduced-dimension space-time RAKE receiving," *IEEE Transactions on Vehicular Technology*, vol. 57, no. 6, pp. 3880–3885, 2008.

[37] C. R. Anderson, "Low-antenna ultra wideband spatial correlation analysis in a forest environment," in *Proceedings of the Vehicular Technology Conference*, pp. 1–5, Barcelona, Spain, 2009.

[38] X. Cheng, C.-X. Wang, H. Wang et al., "Cooperative MIMO channel modeling and multi-link spatial correlation properties," *IEEE Journal on Selected Areas in Communications*, vol. 30, no. 2, pp. 388–396, 2012.

[39] X. Cheng, B. Yu, L. Yang et al., "Communicating in the real world: 3D MIMO," *IEEE Wireless Communications Magazine*, vol. 21, no. 4, pp. 136–144, 2014.

Hindawi Publishing Corporation
International Journal of Antennas and Propagation
Volume 2015, Article ID 975139, 11 pages
http://dx.doi.org/10.1155/2015/975139

Research Article

Power Allocation Optimization: Linear Precoding Adapted to NB-LDPC Coded MIMO Transmission

Tarek Chehade,[1,2] Ludovic Collin,[1,2] Philippe Rostaing,[1,2] Emanuel Radoi,[1,2] and Oussama Bazzi[3]

[1] *Université Européenne de Bretagne, 5 Boulevard Laënnec, 35000 Rennes, France*
[2] *Université de Brest, CNRS, UMR 6285 Lab-STICC, 6 avenue Victor Le Gorgeu, CS 93837, 29238 Brest Cedex 3, France*
[3] *Department of Physics and Electronics, Faculty of Sciences I, Lebanese University, Hadath, Beirut, Lebanon*

Correspondence should be addressed to Tarek Chehade; tarek.chehade@univ-brest.fr

Received 19 September 2014; Revised 31 December 2014; Accepted 14 January 2015

Academic Editor: Yan Zhang

In multiple-input multiple-output (MIMO) transmission systems, the channel state information (CSI) at the transmitter can be used to add linear precoding to the transmitted signals in order to improve the performance and the reliability of the transmission system. This paper investigates how to properly join precoded closed-loop MIMO systems and nonbinary low density parity check (NB-LDPC). The q elements in the Galois field, GF(q), are directly mapped to q transmit symbol vectors. This allows NB-LDPC codes to perfectly fit with a MIMO precoding scheme, unlike binary LDPC codes. The new transmission model is detailed and studied for several linear precoders and various designed LDPC codes. We show that NB-LDPC codes are particularly well suited to be jointly used with precoding schemes based on the maximization of the minimum Euclidean distance (max-$d_{\min}$) criterion. These results are theoretically supported by extrinsic information transfer (EXIT) analysis and are confirmed by numerical simulations.

1. Introduction

Multiple-input multiple-output (MIMO) schemes have become unavoidable for transmission systems looking for increased throughput and improved reliability. Many methods have lately been developed to exploit the diversity offered by multiantenna systems like antenna distribution or space/polarization isolation [1], space-time block codes (e.g., Alamouti scheme) that do not require any channel state information at the transmitter side (Tx-CSI), or power allocation optimization techniques, also called precoding, that require a full or partial Tx-CSI. In this paper, we focus on NB-LDPC codes that are widely used because of their effectiveness. One advantage of NB-LDPC codes over binary LDPC codes is that nonbinary codes can match very well the underlying modulation, so symbol-to-bit conversion at the receiver can be avoided. The results in [2] confirm the advantages of using NB-LDPC codes to match the underlying high order modulations.

To the best of our knowledge, the MIMO linear precoding performances are typically evaluated for uncoded MIMO systems. In this paper, we examine the association of the precoding scheme with channel coding in order to finally determine a power allocation optimization solution that adapts a block of linear precoding to a NB-LDPC coded MIMO transmission, where the Belief Propagation algorithm is used for decoding.

We implement this new scheme using linear precoders, having diagonal or nondiagonal structure, and we study the impact of the application of different known precoders on two system configurations ((2, 2) and (2, 4) MIMO). We investigate, by means of an EXIT analysis, how to take advantage of the precoding techniques in a MIMO system that uses NB-LDPC codes and we show why some associations could be harmful and others beneficial.

The main contributions of this paper are listed as follows:

(i) a proposed scheme associating NB-LDPC codes to MIMO precoding systems with adequate correspondence between the GF(q) elements and the q received constellation points;

(ii) a comparison between different precoder types and a study of the gain/loss in the different cases;

(iii) a theoretical EXIT analysis in order to predict the performance of different precoders with the NB-LDPC codes;

(iv) a confirmation by numerical simulations, in terms of bit error rate (BER), of the performance of the proposed power allocation optimization scheme.

This paper is organized as follows. In Section 2 the system model is described with the eigenmode representation. LDPC codes are introduced in Section 3. Linear precoding techniques are presented in Section 4. Section 5 provides a detailed description of the new proposed scheme; Section 6 presents the EXIT analysis, while the simulation results are given in Section 7. Finally, some conclusions are drawn in Section 8.

The notations used in this paper are as follows. Matrices and vectors are denoted by symbols in boldface, and $(\cdot)^T$ and $(\cdot)^H$ represent complex transpose and Hermitian, respectively. $\mathbf{I}_m$ denotes the $m \times m$ identity matrix and diag($\mathbf{x}$) denotes a diagonal matrix with $\mathbf{x}$ on its main diagonal. $E[\cdot]$ denotes statistical expectation. $\mathbf{X}[i_1 : i_2, j_1 : j_2]$ denotes a submatrix obtained by extracting rows i_1 through i_2 and columns j_1 through j_2 from a matrix $\mathbf{X}$. If no specific range appears at the row or column position in notation, then all rows or columns are considered to constitute the submatrix. $[\mathbf{X}]^{ij}$ denotes the (i, j)th element of a matrix $\mathbf{X}$. $\|\mathbf{x}\|$ denotes the 2-norm of vector $\mathbf{x}$. $\|\mathbf{X}\|_F$ denotes the Frobenius norm of matrix $\mathbf{X}$ and $\mathcal{N}_{\mathbb{C}}(0, \sigma^2)$ denotes a circular symmetric complex Gaussian distribution with zero mean and variance σ^2.

2. System Model and Eigenmode Representation

Let us consider a MIMO system with n_T transmit antennas and n_R receive antennas; the received signal is therefore given by

$$\mathbf{y} = \mathbf{GAFs} + \mathbf{Gn}, \tag{1}$$

where $\mathbf{y}$ is the $b \times 1$ received symbol vector, $\mathbf{A}$ is the $n_R \times n_T$ channel matrix, $\mathbf{F}$ is the $n_T \times b$ linear precoding matrix, $\mathbf{G}$ is the $b \times n_R$ linear decoding matrix, $\mathbf{s}$ is the $b \times 1$ transmitted symbol vector, and $\mathbf{n}$ is $n_R \times 1$ complex additive white Gaussian noise vector with zero mean and covariance matrix $N_0 \mathbf{I}_{n_R}$. Let us assume that

$$E\left[\mathbf{ss}^H\right] = E_s \mathbf{I}_b, \qquad E\left[\mathbf{sn}^H\right] = 0, \qquad E\left[\mathbf{nn}^H\right] = N_0 \mathbf{I}_{n_R}. \tag{2}$$

The average transmitted power is limited; the precoding matrix is normalized and is therefore subject to the power constraint:

$$\|\mathbf{F}\|_F^2 = 1. \tag{3}$$

All over the paper, the channel state information is assumed to be perfectly known at both transmitter and receiver sides. We apply a transformation in order to obtain a simplified model of the system. This will result in a diagonalized channel matrix [3]. Let us apply this virtual transformation, which is based on the singular value decomposition (SVD), by means of the following decompositions: $\mathbf{A} = \mathbf{UA}_v\mathbf{V}^H$, $\mathbf{F} = \mathbf{F}_v\mathbf{F}_d$, $\mathbf{G} = \mathbf{G}_v$, where $\mathbf{F}_v = \mathbf{V}(:, 1 : b)$ and $\mathbf{G}_v = \mathbf{U}^H(:, 1 : b)$.

Relation (1) can be then rewritten as

$$\mathbf{y} = \mathbf{A}_v\mathbf{F}_d\mathbf{s} + \mathbf{n}_v, \tag{4}$$

where $\mathbf{A}_v = \mathbf{G}_v\mathbf{AF}_v$ is the eigenchannel matrix, $\mathbf{n}_v = \mathbf{G}_v\mathbf{n}$ is the transformed additive noise vector with the covariance matrix $\mathbf{R}_{\mathbf{n}_v} = E[\mathbf{n}_v\mathbf{n}_v{}^H] = N_0\mathbf{I}_b$, and the unitary matrices $\mathbf{G}_v$ and $\mathbf{F}_v$ are chosen so as to ensure the whitening of the noise, the diagonalization of the channel, and the reduction of the dimension to b. The eigen-channel matrix $\mathbf{A}_v$ can now be expressed as

$$\mathbf{A}_v = \operatorname{diag}\left(\sigma_1, \sigma_2, \ldots, \sigma_b\right), \tag{5}$$

where the singular values are sorted in descending order.

3. Low Density Parity Check Codes

Low density parity check (LDPC) codes were proposed by Gallager in 1962 [4]. They are defined by a sparse parity check matrix over a Galois field GF(q), where q denotes the order of the Galois field. LDPC codes are binary when $q = 2$ and nonbinary when $q > 2$. Binary LDPC codes have been shown to approach Shannon limit performance [4–7] for very long code lengths. NB-LDPC codes are usually preferred to their binary counterparts when the block length is small to moderate [8] or when the order of the symbols sent through the channel is not binary [9], which is the case for high order modulations or for multiple-antennas channels [10, 11]. Davey and MacKay studied in 1998 NB-LDPC codes [12] and showed that they may achieve superior performance than the binary codes when constructed over higher order Galois fields at the expense of increased decoding complexity [12, 13].

A sparse parity check matrix $\mathbf{H}$ describes the LDPC code and can be efficiently represented by a bipartite graph called Tanner graph. Iterative decoding of LDPC codes has been addressed efficiently in [12, 14] using the Belief Propagation (BP) algorithm.

The BP algorithm is a suboptimal decoding algorithm proposed by Gallager in [4] for binary LDPC codes decoding and then generalized in [12] for the NB-LDPC codes. The iterative decoding is done by repeating the steps of the algorithm until a valid codeword has been obtained or a fixed number of iterations have been completed. Therefore, the rapidity of convergence of the algorithm appears to be an important issue.

One advantage of NB-LDPC coding is that one can match the field order with the constellation size. This way, one element in GF(q) is mapped to one point in the signal constellation. This is because the likelihood probabilities (or LLRV) for each coded symbol over GF(q) are independent of other coded symbols.

The LDPC codes we chose to use have the following properties.

(i) Ultrasparse NB-LDPC codes with column weight $d_v = 2$ at the variable-node side that gives large girths compared to classical binary graphs [8, 15].

(ii) These codes are well designed for both good waterfall and error floor properties [8, 15], compared to random choice of the Tanner graph structure and the nonzero values assignment.

(iii) At the check mode side, several row weights are chosen ($d_c = 4, 8$, and 12) to have precoding comparison at several code rates.

(iv) These codes are targeted for LTE-A with small packet lengths (small to moderate codeword lengths) [15].

(v) Small packet lengths are typically well suited for closed-loop MIMO systems.

4. Linear Precoding

The full knowledge of the channel state information at the transmitter side (Tx-CSI) permits the application of linear precoding operation in MIMO transmissions. It consists in a matrix multiplication operation that is applied to the transmitted signal which combines the symbols on the different antennas. This antenna allocation operation is determined and designed in such a way that allows the optimization of a well-defined criterion. Therefore, different linear precoders are defined because of the different optimization criteria. These precoders are mainly divided into two categories: diagonal precoders that allow transforming the MIMO transmission system into parallel independent SISO systems and nondiagonal precoders.

The precoders are detailed hereafter for the sake of presenting them on the same formalism, which facilitates the presentation of our proposed scheme and allows the comparison in terms of both EXIT analysis (Section 6) and numerical simulations (Section 7).

4.1. Diagonal Precoders. For diagonal precoders, the precoding matrix has the following expression:

$$\mathbf{F}_d = \operatorname{diag}\left(\sqrt{p_1}, \ldots, \sqrt{p_b}\right), \tag{6}$$

where p_i ($i = 1, \ldots, b$) represents the power allocation of the ith subchannel.

Knowing that the transformation of the channel model gives a diagonal channel $\mathbf{A}_v$ the use of a diagonal precoder will result in completely independent subchannels and the transmission system is therefore equivalent to distributing the symbols onto parallel independent subsystems.

The power constraint in this case is expressed as

$$\sum_{i=1}^{b} p_i = 1. \tag{7}$$

The main optimization criteria that lead to diagonal precoders are the maximization of the postprocessing SNR [16], the maximization of the channel capacity [17], the minimization of the BER [18], the minimization of the mean square error (MSE) [19], the maintaining of fixed ratios between the postprocessing SNR values of the different subchannels [19].

4.1.1. Max-SNR Precoder. Maximizing the postprocessing SNR leads to a transmission over one subchannel only, corresponding to the highest subchannel singular value σ_1. If we apply the power constraint, we obtain $p_1 = 1$ and $p_i = 0$ for $i = 2, \ldots, b$. The max-SNR solution simplifies the signal model equation that becomes

$$y = \sigma_1 s + n. \tag{8}$$

4.1.2. Water-Filling Precoder. The optimization criterion that maximizes the channel capacity leads to the Water-Filling (WF) precoder. The channel capacity can be expressed as

$$C = \sum_{i=1}^{b} \log_2\left(1 + \frac{E_s}{N_0} \times p_i \sigma_i^2\right) \tag{9}$$

with $E_s = E[|s|^2]$ and $N_0 = E[|n|^2]$.

We set

$$\tilde{\sigma}_i = \sigma_i \sqrt{\frac{E_s}{N_0}} \tag{10}$$

and then the maximization of C gives the following power allocation strategy:

$$p_i = \begin{cases} \Psi - \dfrac{1}{\tilde{\sigma}_i^2} & \text{if } \Psi > \dfrac{1}{\tilde{\sigma}_i^2} \\ 0 & \text{otherwise} \end{cases} \tag{11}$$

$$\text{for } i = 1, \ldots, b,$$

where the threshold Ψ is defined by

$$\Psi = \frac{1 + \gamma_\Psi}{b_\Psi}; \qquad \gamma_\Psi = \sum_{i=1}^{b_\Psi} \frac{1}{\tilde{\sigma}_i^2} \tag{12}$$

and $b_\Psi = i$ the greatest value in $\{1, \ldots, b\}$ such that $\Psi > 1/\tilde{\sigma}_i^2$.

The power allocation strategy of the WF precoder depends on the SNR values of the subchannels (i.e., $\tilde{\sigma}_i^2$ for $i = 1, 2, \ldots, b$). The precoder allows the cancellation of the most disadvantaged subchannels. The total average power is then distributed among the strongest b_Ψ subchannels.

In a (2, 2) MIMO system, this results in either transmitting over 2 subchannels or using only the most advantageous one. We will show later the switch of this precoder in function of the SNR values.

4.1.3. MMSE Precoder. The optimization criterion of the MMSE precoder is the minimization of the mean square error that is expressed as

$$\text{MSE} = E\left[\|\mathbf{y} - \mathbf{s}\|^2\right] = \sum_{i=1}^{b} E\left[\left|\left(\sigma_i \sqrt{p_i} - 1\right) s_i + n_i\right|^2\right] \tag{13}$$

and then the minimization of MSE gives the following power allocation strategy:

$$p_i = \begin{cases} \frac{1}{\tilde{\sigma}_i}\left(\Psi_{\text{MMSE}} - \frac{1}{\tilde{\sigma}_i}\right) & \text{if } \Psi_{\text{MMSE}} > \frac{1}{\tilde{\sigma}_i} \\ 0 & \text{otherwise} \end{cases} \quad \text{for } i = 1, \ldots, b, \tag{14}$$

where the threshold Ψ_{MMSE} is defined by

$$\Psi_{\text{MMSE}} = \frac{1 + \gamma_{\Psi_{\text{MMSE}}}}{\sum_{i=1}^{b_{\Psi_{\text{MMSE}}}} \left(1/\tilde{\sigma}_i\right)}; \qquad \gamma_{\Psi_{\text{MMSE}}} = \sum_{i=1}^{b_{\Psi_{\text{MMSE}}}} \frac{1}{\tilde{\sigma}_i^2}. \tag{15}$$

The power allocation strategy of the MMSE precoder depends on the SNR values of the subchannels also and may lead to subchannel cancellation; that is, $b_{\Psi_{\text{MMSE}}}$ subchannels are used (in the case of $b = 2$, only one subchannel is used).

4.1.4. Quality of Service and Equal Error Precoders. The power allocation strategy of the Quality of Service (QoS) precoder aims to maintain fixed ratios between the postprocessing SNR values of the different subchannels [19], which are expressed as

$$\gamma_i = p_i \tilde{\sigma}_i^2 = \frac{w_i}{\sum_{k=1}^{b} w_k/\tilde{\sigma}_k^2} \quad \text{for } i = 1, \ldots, b, \tag{16}$$

where $w_1 = 1 > w_2 > \cdots > w_b$ are the fixed SNR ratios between subchannel $i \neq 1$ and subchannel 1 (i.e., $w_i = \gamma_i/\gamma_1$).

The Equal Error (EE) precoder is the particular case of the QoS precoder where all subchannels have the same postprocessing SNR value γ_i by setting $w_1 = w_2 = \cdots = w_b = 1$.

4.2. Nondiagonal Precoders. Unlike diagonal precoders, the precoding matrix of nondiagonal precoders is a nondiagonal matrix. In our study, we focus on two of the best performing nondiagonal precoders which are based on the minimal Euclidean distance criterion: the max-$d_{\min}$ precoder [3] and the max-$d_{\min}$-DFT precoder (Discrete Fourier Transform) [20].

4.2.1. Max-$d_{\min}$. The minimum Euclidean distance between signal points on the receiver's constellation affects the system performances, especially with the ML detector [21]. The max-$d_{\min}$ precoder is designed with the criterion of maximizing this minimal Euclidean distance $d_{\min}$ which is expressed as

$$d_{\min} = \min_{\boldsymbol{\epsilon} \in \mathscr{E}} \left\| \mathbf{A}_v \mathbf{F}_d \boldsymbol{\epsilon} \right\|, \tag{17}$$

where $\boldsymbol{\epsilon} = \mathbf{s}_k - \mathbf{s}_l$ is the error vector between vector symbols $\mathbf{s}_k$ and $\mathbf{s}_l$ for $k \neq l$, $\mathscr{E}$ being the set of all error vectors. The max-$d_{\min}$ precoder can then be obtained by solving

$$\mathbf{F}_d^{d_{\min}} = \underset{\mathbf{F}_d}{\operatorname{argmax}}\, d_{\min}\left(\mathbf{F}_d\right) \tag{18}$$

under the power constraint $\|\mathbf{F}_d\|_F^2 = 1$.

Collin et al. give in [3] a solution for (17) for the case of $b = 2$ and a 4-QAM modulation. For two data streams, the precoding matrix is written as

$$\mathbf{F}_d = \begin{pmatrix} \cos\psi & 0 \\ 0 & \sin\psi \end{pmatrix} \begin{pmatrix} \cos\theta & \sin\theta \\ -\sin\theta & \cos\theta \end{pmatrix} \begin{pmatrix} 1 & 0 \\ 0 & e^{j\phi} \end{pmatrix} \tag{19}$$

and the channel matrix is written as

$$\mathbf{A}_v = \rho \begin{pmatrix} \cos\gamma & 0 \\ 0 & \sin\gamma \end{pmatrix}, \tag{20}$$

where $\rho^2 = \sigma_1^2 + \sigma_2^2$ and $\tan\gamma = \sigma_2/\sigma_1$.

For 4-QAM modulation, the values of the triplet (ψ, θ, ϕ) that maximizes $d_{\min}$ depend on the parameter γ, and two cases are possible:

(i) if $\gamma < \gamma_0$, we have

$$\psi = 0, \quad \theta = \operatorname{atan}\left(\frac{2}{\left(\sqrt{6} + \sqrt{2}\right)}\right), \quad \phi = 15^\circ; \tag{21}$$

(ii) if $\gamma \geq \gamma_0$, we have

$$\psi = \operatorname{atan}\left(\frac{\left(\sqrt{2} - 1\right)}{\tan\gamma}\right), \quad \theta = 45^\circ, \quad \phi = 45^\circ \tag{22}$$

with $\gamma_0 \approx 17.28^\circ$.

4.2.2. Max-$d_{\min}$-DFT. The general form of this precoder can be written as

$$\mathbf{F}_d = \operatorname{diag}\left(\sqrt{p_1}, \ldots, \sqrt{p_b}\right) W_b, \tag{23}$$

where W_b is the DFT matrix defined as

$$W_b = \left(w^{kl}\right)_{k,l=0,\ldots,b-1} \tag{24}$$

with $w = e^{j2\pi/b}$.

For $b = 2$, the DFT matrix is written as

$$W_2 = \begin{pmatrix} 1 & 1 \\ 1 & -1 \end{pmatrix}. \tag{25}$$

The power allocation strategy aims to optimize the minimal Euclidean distance $d_{\min}$, which leads to a switch to the max-SNR solution at $\gamma_{\text{DFT}} = \operatorname{atan}(1/\sqrt{7}) = 20.70^\circ$.

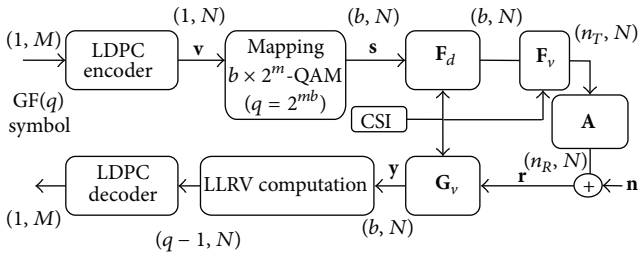

Figure 1: Proposed block diagram scheme.

For $\gamma < \gamma_{\mathrm{DFT}}$, the max-SNR precoder is used, while for $\gamma > \gamma_{\mathrm{DFT}}$, considering the form expressed in (19), we obtain the following triplet values:

$$\begin{aligned} \psi &= \operatorname{atan}\left(\frac{1}{\left(\sqrt{3}\tan\gamma\right)}\right), \\ \theta &= 45^{\circ} \\ \phi &= 0. \end{aligned} \tag{26}$$

5. Proposed Scheme

The block diagram of the proposed scheme is detailed in Figure 1. A sparse parity check matrix $\mathbf{H}$ of dimension $(M \times N)$ whose elements are in the Galois field GF(q) defines the LDPC code, with $M = N - K$, where K and N are, respectively, the source block length and the transmitted code block length. Data stream is encoded through the LDPC encoder into the codeword $\mathbf{v}$ and then mapped into $b \times 2^m$-QAM symbol vectors. Note that the code alphabet matches the b-dimensional constellation alphabet (i.e., $q = 2^{mb}$). The precoding matrix $\mathbf{F}_d$ is applied to the transmitted symbol vectors before transmission through the channel $\mathbf{A}_v$ ($\mathbf{A}_v = \mathbf{G}_v\mathbf{A}\mathbf{F}_v$) where the transformed AWGN noise vector is added. The received symbol vector $\mathbf{y}$ is used to compute the log likelihood ratio vector (LLRV) required for log-BP initialization.

The LLRV corresponding to the variable-node v, according to the channel model, is given by

$$\mathbf{L}_{\mathbf{v}} = \left[L_v(v=1) \;\; L_v(v=\alpha) \;\; \cdots \;\; L_v\left(v=\alpha^{q-2}\right)\right], \tag{27}$$

where $\{0, 1, \alpha, \ldots, \alpha^{q-2}\}$ are the elements of GF(q), α represents the primitive element, and

$$L_v\left(v=\alpha^k\right) = \log\left(\frac{P\left(\mathbf{y} \mid v=\alpha^k\right)}{P\left(\mathbf{y} \mid v=0\right)}\right) \quad \text{for } k = 0, \ldots, q-2. \tag{28}$$

The channel LLR value computation is actually done using the following expression:

$$L_v\left(v=\alpha^k\right) = -\frac{1}{N_0}\left(\left\|\mathbf{y}-\mathbf{A}_v\mathbf{F}_d\mathbf{s}^{(k+1)}\right\|^2 - \left\|\mathbf{y}-\mathbf{A}_v\mathbf{F}_d\mathbf{s}^{(0)}\right\|^2\right), \tag{29}$$

where $\mathbf{s}^{(k)}$ represent all possible elements of vectors $\mathbf{s}$ for $k = 0, 1, \ldots, q-2$.

The LLRV values of (28), calculated for all nonbinary GF symbols of a codeword, are the intrinsic messages given as input to the Belief Propagation algorithm. They serve to initialize extrinsic messages, which are then updated through the iterated exchange of messages between variable and check nodes in the Tanner graph representing the code. At the end of every iteration, a posteriori messages are calculated for a decoding attempt. The procedure stops when all the parity check equations are satisfied (null syndrome) or when the maximum number of iterations is reached (decoding failure).

6. EXIT Analysis

EXIT charts predict the behavior of the BP decoder on the basis of only simulated behavior of the individual components decoders (variable-node decoder (VND) and check-node decoder (CND)). Using this approach it is only necessary to simulate the behavior of each component decoder once. Such charts that track the mutual information at each iteration give an excellent visual representation to analyze the decoding convergence.

In [9], Bennatan and Burshtein extend the development of EXIT charts for binary LDPC codes to NB-LDPC codes. In the following, the main results are presented.

The mutual information $I(C;\mathbf{L})$ between the code symbol C and its corresponding LLR vector $\mathbf{L}$ (*a priori* or extrinsic information from VND and CND at each iteration step) can be expressed as

$$I(C;\mathbf{L}) = 1 - E\left[\log_q\left(1 + \sum_{i=1}^{q-1} e^{-\mathbf{L}_i}\right) \mid C = 0\right]. \tag{30}$$

The conditioning on $C = 0$ results in the classical all-zero codeword assumption where the decoder performance is independent of the transmitted codeword.

Using a Gaussian distribution approximation of $\mathbf{L}$ (mean $\mathbf{m}$ and covariance matrix Σ) and symmetry and permutation invariance assumptions as defined in [9], the number of parameters is reduced from $q-1$ to one parameter denoted by σ such that

$$\mathbf{m} = \begin{bmatrix} \frac{\sigma^2}{2} \\ \frac{\sigma^2}{2} \\ \vdots \\ \frac{\sigma^2}{2} \end{bmatrix}; \qquad \Sigma = \begin{bmatrix} \sigma^2 & & & \frac{\sigma^2}{2} \\ & \sigma^2 & & \\ & & \cdots & \\ \frac{\sigma^2}{2} & & & \sigma^2 \end{bmatrix}. \tag{31}$$

That is, $m_i = \sigma^2/2$, $i = 1, \ldots, q-1$, and $\Sigma_{i,j} = \sigma^2$ if $i = j$ and $\sigma^2/2$ otherwise.

The computation of (30) can be numerically evaluated by using the Gaussian approximation (31) and results in a monotonically increasing function $J_q(\sigma) = I(C;\mathbf{L})$ with values from 0 to 1. We denote by $J_q^{-1}(I)$ the corresponding

inverse function. These functions can be obtained by using fitting polynomial approximation [9].

These assumptions result in the expression of the classical mutual information relations for the CND and VND regular LDPC codes, similarly to the binary case:

$$I_{E,\mathrm{VND}}\left(I_A; d_v, I^{(0)}\right) \approx J_q\left(\sqrt{(d_v-1)\left[J_q^{-1}(I_A)\right]^2+\left[J_q^{-1}(I^{(0)})\right]^2}\right), \quad (32)$$

$$I_{E,\mathrm{CND}}\left(I_A; d_c\right) \approx 1 - J_q\left(\sqrt{d_c-1}\,J_q^{-1}(1-I_A)\right), \quad (33)$$

where I_A and $I^{(0)}$ denote the mutual information of the incoming and the initial message, respectively. $I^{(0)}$ equals the capacity of the channel and is given by

$$I^{(0)} = 1 - \frac{1}{q}\sum_{i=1}^{q} E_{\mathbf{n}_v}\left\{\log_q \sum_{j=1}^{q} e^{-d_{i,j}}\right\} \quad (34)$$

with $d_{i,j} = (1/N_0)(\|\mathbf{A}_v\mathbf{F}_d(\mathbf{s}_i-\mathbf{s}_j)+\mathbf{n}_v\|^2-\|\mathbf{n}_v\|^2)$ and $q = 2^{mb}$.

Unlike (33), (32) depends on the channel information (SNR value and MIMO precoding). Based on (32) the computation of $I_{E,\mathrm{VND}}$ highly depends on the mutual information $I^{(0)}$. Higher $I^{(0)}$ implies a higher $I_{E,\mathrm{VND}}$ curve ($J_q(\sigma)$ and $J_q^{-1}(I)$ monotonically increasing functions), which means that the convergence point with the $I_{E,\mathrm{CND}}$ curve will be closer to one. Therefore, by examining the $I^{(0)}$ curves for the different precoders, we should be able to predict the performance of the association with the LDPC code.

In Figure 2, the mutual information $I^{(0)}$ is plotted for every precoder for $b = 2$ data streams in function of γ (cf. (20) and (34)). This plot is shown for a given received normalized SNR equal to 8.0 dB and defined as

$$\mathrm{SNR}_R = \frac{\|\mathbf{A}\|_F^2}{n_R n_T}\frac{E_s}{N_0}. \quad (35)$$

Since the channel energy $\|\mathbf{A}\|_F^2 = \rho^2$ is included in SNR_R, $I^{(0)}$ does not depend on ρ^2. Thus $I^{(0)}$ shows only the influence of the parameter γ for each precoder (cf. (20) and (34)). Note that the values of $I^{(0)}$ are between 0 and 1 since logarithm $\log_q$ uses base $q = 2^{mb}$. In terms of bit per symbol time, the channel capacity is equal to $bmI^{(0)}$, with $b = 2$, and $m = 2$ (4-QAM); values are between 0 and $bm = 4$.

In order to maintain a constant transmission throughput and knowing that some precoders may cancel the weak subchannel and transmit only on the best one, the modulation of the data stream was set to switch to 16-QAM whenever the precoder cancels one subchannel. Therefore the precoders will be denoted in the simulation results as presented in Table 1.

In order to analyze the performance of the precoders in a given Rayleigh MIMO system, it is important to examine the distribution (pdf) of the γ angle. Therefore, Figure 3 plots the probability density function of γ for Rayleigh channel model ($[\mathbf{A}]^{ij} \sim \mathcal{N}_{\mathbb{C}}(0,1)$) for both MIMO (2, 2) and MIMO (2, 4) systems [22].

Table 1: Precoder notations.

Precoder	Notation
Max-SNR (1×16QAM)	MaxSNR
Water-Filling (2×4QAM/1×16QAM)	WF
MMSE (2×4QAM/1×16QAM)	MMSE
Equal Error (2×4QAM)	EE
Quality of Service (2×4QAM-WdB with $W = 10\log_{10}w_2$)	QoS
Max-$d_{\min}$ (2×4QAM)	MaxDmin
Max-$d_{\min}$-DFT-2×4QAM/1×16QAM	MaxdminDFT

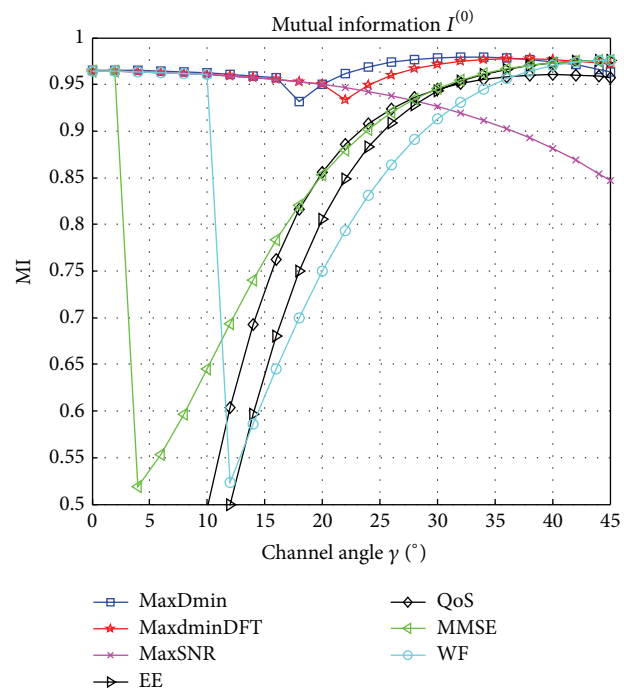

Figure 2: Mutual information $I^{(0)}$ in function of γ for different precoders.

Figure 3 shows that, in the case of MIMO (2, 2) system, the pdf is larger for low γ values than for high γ values, while, in the case of MIMO (2, 4) system, the pdf is considerably larger for high γ values than for low γ values. This will be helpful in order to explain the BER performance with regard to the $I^{(0)}$ values in function of γ. The $I^{(0)}$ values for low γ values will affect the MIMO (2, 2) system and the $I^{(0)}$ values for high γ values will affect the MIMO (2, 4) system performance.

Now that γ distribution is known for both MIMO systems, the impact of γ on $I^{(0)}$ for every precoder can be analyzed, and the performance of each precoder can be predicted for both MIMO systems.

In Figure 2, the curve corresponding to the Equal Error precoder has the lowest values for small γ values and does not increase much for large γ values, compared to other

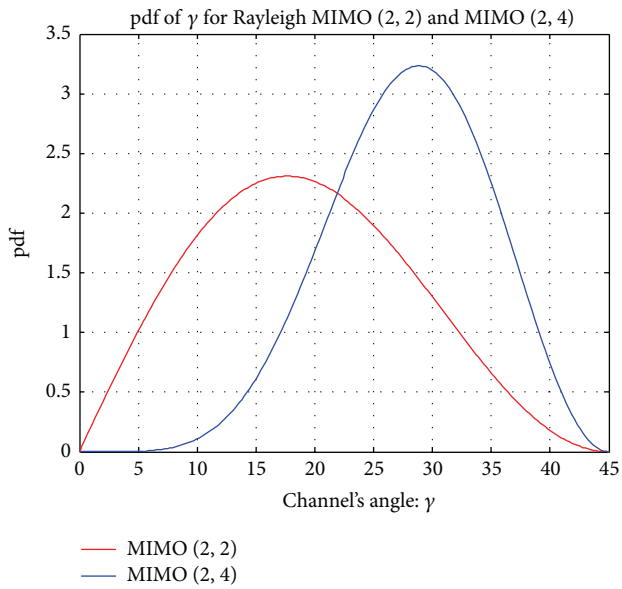

Figure 3: Probability density functions of the γ channel angle for Rayleigh MIMO (2, 2) and MIMO (2, 4) systems.

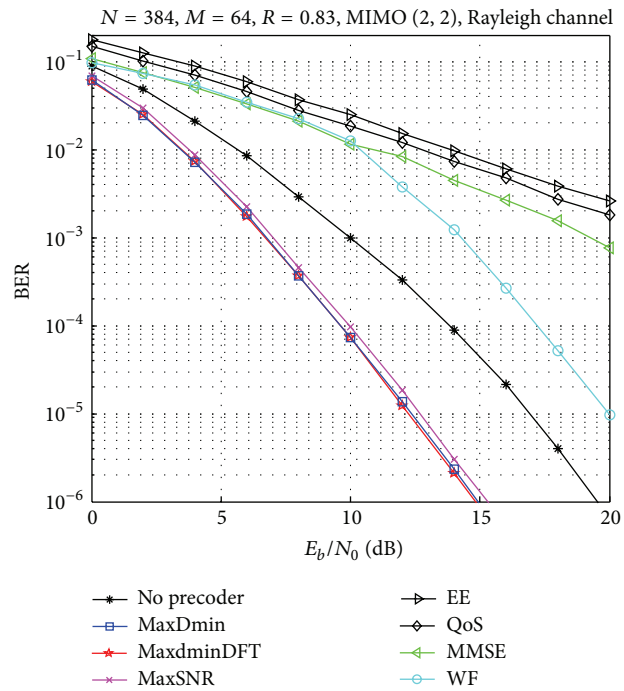

Figure 4: BER performance of the proposed scheme for a (2, 2) MIMO system.

precoders. This will affect the performance of this precoder that should be among the worse compared to other precoders especially in the case of MIMO (2, 2) system.

The curve of the QoS precoder is slightly higher than the EE one, which will result in a slight performance improvement for both MIMO systems.

The WF precoder is a diagonal precoder that is capable of using two subchannels or cancelling the second when the threshold stated in (11) is exceeded. This appears in its curve where high $I^{(0)}$ values are recorded for small γ values, and a switch is clearly seen above a γ limit, where this precoder becomes even worse than the EE. This deterioration will be retrieved in the performance level when γ values increase (MIMO (2, 4)).

The MMSE precoder applies a similar cancellation strategy as the WF with a smaller switch angle. Its curve shows lower $I^{(0)}$ values than the WF for small γ and greater $I^{(0)}$ values for large γ. This will be reflected in better performance of MMSE compared to WF in the case of MIMO (2, 4) system.

These curves show that all diagonal precoders have low $I^{(0)}$ values, which predicts poor performance in terms of BER.

The max-SNR precoder, which can be considered as a special precoder because of its use of one subchannel only, reaches high $I^{(0)}$ values for small γ values. For high γ values, the precoder strategy is to always use one subchannel only, thus wasting the second subchannel that became more advantageous when γ values are high. The max-SNR $I^{(0)}$ curve decreases with increasing γ and becomes low. The max-SNR precoder will have performance as good as nondiagonal precoders for MIMO (2, 2) system and will see its performance deteriorated for MIMO (2, 4) system.

Finally, the nondiagonal precoders based on the minimum Euclidean distance criterion (max-$d_{\min}$ and max-$d_{\min}$-DFT) have both a constant $I^{(0)}$ value larger than all the others, whatever the γ values are. This will result in a better performance of both MIMO systems.

As it is shown in (34), the minimum Euclidean distance appears in the computation of $I^{(0)}$, and the curves of Figure 2 confirm that this criterion is well-suited with the LDPC code association.

In addition, the high values of $I^{(0)}$ for the nondiagonal precoders predict not only better performance in terms of BER, but also a higher convergence rate due to the smaller number of iterations needed in order to reach convergence point on the EXIT charts.

This analysis of the $I^{(0)}$ curves for different precoders will be verified through simulations and the predicted results will be confirmed hereafter (Figures 4 and 5).

7. Simulation Results

The performance of the proposed power allocation scheme has been validated through a series of simulations that assess the achieved improvement in terms of both BER and convergence rate.

The precoders under evaluation are all the above cited diagonal and nondiagonal precoders. LDPC codes are constructed over GF(16) and different parity check matrices are used, having different rates, all derived from matrices designed in the framework of DAVINCI Project [8, 23]. Simulations have been run on two different MIMO configurations: a symmetric (2, 2) system and an asymmetric (2, 4) system. The number of subchannels is set to $b = 2$. The modulation is set to 4-QAM. We consider a flat-fading channel with a Rayleigh distribution model. A new channel realization

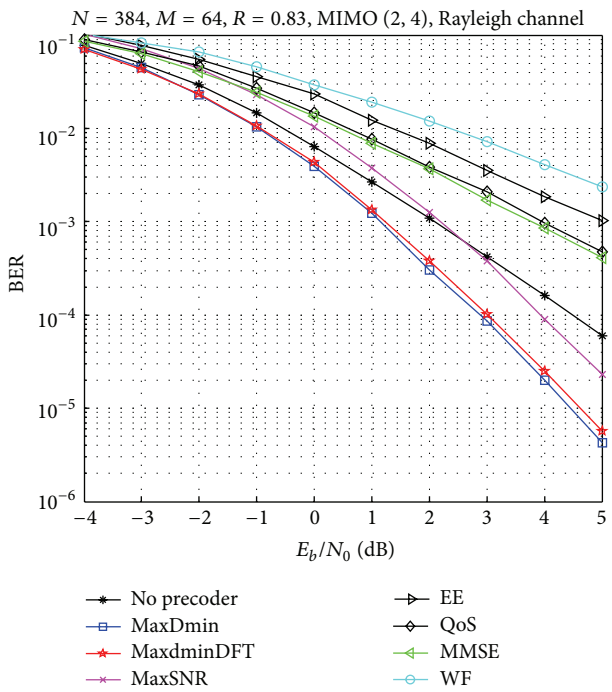

Figure 5: BER performance of the proposed scheme for a (2, 4) MIMO system.

Table 2: SNR per bit definition.

System with precoding	$E_b/N_0 = (E_s/N_0)(1/4R)$
System without precoding (spatial multiplexing)	$E_b/N_0 = (n_T E_s/N_0)(1/4R)$

is considered at each transmitted codeword with $[\mathbf{A}]^{ij} \sim \mathcal{N}_{\mathbb{C}}(0, 1)$. The SNR per bit is defined in Table 2.

Figure 4 illustrates the BER performances versus SNR for a (2, 2) MIMO transmission system with LDPC code designed from the parity check matrix having the following parameters:

(i) matrix size: $N = 384$, $M = 64$, the numbers of nonzero elements in columns and rows being, respectively, $d_v = 2$ and $d_c = 12$,

code rate: $R = 5/6 = 0.83$,

girth: 8.

The curves on this figure assess the performance of the proposed scheme predicted above by EXIT analysis and confirm the results for the MIMO (2, 2) system.

Figure 4 shows that applying diagonal precoders on MIMO systems with LDPC codes deteriorates the performance of the transmission. All diagonal precoders present higher BER than the system with no precoding that was plotted as reference. The only precoders that permit a gain of about 4 dB at high E_b/N_0 are the one based on the minimal Euclidean distance criteria, along with the max-SNR precoder.

Figure 5 illustrates another simulation done with the same configuration over an asymmetric (2, 4) MIMO system. The results show that the diagonal precoders are still damaging the performance and that the max-$d_{\min}$ and the max-$d_{\min}$-DFT still allow a gain of up to 1 dB. The max-SNR precoder shows a weaker performance than that of the symmetric (2, 2) MIMO system.

These simulations confirm the performance predicted from the $I^{(0)}$ values in Figure 2.

These results suggest that the power allocation optimization of LDPC coded MIMO systems should be done using minimal Euclidean distance based precoders.

The use of SVD allows transforming the MIMO channel matrix into b parallel independent eigensubchannels. The diagonal precoder ($\mathbf{F}_d$ is a diagonal matrix) preserves the diagonal structure, which allows transmitting each symbol over each eigensubchannel. The diagonal matrix $\mathbf{F}_d$ allows only obtaining a power allocation strategy among all the subchannels used. In this particular case, the diagonal structure leads to diversity loss. The diversity order of diagonal precoders using b substreams is $(n_T - b + 1)(n_R - b + 1)$. Hence, increasing the throughput by sending multiple symbols at a time loses the full diversity order over flat-fading channel [24, 25]. We obtain performance degradation in terms of BER. Only the special case for max-SNR precoder ($b = 1$) can reach full diversity order. The proposed NB-LDPC codes are not well suited for diagonal closed-loop systems ($b > 1$) due to the bad LLRV initialization of the log-BP algorithm. This bad initialization was clearly examined in the VND curves of the diagonal precoders (Figure 2). The max-$d_{\min}$ precoder that presents full diversity order [22] is well suited with the proposed NB-LDPC. The $I^{(0)}$ values of Figure 2 have already predicted this good match.

Therefore, other simulations have been conducted on the max-$d_{\min}$ precoder (in which performances appear to be equivalent to the max-$d_{\min}$-DFT) in order to validate these results, and four different systems have been compared. The first one is a (2, 2) MIMO transmission without any error correcting coding or precoding. This system is equivalent to "spatial multiplexing (SM)." The second system consists in the same MIMO scheme with the LDPC coding block, which is referred to as "SM-LDPC." The third system consists in a MIMO scheme where the max-$d_{\min}$ precoder is applied and is referred to as "max-$d_{\min}$." The last system is the MIMO scheme with LDPC coding and where the power allocation optimization is done by applying the max-$d_{\min}$ precoder and is referred to as "max-$d_{\min}$-LDPC." Figures 6, 7, and 8 show BER performance of these four systems for LDPC codes rates of 0.5 ($d_c = 4$), 0.75 ($d_c = 8$), and 0.83 ($d_c = 12$), respectively.

In Figure 6 we can see that the SM-LDPC system reaches the BER value of 10^{-5} for E_b/N_0 equal to 12.5 dB while the max-$d_{\min}$-LDPC system reaches the same BER value for only 11 dB. Consequently, the max-$d_{\min}$-LDPC system has a gain of 1.5 dB over the SM-LDPC system for this same BER value.

In Figure 7, it can be noted that, for a higher code rate, the gain of the max-$d_{\min}$-LDPC system over the SM-LDPC is increased and attains 4.2 dB for a BER value of 10^{-5}.

In Figure 8, the increase of the gain between the max-$d_{\min}$-LDPC and the SM-LDPC systems reaches 5 dB for a BER value of 10^{-5} and confirms that the improvement

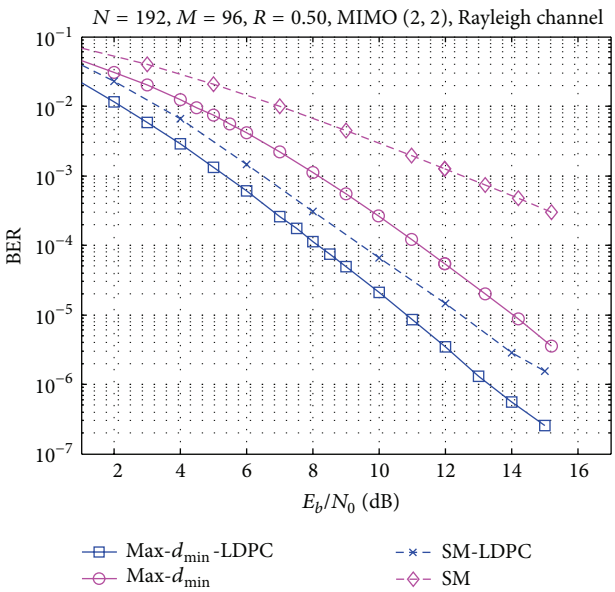

FIGURE 6: BER performance for max-d_{min} with LDPC code rate $R = 0.5$ ($d_c = 4$).

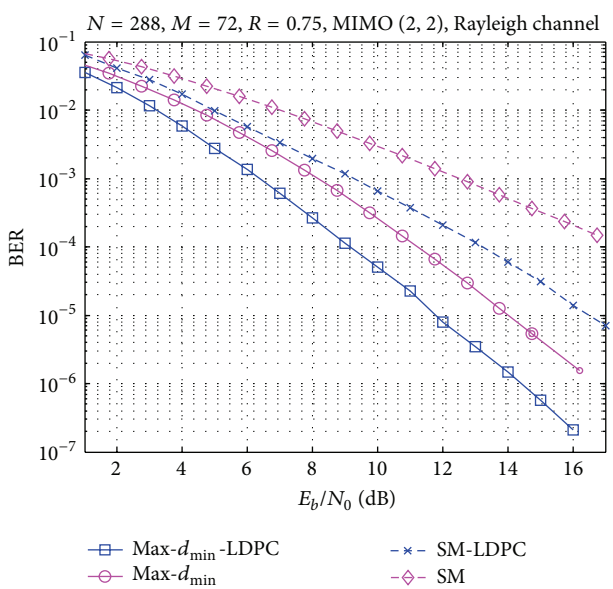

FIGURE 7: BER performance for max-d_{min} with LDPC code rate $R = 0.75$ ($d_c = 8$).

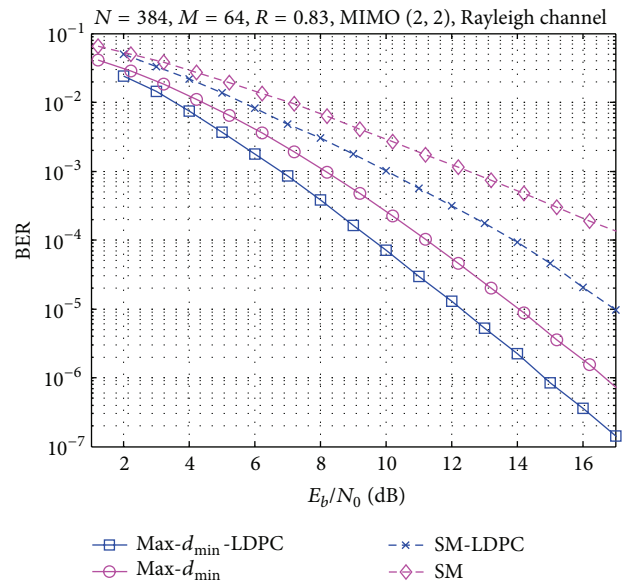

FIGURE 8: BER performance for max-d_{min} with LDPC code rate $R = 0.83$ ($d_c = 12$).

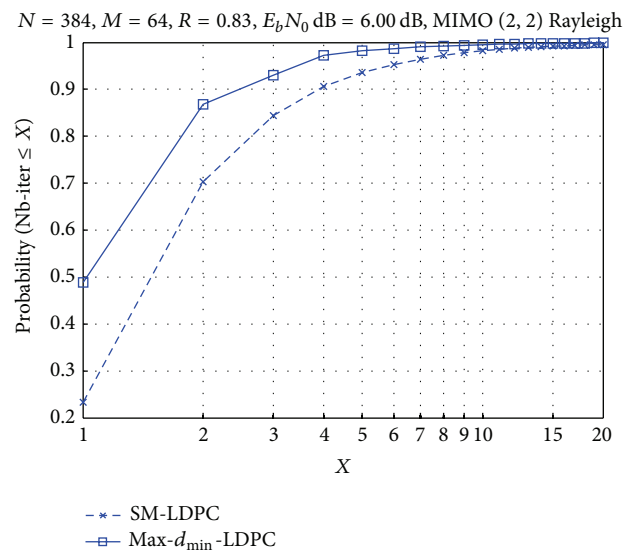

FIGURE 9: Probability of number of iterations till convergence for SM-LDPC and max-d_{min}-LDPC transmissions.

brought by the max-d_{min} precoder to an LDPC coded MIMO system is more significant for LDPC codes with higher rates.

The presence of the max-d_{min} precoder allows an increase of the spectral efficiency compared to the SM-LDPC system. For example, we can see that the BER performance of the SM-LDPC for code rate $R = 0.5$ (Figure 6) and the BER performance of the max-d_{min}-LDPC for code rate $R = 0.83$ (Figure 8) are very similar. The transmission rate is $4 \times 0.5 = 2$ for SM-LDPC and $4 \times 0.83 = 3.33$ for max-d_{min}-LDPC. This is equivalent to a 67% increase in the transmission rate for the same BER performance, due to the use of the max-d_{min} precoder.

The convergence rate of the LDPC decoder, when combined with linear precoding, has been appraised through the simulations and the results point out that a slight improvement is obtained compared to the SM-LDPC transmissions. This result has been already predicted and explained via the EXIT charts analysis above.

We denote by "Nb-iter" the required number of iterations for the BP algorithm to converge (i.e., null syndrome). Figure 9 plots the probability of Nb-iter to be less than or equal to the numbers on the x-axis (abscissa), P (Nb-iter $\leq X$) for $X = 1, 2, \ldots, 20$ and for a fixed SNR per bit at 6 dB. For $X = 1$ the BP algorithm converges at the iteration number 1 in

23% of the cases for the SM-LDPC system, while it converges at the first iteration in 49% of the cases for the max-$d_{\min}$-LDPC. For larger values of X, the gain becomes smaller, but still noticeable.

8. Conclusion

We have presented in this paper a new power allocation optimization scheme that deals with MIMO transmission scheme using ultrasparse NB-LDPC codes adapted for closed-loop MIMO systems and targeted for LTE-A with small to moderate codeword lengths. The proposed scheme makes use of a nondiagonal linear precoder based on the minimal Euclidean distance criteria in order to improve performance in terms of BER. Our study has shown that it is possible to join precoding techniques to such MIMO systems with NB-LDPC codes, but our simulation results also reveal that no improvement is brought by diagonal linear precoders when NB-LDPC codes are used. However, the special case of the max-SNR is competitive for $n_T = n_R = 2$ only. The results of our simulation are predicted and explained by a theoretical EXIT chart analysis that shows the impact of using different precoders on the initial mutual information of the decoder and subsequently its influence on the performance of the proposed association. We have established that using a full diversity order precoder (max-$d_{\min}$ or max-$d_{\min}$-DFT) along with NB-LDPC results in a considerable improvement of the transmission performance and leads to a slight improvement of the convergence rate for the log Belief Propagation algorithm of LDPC decoder. Consequently, thanks to the proposed scheme, a smaller SNR is required to achieve a given BER value. The spectral efficiency is also increased due to the use of LDPC codes of higher rate along with the corresponding precoding. This result implies less energy consumption in the system and promotes green communication applications.

Conflict of Interests

The authors declare that there is no conflict of interests regarding the publication of this paper.

Acknowledgments

This work has been supported by the CORRIDOR (ANR) project and the Images & Réseaux cluster.

References

[1] J. Wang, Z. Lv, and X. Li, "Analysis of MIMO diversity improvement using circular polarized antenna," *International Journal of Antennas and Propagation*, vol. 2014, Article ID 570923, 9 pages, 2014.

[2] R.-H. Peng and R.-R. Chen, "Design of non-binary LDPC codes over GF(q) for multiple-antenna transmission," in *Proceedings of the Military Communications Conference*, pp. 1–7, Washington, DC, USA, October 2006.

[3] L. Collin, O. Berder, P. Rostaing, and G. Burel, "Optimal minimum distance-based precoder for MIMO spatial multiplexing systems," *IEEE Transactions on Signal Processing*, vol. 52, no. 3, pp. 617–627, 2004.

[4] R. G. Gallager, "Low-density parity-check codes," *IRE Transactions on Information Theory*, pp. 21–28, 1962.

[5] T. J. Richardson, M. A. Shokrollahi, and R. L. Urbanke, "Design of capacity-approaching irregular low-density parity-check codes," *IEEE Transactions on Information Theory*, vol. 47, no. 2, pp. 619–637, 2001.

[6] M. G. Luby, M. Mitzenmacher, M. A. Shokrollahi, and D. A. Spielman, "Improved low-density parity-check codes using irregular graphs," *IEEE Transactions on Information Theory*, vol. 47, no. 2, pp. 585–598, 2001.

[7] S.-Y. Chung, G. D. Forney Jr., T. J. Richardson, and R. L. Urbanke, "On the design of low-density parity-check codes within 0.0045 dB of the Shannon limit," *IEEE Communications Letters*, vol. 5, no. 2, pp. 58–60, 2001.

[8] C. Poulliat, M. Fossorier, and D. Declercq, "Design of regular (2, dc)-ldpc codes over gf(q) using their binary images," *IEEE Transactions on Communications*, vol. 56, no. 10, pp. 1626–1635, 2008.

[9] A. Bennatan and D. Burshtein, "Design and analysis of nonbinary LDPC codes for arbitrary discrete-memoryless channels," *IEEE Transactions on Information Theory*, vol. 52, no. 2, pp. 549–583, 2006.

[10] S. Pfletschinger and D. Declercq, "Non-binary coding for vector channels," in *Proceedings of the IEEE 12th International Workshop on Signal Processing Advances in Wireless Communications (SPAWC '11)*, pp. 26–30, June 2011.

[11] A. Voicila, D. Declercq, F. Verdier, M. Fossorier, and P. Urard, "Low-complexity decoding for non-binary LDPC codes in high order fields," *IEEE Transactions on Communications*, vol. 58, no. 5, pp. 1365–1375, 2010.

[12] M. C. Davey and D. MacKay, "Low-density parity check codes over GF(q)," *IEEE Communications Letters*, vol. 2, no. 6, pp. 165–167, 1998.

[13] X.-Y. Hu and E. Eleftheriou, "Binary representation of cycle Tanner-graph GF(2b) codes," in *Proceedings of the IEEE International Conference on Communications*, pp. 528–532, Paris, France, June 2004.

[14] L. Barnault and D. Declercq, "Fast decoding algorithm for LDPC over GF(2^q)," in *Proceedings of the IEEE Information Theory Workshop*, pp. 70–73, Paris, France, March 2003.

[15] S. Pfletschinger, A. Mourad, E. Lopez, D. Declercq, and G. Bacci, "Performance evaluation of non-binary LDPC codes on wireless channels," in *Proceedings of the ICT Mobile Summit Conference*, 2009.

[16] P. Stoica and G. A. Ganesan, "Maximum-SNR spatial-temporal formatting designs for MIMO channels," *IEEE Transactions on Signal Processing*, vol. 50, no. 12, pp. 3036–3042, 2002.

[17] I. E. Telatar, "Capacity of multi-antenna Gaussian channels," *European Transactions on Telecommunications*, vol. 10, no. 6, pp. 585–595, 1999.

[18] P. Rostaing, O. Berder, G. Burel, and L. Collin, "Minimum BER diagonal precoder for MIMO digital transmissions," *Signal Processing*, vol. 82, no. 10, pp. 1477–1480, 2002.

[19] H. Sampath, P. Stoica, and A. J. Paulraj, "Generalized linear precoder and decoder design for MIMO channels using the weighted MMSE criterion," *IEEE Transactions on Communications*, vol. 49, no. 12, pp. 2198–2206, 2001.

[20] Q.-T. Ngo, O. Berder, and P. Scalart, "General minimum Euclidean distance-based precoder for MIMO wireless systems," *EURASIP Journal on Advances in Signal Processing*, vol. 2013, no. 1, article 39, pp. 1–12, 2013.

[21] X. Zhu and R. D. Murch, "Performance analysis of maximum likelihood detection in a MIMO antenna system," *IEEE Transactions on Communications*, vol. 50, no. 2, pp. 187–191, 2002.

[22] B. Vrigneau, J. Letessier, P. Rostaing, L. Collin, and G. Burel, "Theoretical results about MIMO minimal distance precoder and performances comparison," *IEICE Transactions on Communications*, vol. 91, no. 3, pp. 821–828, 2008.

[23] DaVinci project, FP7 INFSO-ICT-216203, http://www.ict-davinci-codes.eu/.

[24] E. Sengul, E. Akay, and E. Ayanoglu, "Diversity analysis of single and multiple beamforming," *IEEE Transactions on Communications*, vol. 54, no. 6, pp. 990–993, 2006.

[25] L. G. Ordoez, D. P. Palomar, A. Pages-Zamora, and J. R. Fonollosa, "High-SNR analytical performance of spatial multiplexing MIMO systems with CSI," *IEEE Transactions on Signal Processing*, vol. 55, no. 11, pp. 5447–5463, 2007.